



# UNIVERSITÀ DEGLI STUDI DI PARMA

FACOLTÀ DI INGEGNERIA  
DIPARTIMENTO DI INGEGNERIA INDUSTRIALE

Dottorato di ricerca in Ingegneria Industriale  
Ciclo XXIX

RICERCA DI DIFETTOLOGIE IN CATENE DI  
RINFORZO MEDIANTE LA MISURA NON  
DISTRUTTIVA DELLA RISPOSTA DINAMICA

NONDESTRUCTIVE TESTING METHOD FOR  
CRACK DETECTION IN TIE-RODS BASED ON  
VIBRATION MEASUREMENT

Tutor:

Chiar.mo Prof. Ing. RINALDO GARZIERA

Chiar.mo Prof. Ing. LUCA COLLINI

Coordinatore del corso di dottorato:

Chiar.mo Prof. Ing. MARCO SPIGA

Dottorando:

Dott.ssa KSENIYA RIABOVA

Anno accademico 2016/2017



---

# Abstract

The present thesis summarizes a research that aims to develop a method for *in situ* health-monitoring of metal tie-rods in historical constructions. Many researchers are working in this highly demanded field especially in Italy considering the numerous heritage buildings and high seismic activity. The novelty of this research is to combine an *in situ* test with quantitative and qualitative analysis of modal parameters and finite element simulations. Along with experiments and numerical solutions, analytical formulations of the problems are outlined as well.

The first chapter of the thesis “Axial load identification in tie-rods” describes a method of the tensile load identification in ancient tie-rods. Solution of the stated problem is delivered by means of vibration measurements combined with parametric finite element modelling and optimization algorithm. The method was approbated on a case study of tie-rods in Casa Romei, Ferrara, Italy, results of which are as well presented in this chapter.

In order to develop a nondestructive technique of damage detection, a special experimental setup was constructed at the laboratory of the Department of Industrial Engineering at the University of Parma. The rig enabled static and dynamic testing of long metal beams with introduced and controlled damage as well as without any defects under adjustable tensile loading, which models the condition of a real operating tie-rod. The second chapter “Damage identification in tie-rods” is hinged on the experimental setup and the method of defect spotting in tie-rods.

The method is based on a nondestructive vibration analysis: a test with an instrumented impact hammer excitation and accelerometric acquisition of the response. These simple tests are very quick and efficient and allow to decrease the time spent on the actual testing on site. Subsequent elaboration of the experimental results in terms of

---

modal analysis provides frequency response functions, coherence functions, eigenfrequencies and modal damping ratios. Further operating these data, we can draw conclusions about the stress state condition and structural integrity of the tested tie-rods.

The results of static compliance tests are correlated with the calculations based on the linear elastic fracture mechanics methods that are addressed in the third chapter “Fracture mechanics approach”. It also focuses on the classification of cracks in round bars and points out the grounds of damage representation adopted in the previous chapter.

In contemporary mechanical studies numerical simulations are an important tool for sensitivity analysis and validation of experimental results. Experiments help improve the modelling and numerical analysis, in its turn, assists to facilitate and improve the efficiency of experiments. In the fourth chapter of the thesis “FEM simulations” we clarify the numerical modelling used to confront the experimental approach reported in previous chapters.

Finally, the chapter “Conclusion” bottom-lines the results of the research and looks out on further perspectives of its development.

---

# Abstract

La presente tesi riassume una ricerca con lo scopo di sviluppare un metodo per il monitoraggio in situ delle catene di rinforzo nelle costruzioni storiche. Tanti ricercatori stanno lavorando su questo campo, soprattutto in Italia considerando i numerosi edifici storici e l'elevata attività sismica. La novità di questa ricerca consiste nella combinazione dei test in situ con le analisi quantitative e qualitative dei parametri modali e, inoltre, con le simulazioni agli elementi finiti. Oltre alla soluzione numerica anche le formulazioni analitiche dei problemi sono state definite.

Il primo capitolo della tesi "Identificazione del carico assiale nelle catene di rinforzo" descrive un metodo per determinare il carico assiale di trazione nelle catene di rinforzo antiche. La soluzione del problema è conseguita tramite le misure vibrometriche, la modellazione parametrica agli elementi finiti e l'algoritmo di ottimizzazione. Il metodo è stato applicato ad un caso di studio, sulle catene di Casa Romei a Ferrara, i cui risultati sono riportati nel primo capitolo.

Al fine di sviluppare una tecnica non distruttiva di rilevamento dei danni, un impianto sperimentale è stato costruito presso il laboratorio del Dipartimento di Ingegneria Industriale dell'Università di Parma. L'impianto è abilitato a prove sia statiche sia dinamiche su travi metalliche con danni introdotti e controllati oppure senza difetti. Le travi, sottoposte al carico di trazione regolabile, riproducono le condizioni operative di un tirante vero. Nel secondo capitolo "Identificazione dei danneggiamenti nelle catene di rinforzo" è trattato l'impianto sperimentale e la tecnica non distruttiva per la difettologia delle travi.

Il metodo si basa sull'analisi delle vibrazioni: la catena viene eccitata con un martello strumentale e la risposta dinamica è registrata tramite accelerometri. Questi semplici test sono veloci ed efficienti e permettono di diminuire il tempo speso per la

---

prova vera in situ. L'elaborazione successiva dei risultati sperimentali in termini dell'analisi modale fornisce le funzioni di risposta in frequenza, le funzioni di coerenza, le frequenze modali e i rapporti di smorzamento modali. Analizzando ulteriormente questi dati è possibile trarre delle conclusioni sullo stato di sollecitazione e sull'integrità strutturale delle catene monitorate.

I risultati delle prove statiche di cedevolezza sono correlati con i calcoli basati sui metodi della meccanica della frattura lineare elastica che vengono affrontati nel terzo capitolo "Approccio della meccanica della frattura". Esso si concentra inoltre sulla classificazione delle cricche nelle travi tonde, giustificando la rappresentazione del difetto adottata nel capitolo precedente.

Negli studi meccanici contemporanei le simulazioni numeriche sono diventate uno strumento importante per l'analisi di sensibilità e per la validazione dei risultati sperimentali. Le prove sperimentali contribuiscono al miglioramento della modellazione e le simulazioni numeriche, a loro volta, consentono di aumentare l'efficienza degli esperimenti. Il quarto capitolo "Simulazioni FEM" chiarifica la modellazione numerica utilizzata per affrontare l'approccio sperimentale riportato nei capitoli precedenti.

Infine, il capitolo "Conclusione" evidenzia i risultati principali di questa ricerca e sottolinea le prospettive dei suoi sviluppi futuri.

---

# Acknowledgements

This dissertation is a milestone at the end of my three-year journey through the PhD course. I am thankful to the Ministry of Education, University and Research (MIUR) of the Italian Government that granted my studies and to the University of Parma for accepting me to the postgraduate program and opening the doors of the academia.

I also would like to express my deepest gratitude and appreciation

To my advisors and mentors, professors Rinaldo Garziera and Luca Collini, for all the wisdom, knowledge, ideas and experience you transmitted to me during these past three years. For teaching me “calma, dignità e classe”. For opportunities and kicks, responsibilities I was entitled to and your faith in me. I feel honoured to have worked in your research group.

To professor Marco Amabili, for the honour of doing an internship under your guidance at the McGill University in Montreal, and for the productive cooperation.

To professor Angelo Farina, for involving me in a challenging and prospective research project.

To professors of the Department of Industrial Engineering for the stimulating courses, and to the staff and fellow PhD students, for the pleasure of working together.

To the most important people in my life, to whom I owe my education and accomplishments, my beloved family of engineers: my parents Irina and Sergey, my grandparents Boris and Irina, and my brother Vladimir. I am blessed to have you.

To Monica, Giovanni and Luca for making an invaluable impact on my life in Italy.

And, above all, to Daniele, an admirable engineer and an honourable man, who grants me happiness every single day, through thick and thin.

---

# Table of Contents

<b>Introduction</b> .....	1
<b>Chapter 1 Axial load identification in tie-rods</b> .....	4
1.1 Introduction .....	4
1.2 State of the art in axial load identification in beams .....	5
1.3 Dynamic method for load identification .....	8
1.3.1 Analytical formulation of the problem .....	9
1.3.2 Numerical model and optimization procedure .....	14
1.4 Application to a case study.....	15
1.4.1 Load identification results .....	17
1.4.2 Analysis of the results.....	20
1.5 Conclusions .....	22
<b>Chapter 2 Damage identification in tie-rods</b> .....	24
2.1 Introduction.....	24
2.1 State of the art in damage identification of beams .....	26
2.2 The experiment: general concept and execution .....	33
2.2.1 Damage representation .....	33
2.2.2 Experimental set-up.....	36
2.3 Experimental modal analysis .....	52
2.3.1 Data acquisition .....	52
2.3.2 Data elaboration: FRF and coherence .....	54
2.3.3 Experimental results .....	56
2.3.4 Influence of the axial load on beam vibrations.....	62
2.3.5 Influence of the damage on beam vibrations.....	65
2.4 Static tests.....	74



---

2.4.1 Flexural test .....	74
2.4.2 Tensile test.....	81
2.5 Conclusions .....	84
<b>Chapter 3 Fracture mechanics approach .....</b>	<b>86</b>
3.1 Introduction .....	86
3.2 Stress concentrations .....	87
3.3 Cracks in round beams .....	90
3.4 Compliance.....	96
3.5 Conclusions .....	99
<b>Chapter 4 FEM simulations .....</b>	<b>100</b>
4.1 Introduction .....	100
4.2 Beam and crack modelling.....	101
4.3 Modal Analysis .....	106
4.4 Conclusions .....	110
<b>Conclusion .....</b>	<b>111</b>
<b>Bibliography .....</b>	<b>114</b>

---

# List of Figures

Figure I.1. Tie-rods in the Castle of Torrechiara in Langhirano, Parma, Italy.....	2
Figure 1.1. Tie-rod with elastic bed-type boundaries.....	8
Figure 1.2. Inner yard of Casa Romei and zoom of the ground floor tie-rods. ....	15
Figure 1.3. Our team during hammer excitation of a tie-rod; map of ground floor. ....	16
Figure 1.4. FRF plot (acceleration amplitude vs. frequency).....	16
Figure 1.5. Residual error function as function of elastic bed stiffness and axial load..	18
Figure 1.6. Influence of the elastic bed on the axial load determination.....	19
Figure 1.7. Average stress state in tie-rods: comparison between encastré and elastic foundation boundaries. ....	20
Figure 1.8. Residual error functions for sets of weight coefficients $W_1, W_2, W_3$ .....	21
Figure 2.1. FRF of a tie-rod with a "broken peak".....	25
Figure 2.2. Two parts of the beam with a bolt connection. ....	35
Figure 2.3. Beam installed in the supporting and tensioning system. ....	37
Figure 2.4. Manual hydraulic lift.....	38
Figure 2.5. NI cDAQ-9174 system with NI 9219 and NI 9234 during the tests. ....	39
Figure 2.6. Schematic of a metallic strain gauge.....	40
Figure 2.7. Strain gauges configured in Wheatstone bridge circuits to detect small changes in resistance. ....	41
Figure 2.8. Half-bridge strain gauges. ....	41
Figure 2.9. Strain gauges glued to the beam and their datasheet.....	42
Figure 2.10. Layout of the electrical connection for a strain gauge in a half-bridge configuration.....	42
Figure 2.11. Calibration line for the strain gauge in the half-bridge configuration. ....	44

---

Figure 2.12. Dependence between reading of the strain gauge and the actual tensile strain. ....	45
Figure 2.13. KMR Force washer 200 kN by HBM. ....	46
Figure 2.14. Load cell mounted on the beam. ....	46
Figure 2.15. Layout of the electrical connection for a load-cell in a full-bridge configuration.....	47
Figure 2.16. Dependence between load cell sensibility and applied load. ....	48
Figure 2.17. Dependence between load cell reading and actual tensile strain. ....	49
Figure 2.18. Instrumented impact hammer.....	50
Figure 2.19. Accelerometer used for dynamic response acquisition. ....	51
Figure 2.20. Experimental setup and the laboratory workspace.....	52
Figure 2.21. Screenshot of the program for data acquisition developed in LabView. ....	53
Figure 2.22. Example of a signal recorded from the strain gauge.....	57
Figure 2.23. Example of a signal recorded from the load cell.....	57
Figure 2.24. Example of input and output signals: impulse excitation and response.....	58
Figure 2.25. Windowing of input and output signals. ....	59
Figure 2.26. FRF, coherence and input/output power spectra. ....	60
Figure 2.27. FRF and coherence function with picked peak frequencies.....	61
Figure 2.28. Scheme of a beam in the experimental setup. ....	62
Figure 2.29. Fundamental frequency of a beam in tension. ....	65
Figure 2.30. First and second natural frequencies of the healthy and damaged beams with respect to axial load. ....	66
Figure 2.31. FRFs of healthy and damaged beams under tensile load of 6.03 kN and 5.99 kN. ....	68
Figure 2.32. FRFs of healthy and damaged beams under tensile load of 11.70 kN and 11.91 kN. ....	70
Figure 2.33. FRF of damaged beam under tensile load of 11.91 kN with a low-amplitude second peak.....	71
Figure 2.34. FRFs of damaged beam under tensile load of 5.99 kN. ....	72
Figure 2.35. First natural frequency of damaged beam with respect to axial load and different torques at the joint.....	73

---

Figure 2.36. Second natural frequency of damaged beam with respect to axial load and different torques at the joint.....	73
Figure 2.37. Scheme of a beam under flexural compliance testing.....	74
Figure 2.38. Flexural test setup. ....	77
Figure 2.39. Results of flexural compliance test with five different weights for damaged beam torqued with 25 Nm. ....	78
Figure 2.40. Flexural compliance test of the damaged beam. ....	79
Figure 2.41. Flexural compliance of healthy and damaged beams: test vs. FEM simulation. ....	80
Figure 2.42. Axial stiffness test setup.....	81
Figure 2.43. Scheme of a beam under axial compliance testing. ....	81
Figure 2.44. Axial displacement vs. tensile load for healthy and damaged beams. ....	83
Figure 2.45. Axial compliance of healthy and damaged beams.....	83
Figure 3.1. Crack in an ancient iron tie-rod.....	87
Figure 3.2. Stress concentration factor $K_t$ for a grooved round bar in tension.....	88
Figure 3.3. Beam with a circular defect loaded in tension. ....	90
Figure 3.4. Dimensionless stress intensity factor $\beta_I$ for a ring-shaped crack in a round beam.....	91
Figure 3.5. Beam with a disk-shaped defect loaded in tension. ....	92
Figure 3.6. Dimensionless stress intensity factor $\beta_F$ for a disk-shaped crack in a round beam.....	93
Figure 3.7. Beam with a semi-elliptical defect loaded in tension.....	94
Figure 3.8. Dimensionless stress intensity factor $\beta_I$ for a semi-elliptical crack in a round beam.....	94
Figure 3.9. Stress intensity factors $K_I$ vs. axial load for three equivalent cracks: ring-shaped, disk-shaped and semi-elliptical. ....	95
Figure 3.10. Dimensionless compliance of a beam with a circular defect loaded in tension.....	98
Figure 4.1. Tie-rod represented with Beam elements in Abaqus CAE. ....	103
Figure 4.2. Tie-rod represented with Solid elements in Abaqus CAE. ....	104
Figure 4.3. Damaged tie-rod in Abaqus CAE. ....	106
Figure 4.4. Model validation: natural frequencies of an unloaded beam. ....	106

---

Figure 4.5. Natural frequencies of the healthy beam: experiment vs. FEM.....	108
Figure 4.6. Natural frequencies of the damaged beam: experiment vs. FEM. ....	109
Figure 4.7. Fundamental frequency of the healthy and damaged beams in FEM. ....	109

---

# List of Tables

Table 1-1. Experimental acquisitions. ....	17
Table 1-2. Summary of results. ....	19
Table 1-3. Results of computation with three sets of weights for the tie-rod PT4. ....	22
Table 2-1. Beam properties. ....	36
Table 2-2. Natural frequencies and damping ratios of the first three modes of the healthy beam under axial load of 13.49 kN. ....	62
Table 2-3. Natural frequencies of the tested beams under tensile loading. ....	67
Table 4-1. Modal shapes of the healthy beam under tensile load of 11.7 kN. ....	107

---

# Introduction

The term “beam” refers generally to any construction element, which has one linear dimension much larger than other two (cross-section). The present thesis specifically investigates so-called “*tie-rods*” – metal beams used in a wide range of civil constructions. The main purpose of these structural elements is to provide support for masonry arches and vaults in ancient buildings, like churches, cathedrals and castles, which are known to lurch and founder in course of time. Tie-rods are subjected to axial tension and, thus, help the building resist lateral loads exerted by walls and facades. Figure I.1 pictures a typical layout of tie-rods supporting arches of the first floor terrace in a medieval *Castello di Torrechiara* (Castle of Torrechiara) in a town of Langhirano, province of Parma, Italy.

Indeed, over the years, deformations of masonry walls and eventual displacements in the building may cause significant changes in the axial loads of tie-rods. In the extremes, this can lead to either of two scenarios: failure in structural integrity of tie-rods (damages and cracks), or loss of loads and subsequent performance decline – a phenomenon referred to as the “laziness” of tie-rods. Both of the scenarios are dangerous for the safety and integrity of buildings and can lead to irretrievable harm to the precious historical heritage of the human race. For this reason regular monitoring of tie-rods’ condition is of a great importance.

Health monitoring of tie-rods includes two major steps. The first one is identification of axial load and the second one is damage identification. As for the first one, multiple methods have been developed to accomplish this task; some details on the state of art are provided in Chapter 1 “Axial load identification in tie-rods”. However, the knowledge of axial load is not enough to assess the condition of structural tie-rods, because it does not contain any information on possible small damages inside them. As

for the damage identification, it definitely requires a more profound inspection of beams and a more careful analysis of experimental data. Such experimental techniques should be as less invasive as possible and at the same time provide sufficient data on the beam condition. Generally this type of testing is referred to as “nondestructive”.



**Figure I.1. Tie-rods in the Castle of Torrechiara in Langhirano, Parma, Italy.**

In particular, non-destructive testing (NDT) is the process of investigating structures and elements for characteristics, discontinuities, changes in properties, etc. without harming the continuity and usability of the part under testing. The tests that are destructive in nature are done on a limited number of samples and cannot be performed on real parts that are further put in service. These tests are used to determine the physical properties of materials such as impact resistance, ductility, yield and ultimate



---

tensile strength, fracture toughness and fatigue strength, but discontinuities and differences in material characteristics are more effectively found by the NDT. Today modern non-destructive tests are used in manufacturing, fabrication and in-service inspections to ensure product integrity and reliability, to control manufacturing processes, lower production costs and to maintain a uniform quality level. During construction, NDT is used to ensure the quality of materials and joining processes during the fabrication and erection phases, and in-service NDT inspections are used to ensure that the products and construction elements in use continue to have the integrity necessary to ensure their usefulness and safety.

NDT methods include: vibration analysis, acoustic emission testing, electromagnetic testing, guided wave testing, ground penetrating radar, laser testing methods, leak testing, magnetic flux leakage, microwave testing, liquid penetrant testing, magnetic particle testing, neutron radiographic testing, radiographic testing, thermal/infrared testing, ultrasonic testing and visual testing.

Vibration Analysis (VA) is a relatively cheap, easily executable and reliable way of health-monitoring of the structures. VA can be applied to testing whole buildings as well as its smallest parts depending on the scope and approach used. The present research focuses on VA application for *in situ* crack damage identification in metal beams (tie-rods).

VA is based on investigation of dynamics of a structure under a certain excitation: it can be an impact hammer or a shaker. The response to the excitation is registered via sensors: accelerometers, optic sensors, laser, etc. Vibrational response contains information about the main structural characteristics: mass and stiffness. A crack does not influence the mass property of a beam, but it does change the local stiffness. A possibility to detect these changes throughout an *in situ* test of a simple execution would facilitate the regular monitoring of tie-rods or other metal beams and make them more efficient.

At the same time a reliable experimental technique will help to validate analytical and numerical models used for prediction of cracked beam dynamics.

The purpose of this research is to develop a VA procedure based on quantitative and qualitative analysis of frequency response functions.

---

# Chapter 1

## Axial load identification in tie-rods

*This Chapter describes a method of tensile load identification in tie-rods. Solution of the stated problem is delivered by means of vibration measurements combined with parametric finite element modelling and optimization algorithm. The method was approbated on a case study of tie-rods in Casa Romei, Ferrara, Italy, results of which are presented herein.*

### 1.1 Introduction

Tie-rods are mostly inserted in old historical constructions, so there is no possibility for a direct *in situ* measurement of the force acting on the tie-rod. In addition, one has to accept the absence of information on: technical drawings, material specifications, construction phases, periods of tie-rods implementation, fixing and anchoring of tie-rods, etc. Basically, we can only operate the data collected from *in situ* measurements nowadays.

This section describes a method for axial load identification in tie-rods developed by the Department of Industrial Engineering of the University of Parma. This approach

combines *in situ* dynamic tests and computations that make use of a beam model with complex boundary conditions. The method was tested and improved throughout some years since it was applied for multiple case studies of monitoring such famous Italian historic buildings as *Duomo di Parma* (Cathedral of Parma), *Basilica della Madonna dell'Umiltà* in Pistoia (Church of Our Lady of Humility), *Rocca Sanvitale di Fontanellato* (Sanvitale Fortress of Fontanellato), *Casa Romei* (Romeis House) in Ferrara, as reported by supervisors of this thesis professors *L. Collini and R. Garziera*, our colleagues professors *M. Amabili, M. Vanali et al.* and the author *K. Riabova* herself in [1-7].

## **1.2 State of the art in axial load identification in beams**

The structural characterization of tie-rods is crucial for the safety assessments of historical buildings. The main parameters that characterize the behaviour of tie-rods are the tensile force, the modulus of elasticity of the material and the rotational stiffness at both restraints. In the last decades several techniques for an indirect non-destructive evaluation of such parameters have been proposed. The non-destructive procedures currently available for the structural characterization of tie-rods can be grouped in static, static–dynamic and pure dynamic approaches. Pioneering static methods presented, for instance, in works of *P. Pozzati, M. Beconcini, S. Briccoli Bati and U. Tonietti* [8-10], in spite of minor differences, are based on measures of displacement and/or strain at few cross-sections of the tie-rod due to applied static loads. *S. Briccoli Bati and U. Tonietti* introduced a static approach for force identification that consisted of measuring three vertical displacements and strains variations at three sections of the tie-rod under a concentrated load [10]. Even if the data post-processing is quite straightforward, these methods are extremely sensitive to the experimental error in the measures of displacement. In addition, since tie-rods are usually positioned at considerable heights, the need of measuring vertical deflections with respect to a reference fixed base makes static methods difficult in practice.

Mixed approaches try to identify the unknown parameters by combining static and dynamic measures. *C. Blasi and S. Sorace* [11-13] modelled tie-rods as simply supported Euler beams with rotational springs of similar stiffness added on each edge. The stiffness of the spring and the force were the two unknowns obtained from the system of equations, built with a static equation for deflection and a dynamic equation for natural frequencies. Thus, this method required data from two separate experiments, i.e. *in situ* measurements of the central deflection under static load and of the fundamental natural frequency, which can be obtained by hammer impact testing and Fourier transforming the recorded accelerations. Testing of this method in laboratory conditions showed good results, however, measurement errors can cause significant deviation in results for the two unknowns. Even though static-dynamic methods can exploit additional dynamic information for the characterization, they are still affected by the shortcomings related to deflection measurements.

Such drawbacks are avoided in pure dynamic procedures [14-28], where, in general, the difference between the experimental and the calculated natural frequencies of vibration is minimized in order to identify the unknown parameters.

*S. Lagomarsino and C. Calderini* [14] developed an algorithm to identify the axial tensile force in ancient tie-rods by using the first three natural frequencies. The tie-rod was modelled as an Euler beam of uniform cross-section, neglecting the shear deformation and rotary inertia, and was assumed to be simply supported at the ends with additional rotational springs.

Recently *K. Maes et al.* introduced a method that enables definition of axial loads in slender beams with unknown boundary conditions, taking into account effects of rotational inertia of the beam and masses of sensors [15]. However, it requires data from five or more sensors along the length of the beam to determine all the introduced unknowns of the inverted problem. A similar technique of the axial force identification was developed by *S. Li et al.* [16], focusing on studies of Euler–Bernoulli beams and takes into account bending stiffness effects.

*G. Rebecchi et al.* established an analytical method of processing experimental data from five instrumented sections of a prismatic slender beam, which showed excellent results in estimation of the axial load in tie-rods [17]. The method does not require any exact value of effective length of the beam, but neglects both rotary inertia and shear

deformations effects in the solution for beam vibrations. For cases of similar beams their colleagues *N. Tullini et al.* proposed a static method of axial force identification [18-20]. The analytical algorithm makes use of any set of experimental data represented by flexural displacements or curvatures measured at five cross-sections of the beam subjected to an additional concentrated lateral load. *C. Gentilini et al.* developed in [21] a procedure that combines dynamical testing with FEM simulations using added masses. The method was tested out for tie-rods of various length and load intensity, showing reliable results.

*T. Livingston et al.* identified the tensile force in prismatic beams of uniform section by using modal data and assuming rotational and vertical springs at each end of the beam [22]. Shear deformation and rotary inertia were neglected (according to the Euler beam model).

Another fully dynamic procedure has been proposed by *B. Kim and T. Park* [23]. It allows to identify the tension force, flexural and axial stiffness of the cable from measured natural frequencies. Anyway this technique is not immediately applicable to tie-rods since they cannot be modelled as cables and present uncertain constraints due to the portion of the rod inserted into the masonry wall or column.

*M. Amabili, L. Collini, R. Garziera, M. Vanali et al.* [1-6] developed a two-step method consisting of in situ measurements of tie-rods' natural frequencies and further elaboration of the data via an optimization algorithm based on the Rayleigh – Ritz method [7]. Varying certain parameters, the main of which was the sought axial load, this algorithm matched estimated sets of frequencies with those determined from experiments. The considered numerical models allowed analysis of ancient tie-rods affected by non-perfect constraints, added masses, discontinuities, irregular cross-sections and complex boundary conditions. Different importance of the natural frequencies can be as well taken into account. The technique is of simple execution and allows to minimize the measurement error. Its functionality and reliability have been proved as it has been applied with success to many case studies.

## 1.3 Dynamic method for load identification

The first step of the method is in situ experimental identification of natural frequencies of the tie-rods by measuring the frequency response functions (FRFs) via instrumented hammer excitation. Precisely the testing technique used for the investigation of tie-rods in Casa Romei located in the city of Ferrara, Emilia-Romagna, Italy [5-6] is described in the next Chapter 2. The first four to six natural frequencies, which can be extracted with high precision, were in the focus. Subsequently, an axially loaded tie-rod was modelled in finite element method (FEM) software Abaqus 6.13 as a general case of a Timoshenko beam, using three-dimensional beam elements retaining shear deformation and rotational inertia. The parametric model enabled considering non-uniform cross-sections of rods, since this is often the case for hand-made tie-rods in old buildings.

The interface tie-rod/wall was assumed to be a continuous elastic bed, i.e. extremities of tie-rods inserted inside masonry walls were modelled as resting on Winkler-type foundation. This type of boundary has been used in dynamics of particular cases, for example, for beams or rails subjected to travelling loads, as reported by *S. Farghaly et al.* [29], *P. Ruge et al.* [30] and *S. Koroma et al.* [31]. In our case we discretized the elastic bed into separate springs equispaced along the length of the bed  $l_f$ , each of a stiffness  $k_f$  (see Figure 1.1).

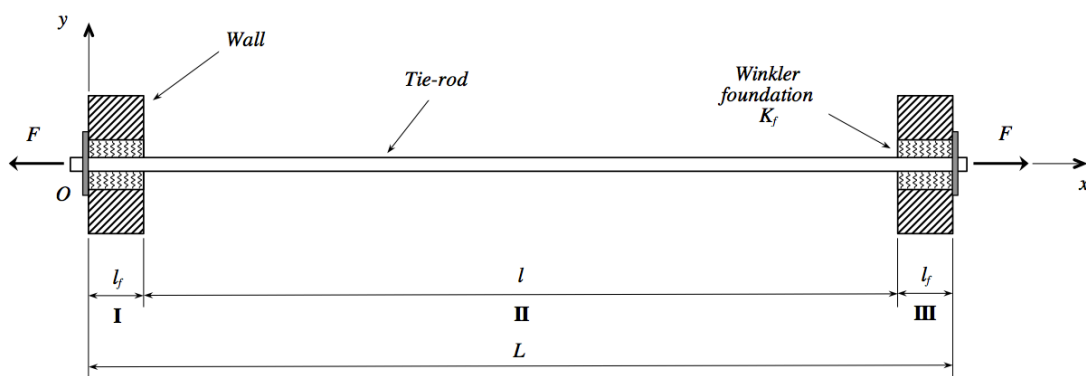


Figure 1.1. Tie-rod with elastic bed-type boundaries.

Clearly, the foundation may have a non-uniformly distributed stiffness, which would result in different  $k_f$  assigned to each spring. The advantage of the Winkler bed

compared to other types of boundaries generally used for tie-rods is that a number of springs placed closely exhibit more complex behaviour than linear and/or rotational springs attached to a single node. Hence, it is a reliable way of modelling a real wall-rod contact condition. The optimization parameters in this case were the unknown axial load, the stiffness of the foundation and the length of the rod inside the wall.

### 1.3.1 Analytical formulation of the problem

As shown in Figure 1.1, tie-rod was divided in three sections of length  $l_f$  – section I,  $l$  – section II and again  $l_f$  – section III, where  $l_f$  identifies the portion inserted into the wall and  $l$  is the measured “free” length. At the tips of the rod free-end boundary conditions were applied and between the sections, correspondingly, the conditions of congruence.

Assuming the hypotheses of Bernoulli-Euler beam theory for the analytical formulation, we chose to neglect the shear deformation and rotational inertia, because the subject of this study was a slender rod, for which the ratio of linear dimensions of cross-sections to length is a very small number.

The energy approach was used to obtain the equations of motion via Lagrangian of the system [1]. Thus, the energy functionals were represented by Equations (1-4).

- Kinetic energy

$$T = \frac{1}{2} \int_0^L \left[ \rho A \left( \frac{\partial w}{\partial t} \right)^2 + \rho I \left( \frac{\partial^2 w}{\partial x \partial t} \right)^2 \right] dx \quad (1)$$

- Potential energy of elastic strain

$$U = \frac{1}{2} \int_0^L \left[ EI \left( \frac{\partial^2 w}{\partial x^2} \right)^2 \right] dx \quad (2)$$

- Potential energy associated with the axial load

$$V_F = \frac{1}{2} \int_0^L \left[ F \left( \frac{\partial w}{\partial x} \right)^2 \right] dx \quad (3)$$

- Potential energy associated by the elastic foundation

$$V_w = \frac{1}{2} \int_0^L K_f w^2 \left[ H(l_f - x) + H(x - L + l_f) \right] dx \quad (4)$$

Where the following symbols were adopted:

$w(x,t)$  is the function of beam deflection in  $xOy$  plane;

$L$  is the total length of a tie-rod;

$\rho$  is the material density;

$E$  is the material elastic modulus;

$A$  is the cross-section area;

$I$  is the moment of inertia of the cross-section about  $z$  axis;

$F$  is the axial load;

$K_f$  is the distributed stiffness of elastic bed;

$H(x)$  is the Heaviside function, which allows us to write down a single expression for the whole tie-rod, taking into account different conditions for its parts.

We proceeded defining the Lagrangian of the system, which is equal to the difference between the overall kinetic and potential energy, Equation (5).

$$L \left( w, \frac{\partial w}{\partial x}, \frac{\partial w}{\partial t}, \frac{\partial^2 w}{\partial x^2}, \frac{\partial^2 w}{\partial x \partial t} \right) = T - \Pi \quad (5)$$

Applying the Hamilton's principle, we obtained the system of Lagrange equations of motion (6), where  $q_k$  indicated every generalized coordinate (degree of freedom) and the number of differential equations was equal to the number of *dofs*. In our case the degree of freedom was represented by the function  $w(x,t)$ .



$$\frac{\partial}{\partial t} \left( \frac{\partial L}{\partial \dot{q}_k} \right) - \frac{\partial L}{\partial q_k} = 0 \quad (6)$$

Sequentially substituting Equations (1-4) into Equation (5) and then differentiating the Lagrangian as shown in Equation (6), we obtained the equation of natural vibrations of the rod (7).

$$EI \frac{\partial^4 w}{\partial x^4} + \rho A \frac{\partial^2 w}{\partial t^2} - F \frac{\partial^2 w}{\partial x^2} + K_f w \left[ H(l_f - x) + H(x - L + l_f) \right] = 0 \quad (7)$$

As stated above, the ends of tie-rods (where  $x = 0$  and  $x = L$ ) were considered free and between the parts I – II and II – III eight conditions of continuity emerged, this provides twelve conditions that were expressed in form of Equation (8).

$$\begin{aligned} x = 0 : & \begin{cases} Q_I = 0 \\ M_I = 0 \end{cases} & x = L : & \begin{cases} Q_{III} = 0 \\ M_{III} = 0 \end{cases} \\ x = l_f : & \begin{cases} w_I = w_{II} \\ \frac{\partial w_I}{\partial x} = -\frac{\partial w_{II}}{\partial x} \\ Q_I = Q_{II} \\ M_I = M_{II} \end{cases} & x = L - l_f : & \begin{cases} w_{II} = w_{III} \\ \frac{\partial w_{II}}{\partial x} = -\frac{\partial w_{III}}{\partial x} \\ Q_{II} = Q_{III} \\ M_{II} = M_{III} \end{cases} \end{aligned} \quad (8)$$

The shearing force  $Q$  and the bending moment  $M$  were defined by Equations (9).

$$\begin{aligned} Q &= EI \frac{\partial^3 w}{\partial x^3} - F \frac{\partial w}{\partial x} \\ M &= EI \frac{\partial^2 w}{\partial x^2} \end{aligned} \quad (9)$$

For each section of the tie-rod (see Figure 1.1 for the reference system), a separate function  $w$  was introduced:  $w_I(x,t)$ ,  $w_{II}(x,t)$ ,  $w_{III}(x,t)$ . The differential equation of motion (7) was solved by means of the Fourier method (10), where  $W_i(x)$  is the form function,

$T_i(t)$  is the time function,  $i$  takes on a value from 1 to 3 according to each section of the rod.

$$w_i(x, t) = W_i(x)T(t) \quad (10)$$

It is evident that the parts vibrate with the same time frequency, thus, we could get rid of the index  $i$  in  $T_i(t)$ . For the time function we obtained Equation (11) for all three sections of the rod, with  $\omega$  being a natural frequency in rad/s,  $A$  and  $B$  being coefficients defining a phase.

$$T(t) = A\cos\omega t + B\sin\omega t \quad (11)$$

After the substitution of Equation (11) and (10) into Equation (7), the form equations (12) for parts I, III and II were delivered.

$$\begin{aligned} \frac{d^4 W_{II}}{dx^4} - \frac{F}{\rho A c^2} \frac{d^2 W_{II}}{dx^2} - \frac{\omega^2}{c^2} W_{II} &= 0 \\ \frac{d^4 W_{I,III}}{dx^4} - \frac{F}{\rho A c^2} \frac{d^2 W_{I,III}}{dx^2} + \left( \frac{K_f}{\rho A c^2} - \frac{\omega^2}{c^2} \right) W_{I,III} &= 0 \end{aligned} \quad (12)$$

Where for better visibility the ratio  $\frac{EI}{\rho A}$  was called  $c^2$ . Ordinary differential equations (12) were solved using the general solution given as Equation (13).

$$W_{I,II,III}(x) = C e^{sx} \quad (13)$$

Further, the algebraic equations (14) in coefficients  $s$  were obtained throughout substitution of the general solution (13) into the differential equations (12).

$$\begin{aligned}
s_{II}^4 - \frac{F}{\rho A c^2} s_{II}^2 - \frac{\omega^2}{c^2} &= 0 \\
s_{I,III}^4 - \frac{F}{\rho A c^2} s_{I,III}^2 + \left( \frac{K_f}{\rho A c^2} - \frac{\omega^2}{c^2} \right) &= 0
\end{aligned} \tag{14}$$

Each of Equations (14) provided correspondingly four solutions for  $s$ : two complex  $s_3 = \pm ik_3$  and two real roots  $s_4 = \pm k_4$  for the first equation, and four complex roots  $s_{1,2} = \pm k_1 \pm ik_2$  for the second one. All of the parameters  $s$  in a certain form contain  $\omega$ ,  $F$  and  $K_f$ . Still, to keep our expressions simplified, we used parameters  $s$  in the form functions for the natural modes of the tie-rod (15).

$$\begin{aligned}
W_I(x) &= C_1 e^{s_1 x} + C_2 e^{-s_1 x} + C_3 e^{s_2 x} + C_4 e^{-s_2 x} \\
W_{II}(x) &= C_5 e^{s_3 x} + C_6 e^{-s_3 x} + C_7 e^{s_4 x} + C_8 e^{-s_4 x} \\
W_{III}(x) &= C_9 e^{s_1 x} + C_{10} e^{-s_1 x} + C_{11} e^{s_2 x} + C_{12} e^{-s_2 x}
\end{aligned} \tag{15}$$

Substituting the forms (15) into twelve conditions (8), we hence obtained a homogeneous system of twelve equations containing twelve unknowns  $C_1 \dots C_{12}$ , which in a matrix form is expressed as Equation (16).

$$[M]\{C\} = \{0\} \tag{16}$$

In order to provide a non-trivial solution the determinant of the matrix M in (16) was supposed to be equal to zero (17), which resulted in a characteristic equation of the eigenvalue problem.

$$\det \begin{bmatrix}
s_1^2 & s_1^2 & s_1^2 & s_1^2 & 0 & 0 & 0 & 0 & 0 & 0 & 0 & 0 & 0 \\
s_1^3 & -s_1^3 & s_2^2 & -s_2^2 & 0 & 0 & 0 & 0 & 0 & 0 & 0 & 0 & 0 \\
e^{s_1 l} & e^{-s_1 l} & e^{s_2 l} & e^{-s_2 l} & -e^{s_1 l} & -e^{-s_1 l} & -e^{s_2 l} & -e^{-s_2 l} & 0 & 0 & 0 & 0 & 0 \\
s_1 e^{s_1 l} & -s_1 e^{-s_1 l} & s_2 e^{s_2 l} & -s_2 e^{-s_2 l} & -s_1 e^{s_1 l} & s_1 e^{-s_1 l} & -s_2 e^{s_2 l} & s_2 e^{-s_2 l} & 0 & 0 & 0 & 0 & 0 \\
s_1^2 e^{s_1 l} & s_1^2 e^{-s_1 l} & s_2^2 e^{s_2 l} & s_2^2 e^{-s_2 l} & -s_2^2 e^{s_1 l} & -s_2^2 e^{-s_1 l} & -s_2^2 e^{s_2 l} & -s_2^2 e^{-s_2 l} & 0 & 0 & 0 & 0 & 0 \\
s_1^3 e^{s_1 l} & -s_1^3 e^{-s_1 l} & s_2^3 e^{s_2 l} & -s_2^3 e^{-s_2 l} & -s_2^3 e^{s_1 l} & -s_2^3 e^{-s_1 l} & -s_2^3 e^{s_2 l} & -s_2^3 e^{-s_2 l} & 0 & 0 & 0 & 0 & 0 \\
0 & 0 & 0 & 0 & e^{s_1(l-l)} & e^{-s_1(l-l)} & e^{s_2(l-l)} & e^{-s_2(l-l)} & -e^{s_1(l-l)} & -e^{-s_1(l-l)} & -e^{s_2(l-l)} & -e^{-s_2(l-l)} & -e^{-s_2(l-l)} \\
0 & 0 & 0 & 0 & s_1 e^{s_1(l-l)} & -s_1 e^{-s_1(l-l)} & s_2 e^{s_2(l-l)} & -s_2 e^{-s_2(l-l)} & -s_1 e^{s_1(l-l)} & -s_1 e^{-s_1(l-l)} & s_2 e^{s_2(l-l)} & -s_2 e^{-s_2(l-l)} & s_2 e^{-s_2(l-l)} \\
0 & 0 & 0 & 0 & s_1^2 e^{s_1(l-l)} & -s_1^2 e^{-s_1(l-l)} & s_2^2 e^{s_2(l-l)} & -s_2^2 e^{-s_2(l-l)} & -s_1^2 e^{s_1(l-l)} & -s_1^2 e^{-s_1(l-l)} & -s_2^2 e^{s_2(l-l)} & -s_2^2 e^{-s_2(l-l)} & -s_2^2 e^{-s_2(l-l)} \\
0 & 0 & 0 & 0 & s_1^3 e^{s_1(l-l)} & -s_1^3 e^{-s_1(l-l)} & s_2^3 e^{s_2(l-l)} & -s_2^3 e^{-s_2(l-l)} & -s_1^3 e^{s_1(l-l)} & -s_1^3 e^{-s_1(l-l)} & s_2^3 e^{s_2(l-l)} & -s_2^3 e^{-s_2(l-l)} & s_2^3 e^{-s_2(l-l)} \\
0 & 0 & 0 & 0 & 0 & 0 & 0 & 0 & s_1^2 e^{s_1 l} & s_1^2 e^{-s_1 l} & s_2^2 e^{s_2 l} & -s_2^2 e^{-s_2 l} & -s_2^2 e^{-s_2 l} \\
0 & 0 & 0 & 0 & 0 & 0 & 0 & 0 & s_1^3 e^{s_1 l} & -s_1^3 e^{-s_1 l} & s_2^3 e^{s_2 l} & -s_2^3 e^{-s_2 l} & -s_2^3 e^{-s_2 l}
\end{bmatrix} = 0 \tag{17}$$

Equation (17) is to be solved for the natural frequencies  $\omega$  by means of, for instance, the Newton-Raphson method. Furthermore, the dispersion between analytically and experimentally determined frequencies can be minimized with respect to parameters  $F$  and  $K_f$ , analogically to the procedure described in the next sections. This approach in a closed form delivers solution for the sought axial load in tie-rod.

### 1.3.2 Numerical model and optimization procedure

Tie-rods were modelled in FEM software using beam elements, which allowed taking into account irregular cross-sections, added masses, elastic supports, etc. The FEM simulation was divided into two steps: as a first step a pretension load  $F$  was applied to the beam and as a second step the modal analysis was performed (see Chapter 4 for more details). The FEM model and analysis were parametric, since the tensile load and elastic bed parameters were the unknowns. Idea here was to “tune” these parameters, looking for a better match between results of physical tests and FEM simulations. Optimization criterion adopted was represented by the residual error between natural frequencies defined via experimental and numerical modal analyses [1-6]. The residual error  $R$  was calculated according to Equation (18), where  $p_k$  is a weight coefficient arbitrary assigned to a frequency number  $k$ . Minimum of the multi-parameter function  $R$  (18) delivered the optimal solution.

$$R = \sqrt{\sum_{k=1}^n p_k^2 (f_k^{\text{exp}} - f_k^{\text{FEM}})^2} \quad (18)$$

As a first iteration we analytically investigated the function  $R$  (18) for a tie-rod with fixed and/or simply supported conditions, with length  $L$  and axial load  $F$  being optimization parameters. On a reasonable range of optimization parameters the residual error (18) had only a forced minimum at the minimal value of the length parameter. The found absolute minimum was lying, however, below the measured length of a tie-rod. This behaviour proved the necessity of modelling more complex boundary conditions. However, this first iteration provided a rough idea of the sought axial load and we could set the range for  $F$  around this value.

Subsequently we modelled the elastic bed boundaries, representing a general condition of translational and rotational stiffness acting for the length  $l_f$ , as in the sketch displayed in Figure 1.1. Elastic bed consists of equispaced linear elastic springs each of stiffness  $k_f$ . Further the optimization has been done with respect to the sought axial load and the parameters of elastic foundation. We needed to provide sets of experimentally obtained frequencies, ranges and step sizes of optimization parameters and sets of weight coefficients  $p_k$  to the code in C that:

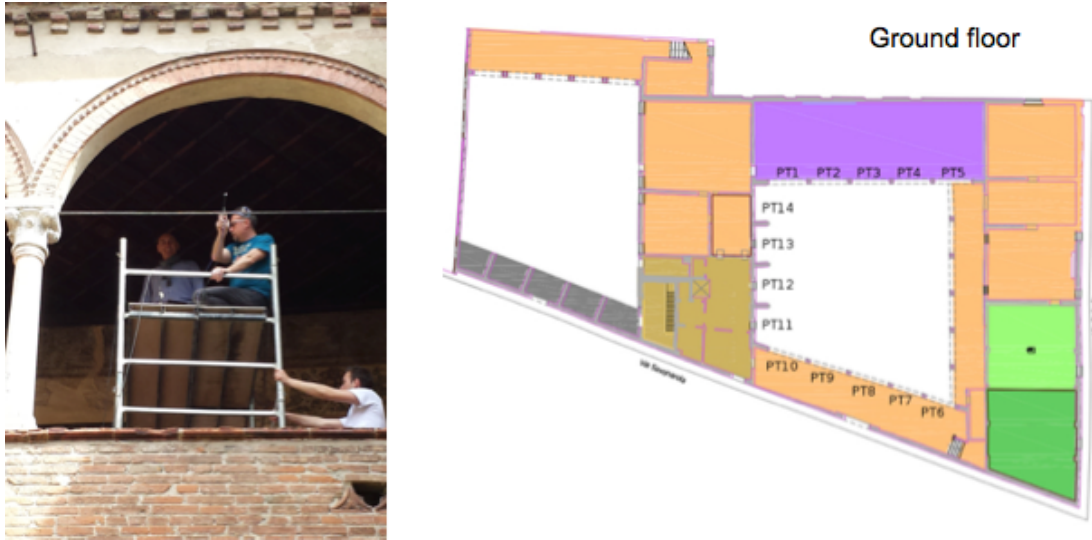
- forms a matrix of parameters;
- launches the FEM analysis for each nod of the grid, extracts and filters natural frequencies from the output;
- calculates the value of residual error (18) for each step;
- finds the local minimum of the function (18) and the corresponding combination of parameters including the sought tensile load;
- refines the grid of parameters and repeats the procedure again.

## 1.4 Application to a case study

The method described hereby was applied to investigation of tie-rods installed in “Casa Romei” located in Ferrara, Italy (see Figure 1.2 and Figure 1.3). Romei's House is a perfect example of a 15<sup>th</sup> century palace, in which you can see rich gothic decoration of the Late Middle Ages combine with elements of the Early Renaissance. Tie-rods have been placed in this building in different times along its existence, differ in dimensions and cross-section shapes.

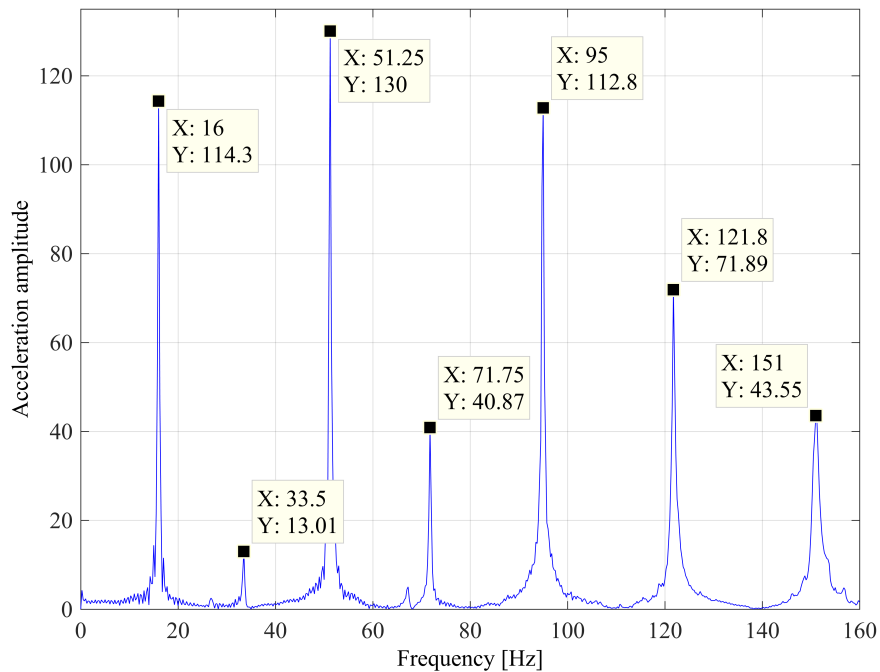


**Figure 1.2. Inner yard of Casa Romei and zoom of the ground floor tie-rods.**



**Figure 1.3. Our team during hammer excitation of a tie-rod; map of ground floor.**

First, measurements of geometrical characteristics and of natural frequencies were performed for each tie-rod. Then experimental acquisition was carried out to determine the natural frequencies from the analysis of response to dynamical excitation applied to tie-rods in horizontal plane; as an example, a frequency response function (FRF) for a ground floor tie-rod is shown in Figure 1.4.



**Figure 1.4. FRF plot (acceleration amplitude vs. frequency).**

For the further analysis, first four to six natural frequencies were identified for each tie-rod. Six eigenmodes are already providing an over constrained problem, besides that, identification of higher modes might appear inaccurate due to larger possible measurement errors. Material was assumed to be general iron with characteristics:  $E = 210$  GPa,  $\nu = 0.3$ ,  $\rho = 7850$  kg/m<sup>3</sup>.

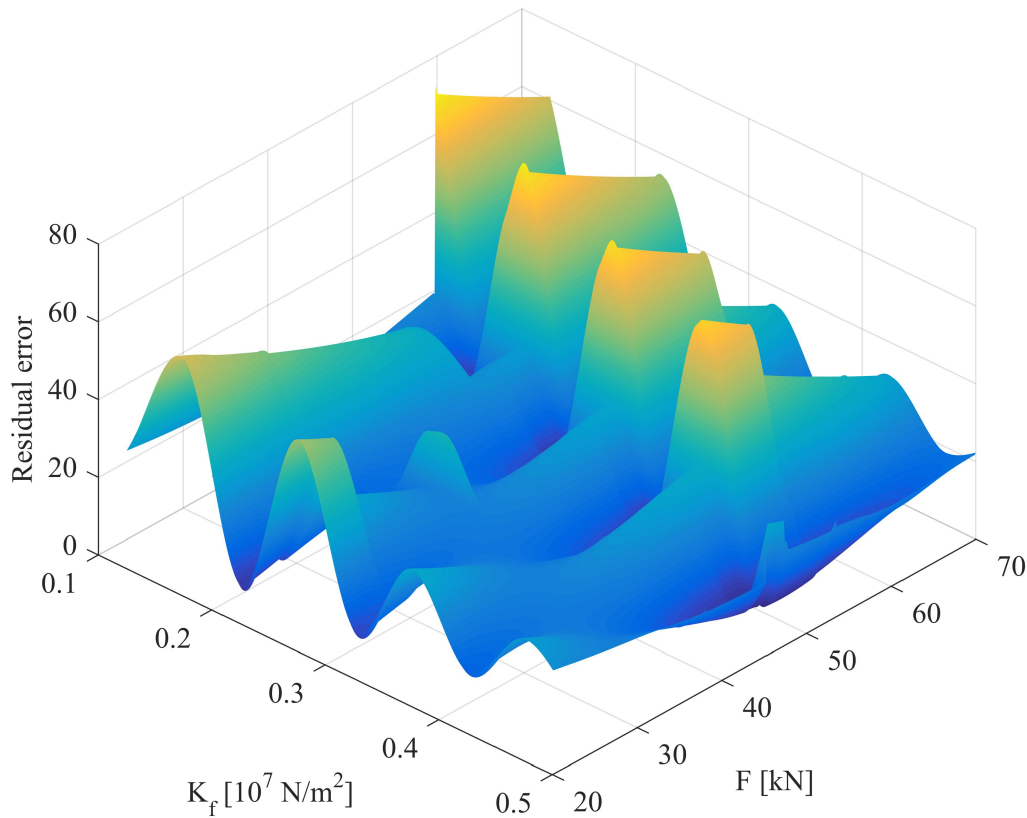
### 1.4.1 Load identification results

Table 1-1 summarizes the data on cross-section  $A$ , free length  $l$  and natural frequencies of the ground floor tie-rods (see Figure 1.3 for layout). Some of the frequencies in Table 1-1 are missing, due to the eventual position of the accelerometer over a modal node; in these cases higher frequencies were considered in the optimization process.

**Table 1-1. Experimental acquisitions.**

# Tie-rod	Cross-section $A$ [mm <sup>2</sup> ]	Length $l$ [mm]	Natural frequencies [Hz]					
			I	II	III	IV	V	VI
PT1	52x9	3178	15.30	-	49.00	-	92.30	-
PT2	51x9	3233	16.80	-	53.80	-	98.80	-
PT3	52x10	3228	16.30	-	53.80	-	103.00	-
PT4	51x10	3218	16.00	33.50	51.30	71.80	95.00	121.80
PT5	53x10	3188	5.50	-	28.30	-	65.50	91.00
PT6	50x20	2748	21.75	49.00	85.25	131.20	188.50	255.20
PT7	50x20	2768	20.00	45.50	80.00	123.80	179.20	242.20
PT8	50x20	3358	14.75	32.75	55.75	85.25	121.20	176.50
PT9	50x20	3248	15.50	34.25	58.75	90.00	128.00	173.00
PT10	50x20	3388	17.75	38.00	63.25	94.75	133.00	177.50
PT11	50x12	3440	13.25	29.75	51.25	78.25	111.50	150.80
PT12	50x12	3298	14.50	30.25	48.25	69.25	94.00	122.20
PT13	50x12	3140	13.75	-	47.25	-	95.75	-
PT14	50x12	2510	19.25	46.50		84.00	-	134.50

A typical graphic scenario of the optimization process is depicted in Figure 1.5. Here several values of the function  $R$  (18) were plotted vs. axial load  $F$  and distributed stiffness of the elastic bed  $K_f$ , for the tie-rod PT2. The length of elastic bed  $l_f$  (see Figure 1.1) was kept constant. It is notable that many minima are present in correspondence to certain  $F$ - $K_f$  couples and one of them is a local minimum. The grid of parameters  $F$  and  $K_f$  was then reduced around it, in order to refine the search of the optimal values.

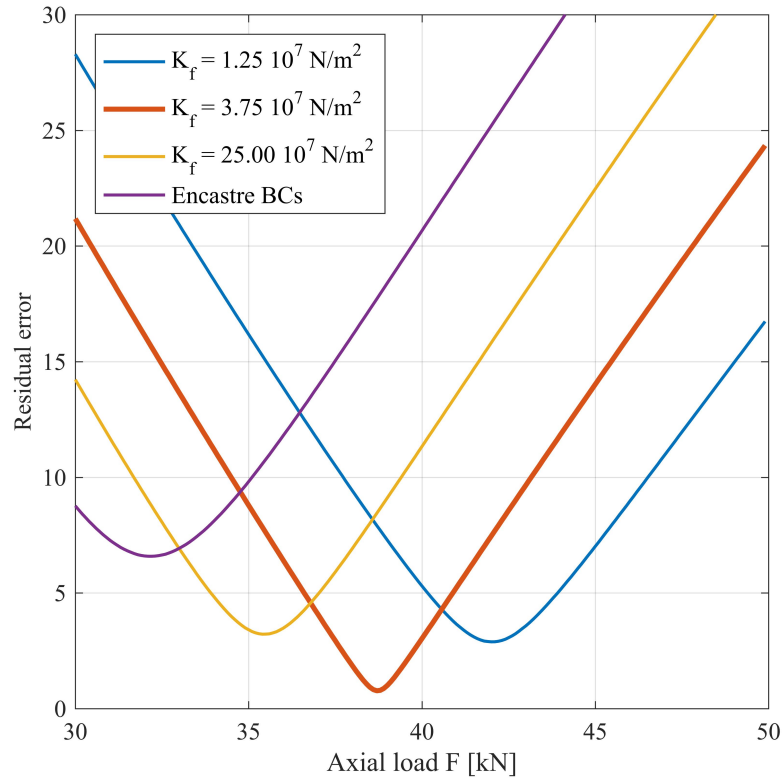


**Figure 1.5. Residual error function as function of elastic bed stiffness and axial load.**

Naturally, the so-defined minima of the residual error (18) were not independent; nevertheless, once the main parameter (axial load  $F$ ) was optimized, the influence of stiffness of constraints on the first parameter was nearly negligible.

The model with elastic foundation boundaries delivered improvement of results as illustrated in Figure 1.6. The plot shows residual error curves for the tie-rod PT4 at different values of stiffness  $K_f$  compared to the clamped boundaries. It indicates that the minimum of the error (18) decreases from 6.59 (encastré BCs) to 0.77 for the optimal stiffness  $K_f = 3.75 \times 10^7 \text{ N/m}^2$ . The corresponding optimal value of the axial load in this tie-rod increases by 20% from 32.20 kN (encastré BCs) to 38.70 kN (elastic bed). We presume that a model with simple clamped boundaries underestimated the axial load, thus, the proposed method reveals to be conservative for the load estimation.





**Figure 1.6. Influence of the elastic bed on the axial load determination.**

Table 1-2 summarizes the results of the computation process of the reported case study.

**Table 1-2. Summary of results.**

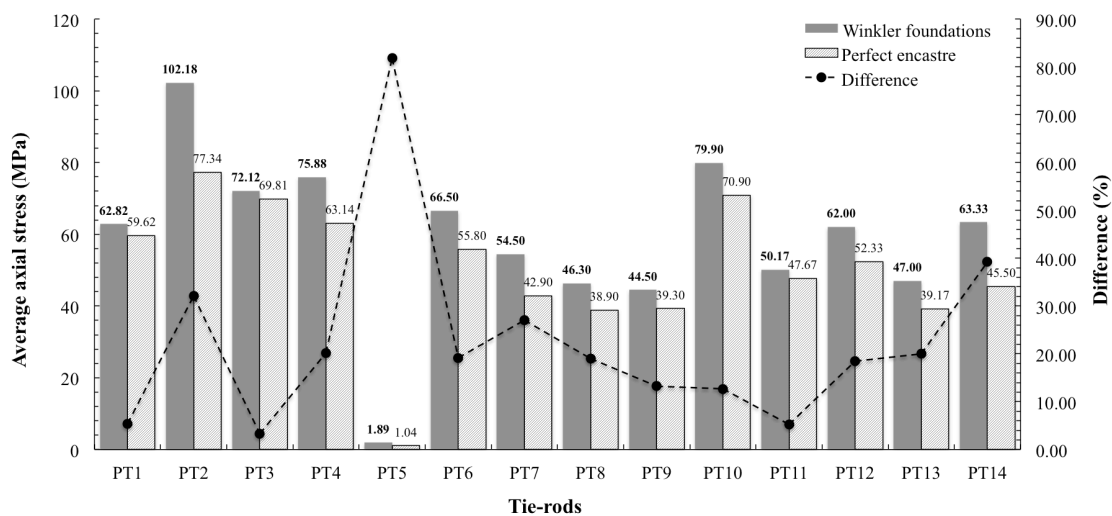
# Tie-rod	Axial load $F$ [kN]	Stress [MPa]	Bed stiffness $K_f$ [ $10^7 \text{ MN/m}^2$ ]	Residual error
PT1	29.40	62.82	50.00	0.31
PT2	46.90	102.18	0.48	6.04
PT3	37.50	72.12	253.00	3.95
PT4	38.70	75.88	3.75	0.77
PT5	1.00	1.89	26.75	1.17
PT6	66.50	66.50	113.00	0.48
PT7	54.50	54.50	57.50	1.43
PT8	46.30	46.30	60.00	6.60
PT9	44.50	44.50	62.50	7.33
PT10	79.90	79.90	76.00	2.22
PT11	30.10	50.17	99.50	6.53
PT12	37.20	62.00	4.25	0.48
PT13	28.20	47.00	5.50	0.27
PT14	38.00	63.33	2.13	5.58

### 1.4.2 Analysis of the results

Tensile loads cause normal stresses that need to be estimated for evaluation of reliability and integrity of tie-rods. This safety assessment can be carried out based on the values of average axial stress  $\bar{\sigma}_{k,N}$ , to which each tie-rod is subjected. The stress was calculated with respect to the optimal axial load  $F_{k,opt}$  and the minimum cross-section area  $A_{k,min}$ :

$$\bar{\sigma}_{k,N} = \frac{F_{k,opt}}{A_{k,min}} \quad (19)$$

This stress (19) is average since it assumes a uniform section without taking into consideration such local effects as screws, fillets, holes, joints, etc., that tie-rods might incorporate. However, these stress concentrators should be considered, if present, for correct local strength verification, eventually via FEM analysis.

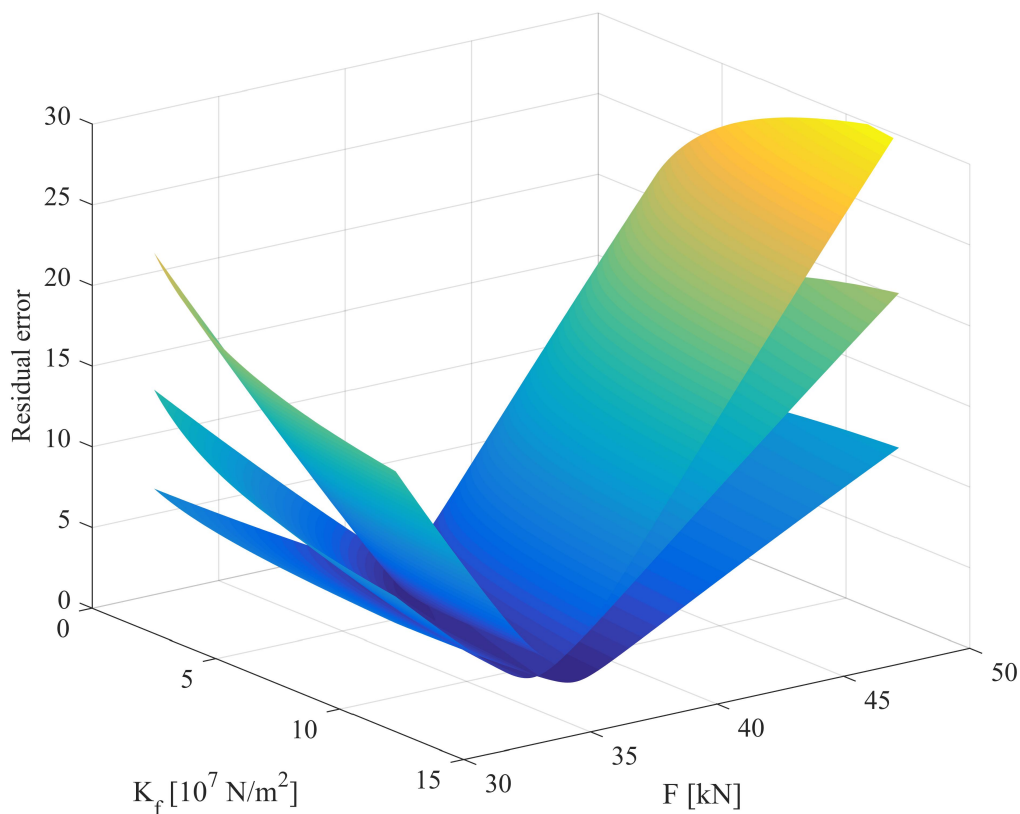


**Figure 1.7. Average stress state in tie-rods: comparison between encastred and elastic foundation boundaries.**

In Figure 1.7 the stresses in rods PT1-PT14 are plotted. Apart from PT5, all tie-rods worked properly and below the allowable stress of 120 MPa for ancient iron. Rod PT5 was evidently unloaded, which indicated that there was either some damage or

malfunction at the anchorages, the issue has been stated in the appropriate technical report of the case study. For comparison, Figure 1.7 reports also average stresses calculated for the case of encastré boundary conditions: safety improvement was definitely confirmed.

In Section 1.2.2 we introduced the residual error (18) to compute “distance” between experimental and numerical frequencies. In the formula the difference (in Hz) between each couple of frequencies is multiplied by a weight coefficient  $p_k$  in order to attribute higher or lower importance to some frequencies rather than others. The set of weight coefficients was arbitrary chosen, but generally higher importance has been given to the first frequencies.



**Figure 1.8. Residual error functions for sets of weight coefficients  $W_1, W_2, W_3$ .**

A sensitivity analysis has been conducted to evaluate the influence of weight coefficients on our results. The plot in Figure 1.8 shows three residual error functions for the tie-rod PT4 corresponding to three different sets of weight coefficients. The sets taken into consideration were  $W_1 = \{1,1,1,1,1,1\}$ ,  $W_2 = \{10,1,1,1,1,1\}$ ,  $W_3 =$

$\{4,1,0.5,0.25,0.1,0.05\}$ . We see that each set generated a different interpolated surface, however, the error reached minimum around the same value of the sought axial load, as reported in Table 1-3. Many other reasonable sets of weight coefficients have been tested, confirming their low influence on the resulting axial load, which proved the stability of our model with respect to these arbitrary assigned parameters.

**Table 1-3. Results of computation with three sets of weights for the tie-rod PT4.**

Sets of weight coefficients	Axial load $F$ [kN]	Bed stiffness $K_f$ [ $10^7$ MN/m <sup>2</sup> ]	Natural frequencies [Hz]					
			I	II	III	IV	V	VI
$W_1 = \{1,1,1,1,1,1\}$	39.00	3.50	16.03	32.91	51.37	72.03	95.32	121.53
$W_3 = \{4,1,0.5,0.25,0.1,0.05\}$	38.60	4.50	16.04	32.95	51.48	72.25	95.69	122.13
$W_2 = \{10,1,1,1,1,1\}$ optimal values	38.70	3.75	16.00	32.85	51.31	71.97	95.28	121.55
$W_2$ , Encasté BCs	32.20	$\infty$	15.68	32.47	51.33	72.97	97.91	126.50
Experimentally defined frequencies			16.00	33.50	51.30	71.80	95.00	121.80

## 1.5 Conclusions

In this Chapter a procedure for axial load identification in structural tie-rods was demonstrated and approved via an experimental study of an ancient mansion. The method is based on a tie-rod model represented by a beam with ends supported by an elastic Winkler-type foundation. The elastic bed was used to simulate the contact condition between a tie-rod and a masonry wall. The proposed method consisted of an experimental and a computational stage. The experimental part was a relatively simple vibrational test for natural frequencies identification. The computational part was an optimization procedure for axial load estimation based on finite element modelling. The optimization has been done with respect to two parameters: the sought axial load and the distributed stiffness of the elastic bed at the boundaries. The technique provided a solution for uncertain boundary conditions and is capable of identifying axial load with high accuracy.

Investigation of the behaviour of natural frequencies depending on the parameters showed that axial load tends to shift the set of frequencies (higher the load – higher the frequencies), while the elastic foundation stiffness changes the “distance” between natural frequencies.

As a result consideration of elasticity at anchorages exhibited increase in axial load by up to 40%. This means that assumption of simple boundary conditions is not sufficient for modelling a tie-rod dynamic response. The sensitivity analysis has proved that the optimization result was stable to variation of weight coefficients and was converging to the same axial load. Thus, the method has been approved in practice and is suitable for in situ identification of axial load in ancient tie-rods.

---

# Chapter 2

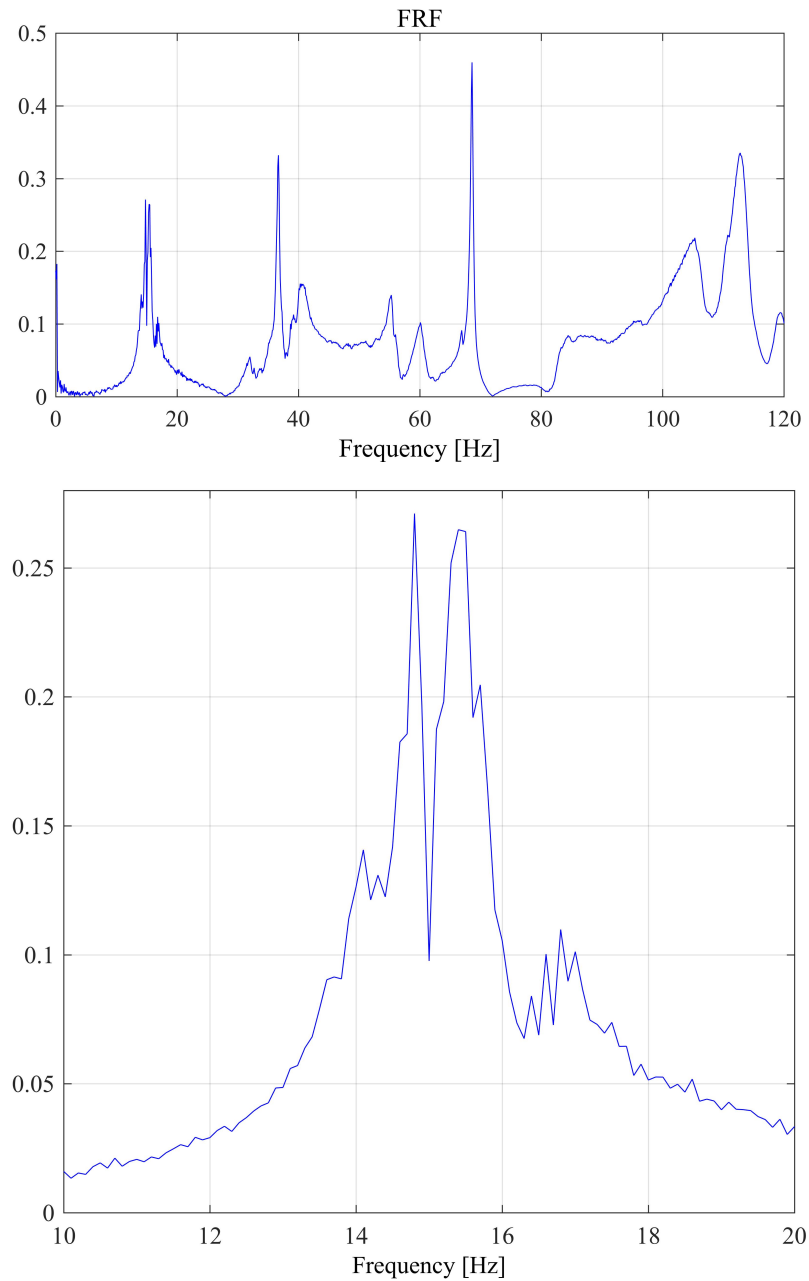
## Damage identification in tie-rods

*This Chapter introduces an experimental setup for static and dynamic testing of tie-rods and a method of defect detection. The method is based on a non-destructive vibration analysis: a test with an instrumented impact hammer excitation and accelerometric acquisition of the response. Subsequent analysis of the modal parameters permits to draw conclusions about the stress state condition and structural integrity of the tested tie-rods.*

### 2.1 Introduction

The case study described in Chapter 1, as well as other experiments executed by the team of the Department of Industrial Engineering [1-6], were quite efficient in the evaluation of axial load in tie-rods. For example, the tie-rod PT5, which was evidently unloaded, was supposed to be replaced or its fixes had to be tightened. These facts were documented and reported to the Municipality that requested this investigation. However, we could only assess the loading condition and, as for the structural integrity of the tie-rods, no precise conclusion could be made based on the obtained results,

rather than from the superficial inspection. At the same time, for certain tie-rods the FRF exhibited “strange” behaviour characterized by broken or doubled peaks as shown in Figure 2.1.



**Figure 2.1. FRF of a tie-rod with a “broken peak”.**

The presence of this nonlinear behaviour in our opinion is an indication of structural discontinuities. For the purpose of investigation of these phenomena an idea of a unique experimental setup emerged.

In a real building there are no two identical tie-rods from which a similar response can be expected. Usually they are installed in different periods, vary in cross-section shapes, lengths and anchorages. The need to compare dynamical responses of equivalent elements, one of which incorporated a damage, lead to an idea of an experimental rig constructed in the laboratory of the Department of Industrial Engineering at the UNIPR. The proposed setup enabled testing of a healthy, (the continuous, “healthy”, as we called it) beam, along with another identical beam, though with a controlled and known defect (the “damaged” beam).

Vibration analysis appears to be one of the most economic and easily accessible ways of non-destructive testing. It does not require very expensive equipment (compared to other non-destructive testing techniques), is executed via simple short tests and the tests output is also elaborated in a blink. Hence, considering the experience of the Department of Industrial Engineering in NDT and vibration analysis we chose it as a base for the damage identification method proposed hereby.

## **2.1 State of the art in damage identification of beams**

Most of the members of engineering structures operate under loading conditions, which may cause damages or cracks in overstressed zones. The presence of cracks in a structural member, such as a beam, causes local variations in stiffness, the magnitude of which mainly depends on the location and depth of the cracks. These variations, in turn, have a significant effect on the vibrational behaviour of the entire structure. To ensure the safe operation of structures, it is extremely important to know whether their members are free of cracks, and should any be present, to assess their extent. The procedures often used for detection are direct procedures such as ultrasound, X-rays, etc. However, these methods have proven to be inoperative and unsuitable in certain cases, since they require expensive and minutely detailed inspections as stated by *J. Silva et al.* in [32]. To avoid these disadvantages, in recent decades, researchers have focused on more efficient procedures in crack detection using vibration-based methods



---

summarized in [33] by *S. Doebling et al.* Modelling of a crack is an important aspect of these methods.

In case of dynamic loading a crack does not stay open or closed all the time: the conditions on the crack surface changes during vibration. This phenomenon is called “breathing” and has to be modelled in order to accurately represent the dynamics of a cracked beam and to understand the damage state as discussed by *A. Bouboulas et al.* in [34]. In their book the authors investigated the vibrational behaviour of a beam with a non-propagating edge crack. They employed a two-dimensional beam finite element model. The breathing crack was simulated as a full frictional contact problem between the crack surfaces, while the region around the crack was discretized into a number of conventional finite elements. This nonlinear dynamic problem was solved using an incremental iterative procedure. This study was applied for the case of an impulsive loaded cantilever beam and based on the derived time response, conclusions could be extracted about the crack state. Furthermore, the time response was analysed by Fourier and continuous wavelet transforms to show the sensitivity of the vibrational behaviour for both a transverse and slant crack of various depths and positions.

The fact that a crack or a local defect affects the dynamic response of a structural member is known long ago. Some crack identification methods using fracture mechanics have been reported by *T. Chondros and A. Dimarogonas* supported by analytical and experimental results [35-36]. *T. Chondros* combined the fracture mechanics results with the local flexibility model for the vibration analysis of cracked beams and frequency spectral methods of crack identification in various structures [37]. Crack local flexibility coefficients for the vibration analysis of cracked beams and rods are presented in the books of *A. Dimarogonas et al.* [38-39]. This approach suffers from various limitations mainly from the fact that the modification of the stress field induced by the crack is decaying with the distance from the crack. *T. Chondros* discussed the correlation between defect position and size and the stiffness change affecting this approach in [40].

The breathing causes variations of local stiffness, which are not only time-/frequency- but also amplitude-dependent. Breathing mechanism is very complex and, normally, suggested models are based on certain assumptions that postpone them from the reality, e.g. considering only two states: full opening or complete closing of a crack.

On the other hand, considering the time-dependent contact condition is overly time consuming in terms of computing. *A. Dimarogonas* summarized over 500 papers in his state-of-art review [41] and came to a conclusion that a consistent theory of cracked beam vibrations was yet to be developed and most of the unanswered questions concern the breathing mechanism: crack opening and closing. Most of the reviewed studies dealt with numerical and analytical modelling of the cracked structure motion throughout considering the nonlinearities in the stiffness of the cracked section.

The majority of published studies assume that the crack in a structural member always remains open during vibration as in studies by *S. Christides, A. Dimarogonas, T. Chondros, M. Krawczuk, A. Bouboulas et al.* [42-46]. The damage detection methods that adopted the open cracks hypothesis are based on the identification of changes in modal parameters of the damaged structure: decrease of frequencies, increase of damping ratios, changes of modal shapes, etc. These techniques limited to the linear field were introduced and discussed along with the mentioned above authors *A. Dimarogonas and T. Chondros* by *P. Rizos, Y. Narkis, M. Mahmoud, F. Tomasel, J. Sinha, F. Sayyad, E. Douka, M. Kim, X. Chen, A. Yan et al.* [47-58]. However, the assumption of an open crack may not be valid when dynamic loadings are dominant. In this case, the crack breathes (opens and closes) regularly during vibration, inducing variations in the structural stiffness. *P. Gudmundson* shows that these variations cause the structure to exhibit non-linear dynamic behaviour [59]. The main distinctive feature of this behaviour is the presence of higher harmonic components. In particular, a beam with a breathing crack shows natural frequencies between those of a non-cracked beam and those of a faulty beam with an open crack. Therefore, in these cases, vibration-based methods should employ breathing crack models to provide accurate conclusions regarding the state of damage.

Several researchers like *P. Cacciola, G. Muscolino, S. Benfratello, K. Sholeh et al.* [60-62] have developed breathing crack models considering only the fully open and fully closed crack states. However, experiments performed by *R. Clark et al.* indicated that the transition between these two crack states does not occur instantaneously [63]. *O. Abraham et al.* represented the interaction forces between two segments of a beam, separated by a crack, using time-varying connection matrices [64]. These matrices were expanded in Fourier series to simulate the alternation of a crack opening and closing.

However, the implementation of this study requires excessive computer time. *S. Loutridis, E. Douka and L. Hadjileontiadis* considered a simple periodic function to model the time-varying stiffness of a beam [65-66]. However, this model is limited to the fundamental mode, and thus, the equation of motion for the beam must be solved.

Finite element formulation of a beam with transverse crack under complex loading is presented by *P. Saavedra et al.* in [67]. The new stiffness matrix with the local variation in flexibility caused by the presence of a crack is deduced using the strain energy density function given by the linear elastic fracture mechanics approach. A free-free beam with rectangular cross-section is considered. The authors obtain and solve numerically the nonlinear equations of motion. To avoid singularities and numerical uncertainties, the stiffness matrices of a cracked section and of “healthy” elements are combined. A simple crack breathing mechanism is considered: complete opening or closure, which leads to only two possible states of the stiffness matrix and a step-type variation. The authors show that under a harmonic load a cracked beam exhibits addition peaks in the FRF that correspond to the multiples of the excitation frequency. However, these nonlinearities in the response can be as well caused by other variations in the damping and stiffness properties.

A realistic model of a breathing crack is difficult to create due to the lack of fundamental understanding about certain aspects of the breathing mechanism. This involves not only the identification of variables affecting the breathing crack behaviour, but also issues for evaluating the structural dynamic response of the fractured material. It is also not yet entirely clear how partial closure interacts with key variables of the problem. The actual physical situation requires a model that accounts for the breathing mechanism and for the interaction between external loading and dynamic crack behaviour. When crack contact occurs, the unknowns are the field singular behaviour, the contact region and the distribution of contact tractions on the closed region of the crack. The latter class of unknowns does not exist in the case without crack closure. This type of complicated deformation of crack surfaces constitutes a non-linear problem that is too difficult to be treated with classical analytical procedures. Thus, a suitable numerical implementation is required when partial crack closure occurs.

*S. Andrieux and C. Varé* constructed a lumped cracked beam model from the three-dimensional formulation of the general problem of elasticity with unilateral contact

conditions on the crack lips [68]. The problem of a beam with an edge crack subjected to a harmonic load was considered by *A. Nandi and S. Neogy* in [69]. The breathing crack behaviour was simulated as a frictionless contact problem between the crack surfaces. Displacement constraints were applied to prevent penetration of the nodes of one crack surface into the other crack surface. *U. Andreaus et al.* studied the problem of a cantilever beam with an asymmetric edge crack subjected to a harmonic load using two-dimensional finite elements [70]. Breathing of the crack was simulated as frictionless contact between the interacting surfaces. The proposed damage identification method is based on the evaluation of the nonlinear characteristics of the system response. The modification of the response with respect to the linear one was outlined: in particular, excitation of sub- and super-harmonics, period doubling, and quasi-impulsive behaviour at crack interfaces. Thanks to a forward analysis the ratio between the main harmonic and a particular sub or super harmonic in the response, used as damage indicator, was studied as the damage position and depth changes. These data are collected in the Harmonic Damage Surfaces (HDS) that describe the dependency between the indicators and the damage.

Encouraged by these results, *O. Giannini et al.* generalize in their paper [71] refined the works of *A. Chatterjee, U. Andreaus & P. Baragatti, A. Bovsunovsky et al.* [72-74] by using more than one vibration mode of the structure for the crack identification. In fact, each mode is sensitive to the location of the damage in its own way. In this frame, the concept of modal-effective damage was introduced to detail the fact that a crack positioned close to curvature nodes does not affect that mode, while a breathing crack in a curvature antinode has a large effect on the dynamics that is detectable by sub- and super-harmonics in the response.

In [74] *U. Andreaus and P. Baragatti* studying the harmonic response of cracked beam considered the qualitative characteristics: phase portrait distortions, sub- and super-harmonic components in the Fourier spectrum, and curved shape of the modal line, along with quantitative parameters, such as the eccentricity and the excursion of the orbit, and the harmonic amplitude in the spectrum. Then, an identification procedure was proposed which was based on the intersection of constructed surfaces, which allowed to identify the structural damage.

Further in [75] the same authors proposed an experimental method of fatigue cracks detection in steel beams. Performing an impact test and a test with a shaker, the authors determined the fundamental natural frequency and then recorded a time-history response to a harmonic excitation with the frequency equal to one-third, half and double of the fundamental one. Furthermore the qualitative and quantitative analysis of the response and the Fourier spectra of the response are carried out using nonlinear damage identifiers. The tests were limited to short beams with rectangular cross-sections due to the peculiarities of the experimental set-up and, thus, the method in most cases cannot be applied in situ.

Besides of the scientists *S. Andrieux, C. Varé, A. Bovsunovsky, S. Loutridis, E. Douka and L. Hadjileontiadis, et al.* mentioned above the closure effects associated with “breathing” behaviour were also exploited by researchers that dealt with the so-called fatigue and breathing cracks, among of which are *C. J. Sundermeyer, M. Kisa, A. Rivola, S.L. Tsyfansky, F. Leonard, C. Surace, S. Benfratello, V.K. Nguyen, Z. Peng, et al.* [61, 65-66, 68, 78–87]. Relatively few papers analysed the nonlinear responses of damaged beams taking into account the effect of the alternation of crack opening and closure.

*U. Andreaus and P. Baragatti, F. Leonard et al.* extended the application of the linear method (i.e. the changes of the modal parameters) developed in the open crack damage scenario also to the breathing crack case [76, 82]. One of the main disadvantages of these techniques is the quantitatively small difference between the response of intact and defective structures, especially if the damage consists in a fatigue crack.

A more recent research trend suggests that the nonlinear characteristics of the motion and the distortions of the forced response of cracked structures must be accorded increasing importance. Several techniques have been developed by *S. Benfratello et al., A. Rivola et al.* in order to detect the damage, using nonlinear approaches such as the stochastic analysis [61, 80,], *V. Nguyen et al.* and *S. Zhong, & S. Oyadiji* proposed the usage of the wavelet transform [85, 90-91], *F. Leonard et al.* used the worm transform and the phase spectrogram [82], *S. Loutridis, E. Douka and L. Hadjileontiadis* developed their research based on the empirical modal decomposition, the Hilbert–Huang Transform and the instantaneous frequency [65-66], *Z. Peng et al.* used the

Volterra series [86-87], *V. Matveev et al.*, on the other hand, used the nonlinear distortions [88], the proper orthogonal decomposition was used by *D. Chelidze et al.* [77], the principal component analysis – by *A. Yan et al.* [89].

*N. Bachschmid et al.* studied the effect of a helicoidal crack on the dynamic behaviour of a rotating shaft [92]. This study used a very accurate and simplified model that assumes linear stress and strain distributions to calculate the breathing mechanism. The determination of open and closed parts of the crack was performed through a non-linear iterative procedure.

*T.G. Chondros et al.* reported results of two independent evaluations of the fundamental frequency of lateral vibrations of a beam with a single-edge surface crack: a numerical solution based on the continuous cracked beam vibration theory, and an asymptotic solution for the breathing crack [93]. These analytical results were correlated with experimental results obtained on simply supported aluminium beams with open fatigue cracks and breathing cracks respectively. Numerical and experimental results showed a substantial variation of the frequency change for a cracked beam with an open-edge crack, and for a breathing crack computed with the analytical method. The changes in vibration frequencies for a fatigue-breathing crack appeared to be smaller than the ones caused by open cracks. The eigenfrequency changes due to a breathing edge-crack were shown to depend on the bi-linear character of the system.

The above state of art review shows that numerous papers can be found on finite element modelling and analytical studies of cracked beams vibrations. Some of them present a substantial correlation with experimental measurements but under strictly limited conditions. In case of tie-rods the beams are long and slender with uncertain boundary conditions and most importantly, for safety, financial and ergonomic and reasons they need to be tested on-site.

Most of the researchers focused on studying and modelling of the nonlinear dynamic response of cracked structures to primary harmonic excitation. The majority of these models and, subsequently, damage identification techniques, require known boundary conditions and absence of other nonlinearities in the system: like added masses, complex uncertain boundary conditions, elastic supports, springs, dashpots, etc. Besides that being stated, these methods are mostly not applicable *in situ*: on metal beams that are still functioning as a part of construction and should not be dismantled, but are

supposed to undergo regular monitoring and checks. The research presented here aims to develop a simple, clear and brief procedure of experimental acquisition and data analysis for structural damage identification in tie-rods.

## **2.2 The experiment: general concept and execution**

The vibration tests were first to be performed on a “healthy” long metal beam (with no damages or cracks) in order to extract the natural frequencies of the beam subjected to various axial loads in a certain range. Furthermore, the same tests were repeated on a “damaged” beam with an artificially introduced controlled damage.

The concept of the experiment was to compare the responses of the healthy and the damaged beams in order to outline the tendencies in their behaviour depending on the axial load and the defect type, and, subsequently, to draw the appropriate conclusions that could be useful for in situ damage identification in the real tie-rods installed in buildings.

### **2.2.1 Damage representation**

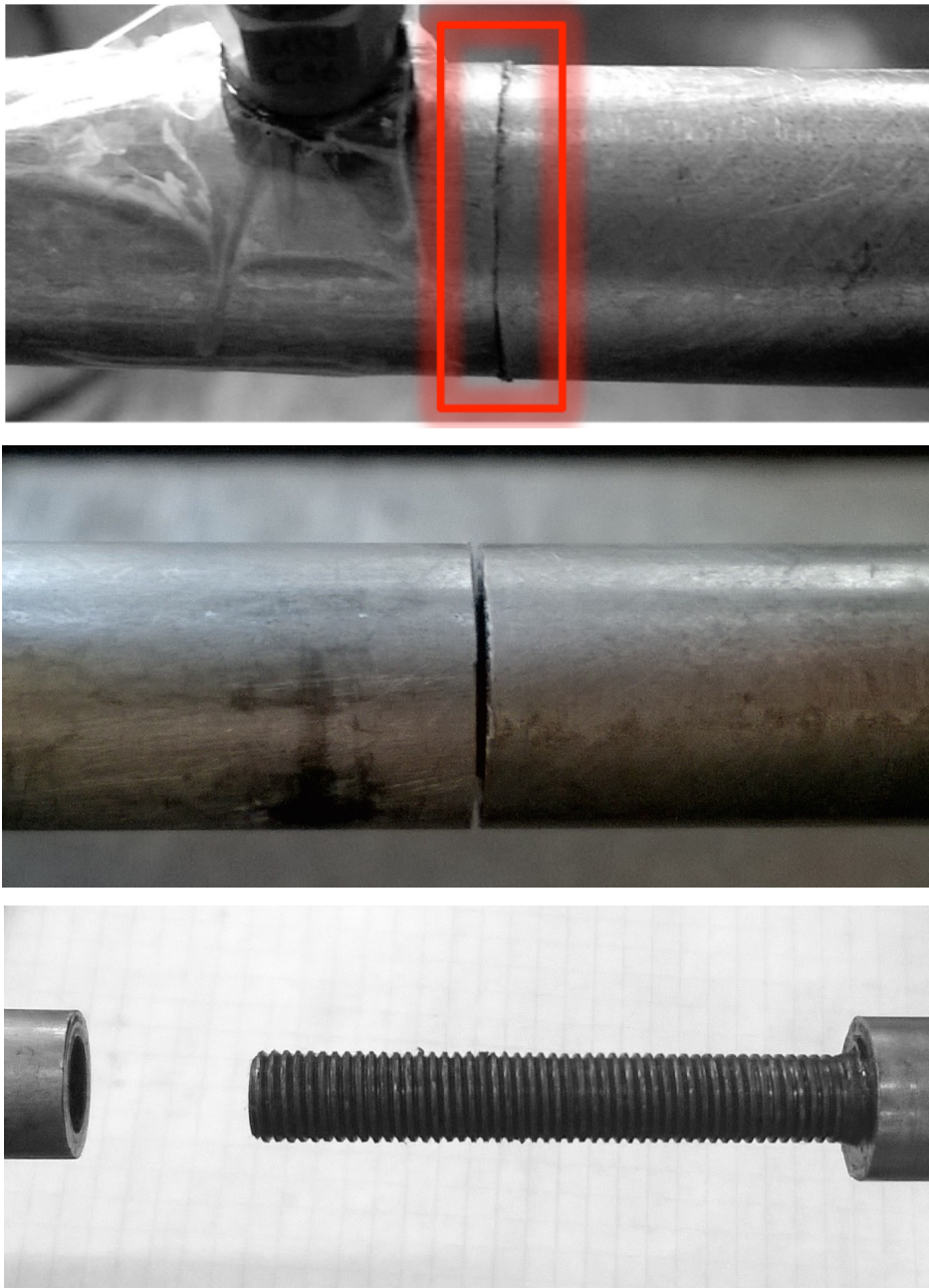
A task to introduce an artificial crack damage into a structure is not trivial at all. On one hand, if a cut in a beam is made with a machine tool it will simply be a notch characterized by a known stress concentration but the surfaces of the cut will not be in contact. On the other hand, there is no equipment, which could enable introducing a crack into a slender three-meter long beam. These factors made the authors think of an alternative way to physically model a crack damage. The artificial damage was represented by a bolt connection of two parts of the beam. Basically, a beam of the same cross-section and material as the “healthy” one was cut in two and a thread and a corresponding hole were carved to create the bolt connection. The two parts connected together formed the “damaged” beam of the same length as the “healthy” one. Figure 2.2 pictures the “damage” when the connection is tightened, loose and two parts separated.

The M8-type bolt between the two parts could be tightened with an adjustable torque using a torque wrench at one edge of the beam. For M8 thread the nominal torque is 25 Nm, other values were tested as well: 10, 15 and 20 Nm. Torque application at the junction between two parts of this beam creates contact pressure on the faces of the joint. When the “crack” is closed so that the surfaces come in contact with one another, the torque causes adhesion and contact friction. Different torques create correspondingly different adhesion on the contact surfaces of the beam. This means that different axial tension is required to overcome the contact pressure and separate the contact surfaces. This is similar to what happens when a real crack is opening in a tie-rod.

The modelled damage is most representative for a *surface ring-shaped crack* in a round bar. The equivalent crack shapes, stress intensity factors and compliances are further reviewed in Chapter 3.

More details on the measurement chain, equipment specifications and calibration procedures are given below in Section 2.3.2 in a step-by-step description.





**Figure 2.2. Two parts of the beam with a bolt connection.**

## 2.2.2 Experimental set-up

The list of parts and equipment used in the experiment was following:

- 1) Supporting system of the beam
- 2) Hydraulic lift
- 3) Modules for data acquisition
- 4) Strain gauge
- 5) Load cell
- 6) Impact hammer
- 7) Accelerometer
- 8) Torque wrench
- 9) Comparator with a stand
- 10) Other additional instruments

Two types of beams were tested during the experiment: the “*healthy*” beam and the “*damaged*” beam. Some of their basic properties are listed below in Table 2-1.

**Table 2-1. Beam properties.**

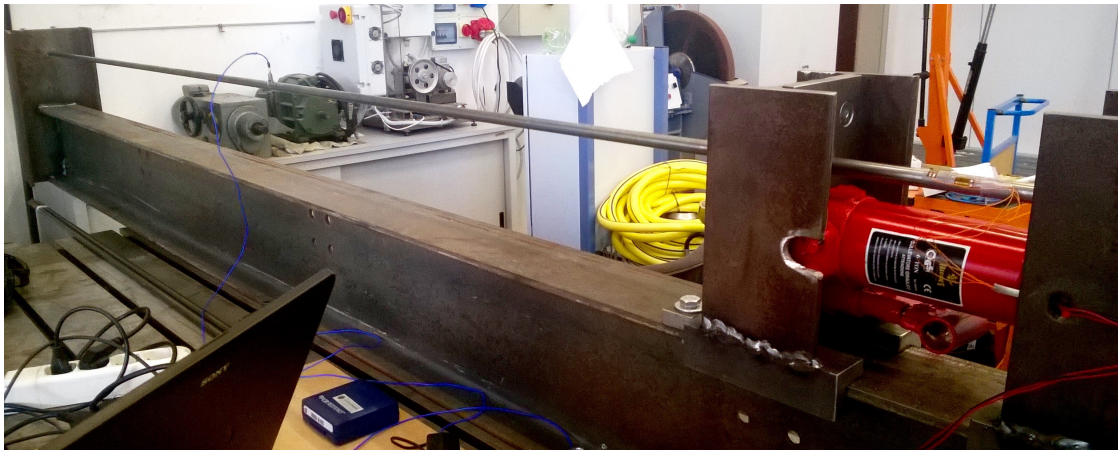
Material: structural steel S235	
Density	$\rho = 7850 \text{ kg/m}^3$
Young's modulus	$E = 200 \text{ GPa}$
Poisson's ratio	$\nu = 0.3$
Yield strength	$\sigma_Y = 235 \text{ MPa}$
Tensile strength	$\sigma_U = 360 - 510 \text{ MPa}$
Beam length	2760 mm
Cross-section diameter	$d = 16 \text{ mm}$
Maximum allowable stress	$\sigma_{\text{all}} = 196 \text{ MPa}$
Maximum allowable tensile force (healthy beam)	$F_{\text{all}} = \sigma_{\text{all}}A = 40 \text{ kN}$
Maximum allowable tensile force (damaged beam)	10 kN

### 2.2.2.1 Supporting system of the beam

The supports were mounted on a steel foundation bar IPE 160 and were crafted from the same type of profile. The left support was soldered to the foundation bar. The right support was able to move along the rail of the foundation beam. This enabled the ability

to regulate the axial tension in the beam applied via a manual hydraulic lift inserted between the right support and another support fixed on the foundation bar (see Figure 2.3). This other support had a hole of a diameter large enough to avoid contact with the beam under testing.

The beam was fixed in the appropriate holes made in the supports with nuts in a way close to the encastré boundary conditions. The whole assembly was placed on a heavy isolated steel table.



**Figure 2.3. Beam installed in the supporting and tensioning system.**

#### **2.2.2.2 Hydraulic lift**

The axial loading of the beam was powered by the Falcon's manual hydraulic lift with maximum capacity of 6 ton (58,86 kN). The principle of this construction was following: with a handle inserted in the appropriate holder (as shown in the photo in Figure 2.4), one manually starts the in-and-out motion of the shaft, which leads to "pumping" of the oil inside the lift. As the pressure of the liquid increases, the tip of the lift displaces the right support creating in the longitudinal direction, thus, applying the axial tension to the beam. In order to unload the beam the valve of the lift should be open (see Figure 2.4).

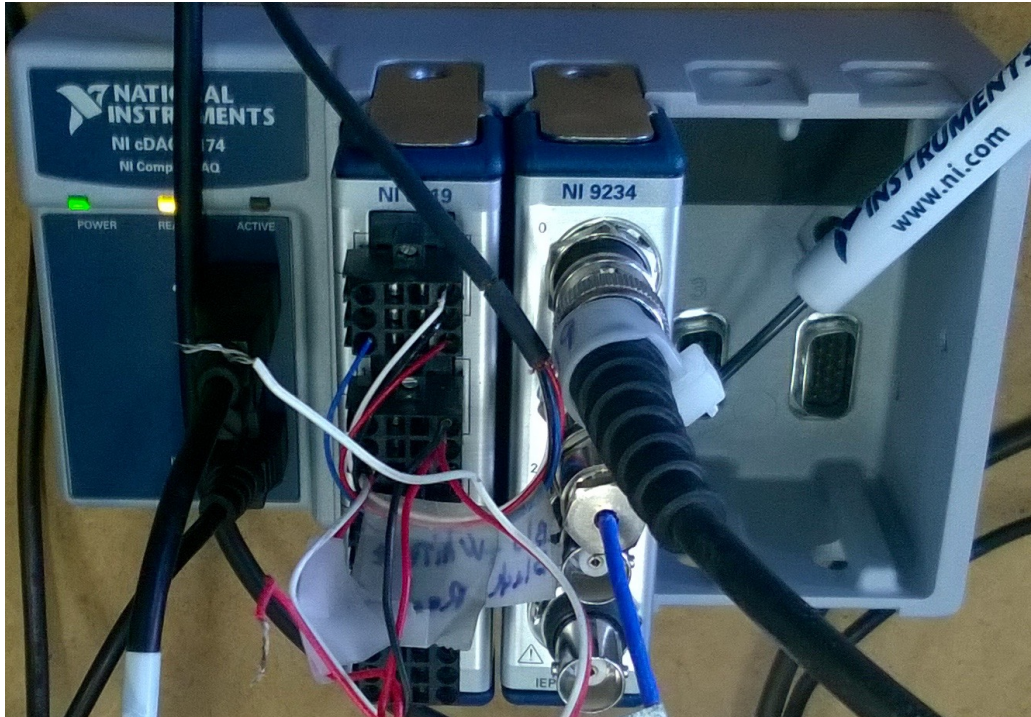


**Figure 2.4. Manual hydraulic lift.**

### **2.2.2.3 Modules for data acquisition**

The intended experiments required simultaneous acquisition of data from an accelerometer, an instrumented hammer, a strain gauge and a load cell. For this purpose we used the equipment of National Instruments and their corresponding software LabView.

The compact data acquisition four-slot USB chassis NI cDAQ-9174 hosted two modules for acquisition: NI 9219 and NI 9234 (see Figure 2.5).



**Figure 2.5.** NI cDAQ-9174 system with NI 9219 and NI 9234 during the tests.

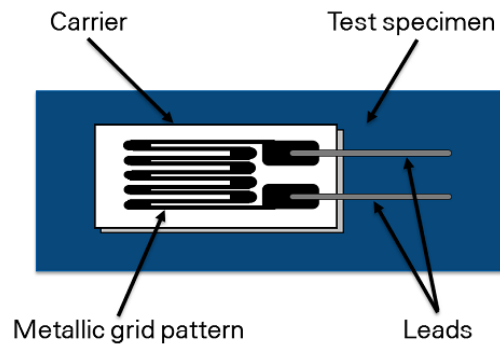
The NI 9219 is a four-channel analogue input module, in which we used two channels: one to connect the load cell and the other for the strain gauge. The other module NI 9234 is also a four-channel dynamic signal acquisition module suitable for high-accuracy frequency measurements from integrated electronic piezoelectric and other sensors. Two channels were used correspondingly to plug in the instrumented hammer and the accelerometer.

#### 2.2.2.4 *Strain gauge*

In our case the beam deformation was caused by the uniaxial tension. This tensile strain  $\varepsilon$  is equal to the ratio between the elongation of the beam  $\Delta L$  and its initial length  $L$ .

$$\varepsilon = \frac{\Delta L}{L} \quad (20)$$

Precision strain gauges are used in mechanical testing to measure deformations. The basic principle is that the electrical resistance of metallic grid changes in proportion to the amount of strain experienced by the test specimen. The metallic strain gauge consists of a very fine wire or, more commonly, metallic foil arranged in a grid pattern (see Figure 2.6 for the schematic). The grid pattern maximizes the amount of metallic wire or foil subject to strain in the parallel direction. The grid is bonded to a thin backing called the carrier, which is attached directly to the test specimen. Therefore, the strain experienced by the test specimen is transferred directly to the strain gauge, which responds with a linear change in electrical resistance.



**Figure 2.6. Schematic of a metallic strain gauge.**

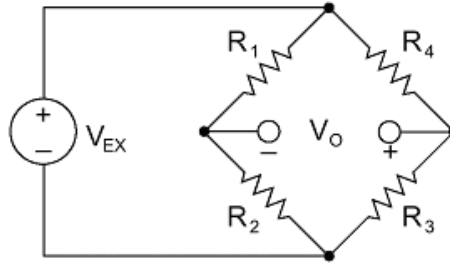
A fundamental parameter of the strain gauge is its sensitivity to strain, expressed quantitatively as the gauge factor  $k$ . Gauge factor is the ratio of the fractional change in electrical resistance  $\Delta R/R$  to the fractional change in length  $\Delta L/L$ , or strain  $\varepsilon$ :

$$k = \frac{\Delta R / R}{\Delta L / L} = \frac{\Delta R / R}{\varepsilon} \quad (21)$$

The actual gauge factor is provided by the sensor documentation and in our case is equal to 2.085 (see Figure 2.9 for the datasheet).

Since measured strains are rarely larger than  $10^{-3}$ , the changes in resistance are very small too and have to be detected very accurately. To measure such small changes in resistance, strain gauge configurations are based on the concept of a Wheatstone bridge.

The general Wheatstone bridge, illustrated in Figure 2.7, is a network of four resistive arms with an excitation voltage,  $V_{EX}$ , that is applied across the bridge.

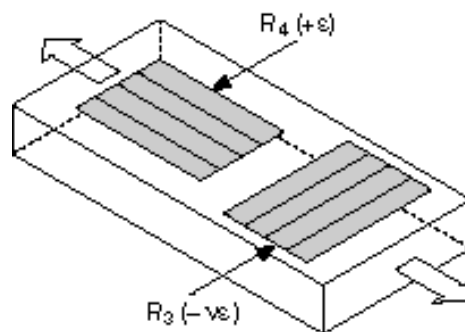


**Figure 2.7. Strain gauges configured in Wheatstone bridge circuits to detect small changes in resistance.**

The Wheatstone bridge is the electrical equivalent of two parallel voltage divider circuits.  $R_1$  and  $R_2$  compose one voltage divider circuit, and  $R_4$  and  $R_3$  compose the second voltage divider circuit. The output of a Wheatstone bridge,  $V_o$ , is measured between the middle nodes of the two voltage dividers.

$$V_o = V_{EX} \left[ \frac{R_3}{R_3 + R_4} - \frac{R_2}{R_1 + R_2} \right] \quad (22)$$

In our tests the sensitivity of the bridge to strain was doubled by putting two active strain gauges in a half-bridge configuration instead of one strain gauge in a quarter-bridge (see Figure 2.8). Generally such configuration allows to measure axial or bending strain.



**Figure 2.8. Half-bridge strain gauges.**

In Figure 2.8  $R_4$  is an active strain gauge measuring the tensile strain ( $+\varepsilon$ ) and  $R_3$  is an active strain gauge compensating for Poisson's effect ( $-\nu\varepsilon$ ).

We attached the strain gauges to the beam in longitudinal and circumferential directions (see Figure 2.9).



Figure 2.9. Strain gauges glued to the beam and their datasheet.

The formed half-bridge configuration was then plugged into the NI 9219 module for data acquisition.

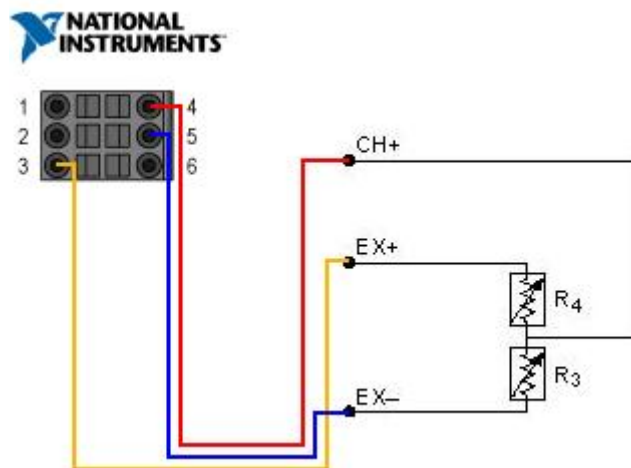


Figure 2.10. Layout of the electrical connection for a strain gauge in a half-bridge configuration.



The strain  $\varepsilon$  measured by the strain gauge could also be used to calculate the axial load applied to the beam using the Hooke's law and the linear dependence between load and tension for the case of uniaxial strain.

$$\sigma = E\varepsilon = \frac{F}{A} \Rightarrow F = E\varepsilon A \quad (23)$$

Where  $E$  is the Young's modulus,  $A$  is the beam cross-section area and  $F$  refers to the axial force.

### **Calibration**

The calibration of a strain gauge is required to determine the dependence between the registration in Volt and the measured tensile strain, this dependence is linear since the linearity of the bridge is assumed. The procedure was carried out via a simple procedure as described below. Zero deformation corresponds to a certain registration of the strain gauge, we called it the registration offset  $V_{offset}$  and it was subject to change from one day of testing to another due to possible environmental temperature variations. Hence, we built the calibration line with respect to the relative change in the reading of the strain gauge in the plane  $\{\varepsilon; \Delta V_0\}$ , where  $\Delta V_0 = V_{reg} - V_{offset}$ . So, the first point of the line was  $(0; 0)$ . Having read the offset, a Shunt resistance  $R_s = 10 \text{ k}\Omega$  was connected in parallel to the  $R_4$ , which, as specified, had a resistance of  $120 \Omega$ . Unbalancing the Wheatstone bridge in this way, we are "fooling" the strain gauge, so that it reads a fictitious "electrical" deformation  $\varepsilon_{el}$ .

$$\varepsilon_{el} = \frac{\Delta R_4}{R_4} / k \quad (24)$$

The variation of the resistance was obtained from the known formula for resistors connected parallelly.

$$\frac{\Delta R_4}{R_4} = \frac{R_4 - R_{eq}}{R_4} = \frac{R_4 - \frac{R_4 R_S}{R_4 + R_S}}{R_4} = \frac{R_4}{R_4 + R_S} \quad (25)$$

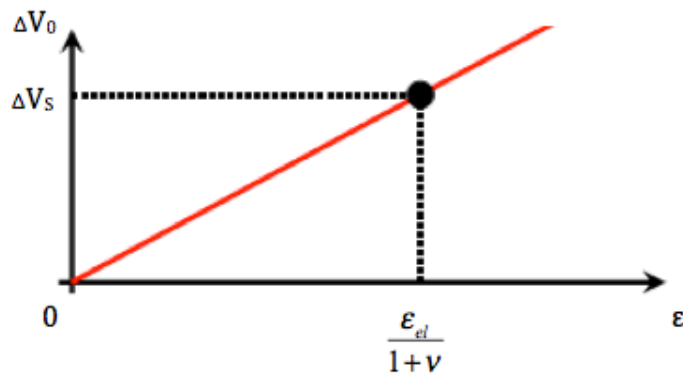
Subtracting the offset from the registered voltage value we obtained the  $\Delta V_S$ .

$$\Delta V_S = \frac{V_{EX}}{4} \frac{\Delta R_4}{R_4} = \frac{V_{EX}}{4} k \varepsilon_{el} \quad (26)$$

However, if the real mechanical deformation were present the resistor  $R_3$  would have also experience the change of resistance equivalent to the strain  $-\nu\varepsilon$ , and the registered voltage loss would have been expressed with a slightly different formula.

$$\Delta V_S = \frac{V_{EX}}{4} \left( \frac{\Delta R_4}{R_4} - \frac{\Delta R_3}{R_3} \right) = \frac{V_{EX}}{4} k \varepsilon_m (1 + \nu) \quad (27)$$

Since the calibration line had to be established with respect to the mechanical deformation, we took into consideration that  $\varepsilon_m = \frac{\varepsilon_{el}}{1 + \nu}$ . Hence, the second point on the line was  $(\varepsilon_m; \Delta V_S)$  as shown in Figure 2.11.

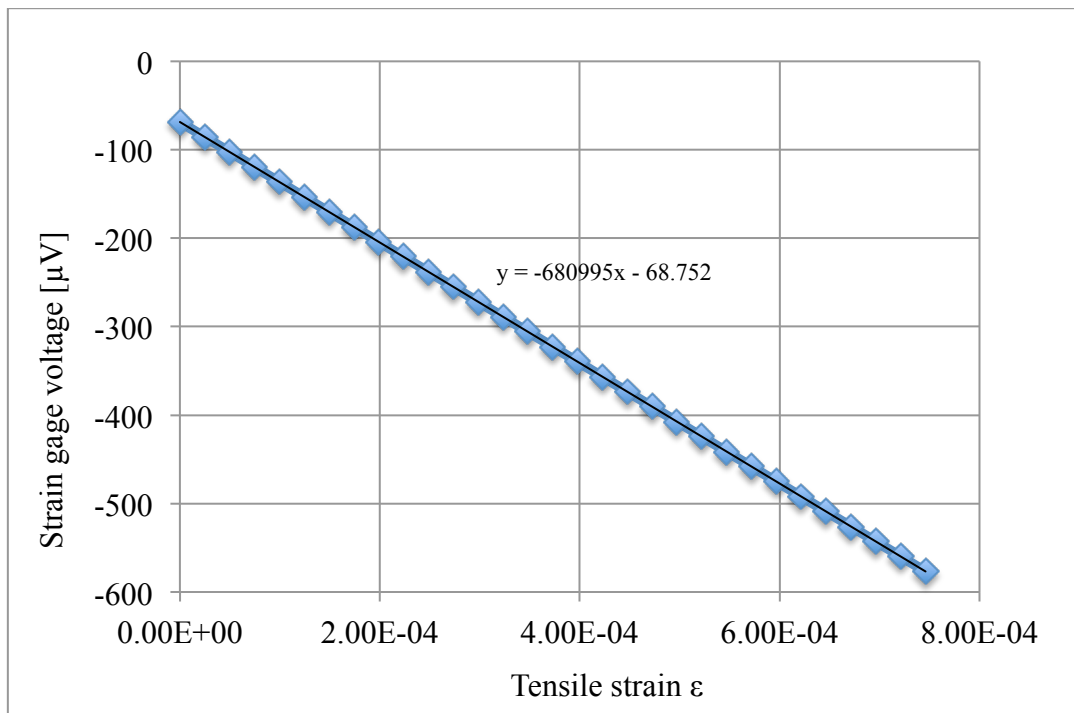


**Figure 2.11. Calibration line for the strain gauge in the half-bridge configuration.**

Calculation of the sensibility of the strain gauge (angular coefficient of the calibration line in Figure 2.11) completed the calibration procedure.

$$S = \frac{\Delta V_S}{\varepsilon_{el}} = \Delta V_S \frac{R_4 + R_S}{R_4} k(1 + \nu) \quad (28)$$

For  $\Delta V_S$  measured in  $\mu V$  we obtained  $S = -680995$ , the coefficient was further used to calculate mechanical strain from the registered voltage loss. The dependence between reading of the strain gauge and the tensile strain for the initial offset  $V_{offset} = -68.752 \mu V$  is illustrated in Figure 2.12.



**Figure 2.12. Dependence between reading of the strain gauge and the actual tensile strain.**

#### 2.2.2.5 Load cell

A load cell is a sensor or a transducer that converts load or force acting on it into an electronic signal. This electronic signal can be a voltage change, current change or frequency change depending on the type of load cell and circuitry used.



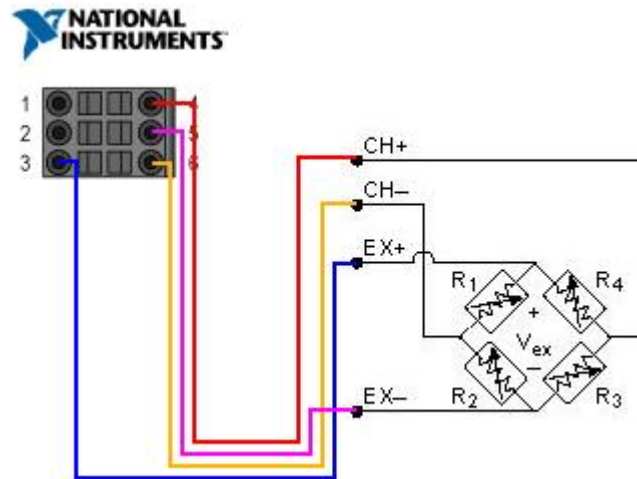
**Figure 2.13. KMR Force washer 200 kN by HBM.**

A KMR force washer with the nominal force of 200 kN produced by HBM was used to measure axial load in the beam. These force washers are designed to measure static and dynamic forces, and are especially suitable for the monitoring of forces, e.g. with production processes or bolted connections. The operating principle is based on the strain gauge technology: when a load is applied to the sensor, it changes its resistance, this change in resistance leads to a change in output voltage when an input voltage is applied. The load cell was placed behind the right support not influencing the free length of the beam, as shown in Figure 2.14.



**Figure 2.14. Load cell mounted on the beam.**

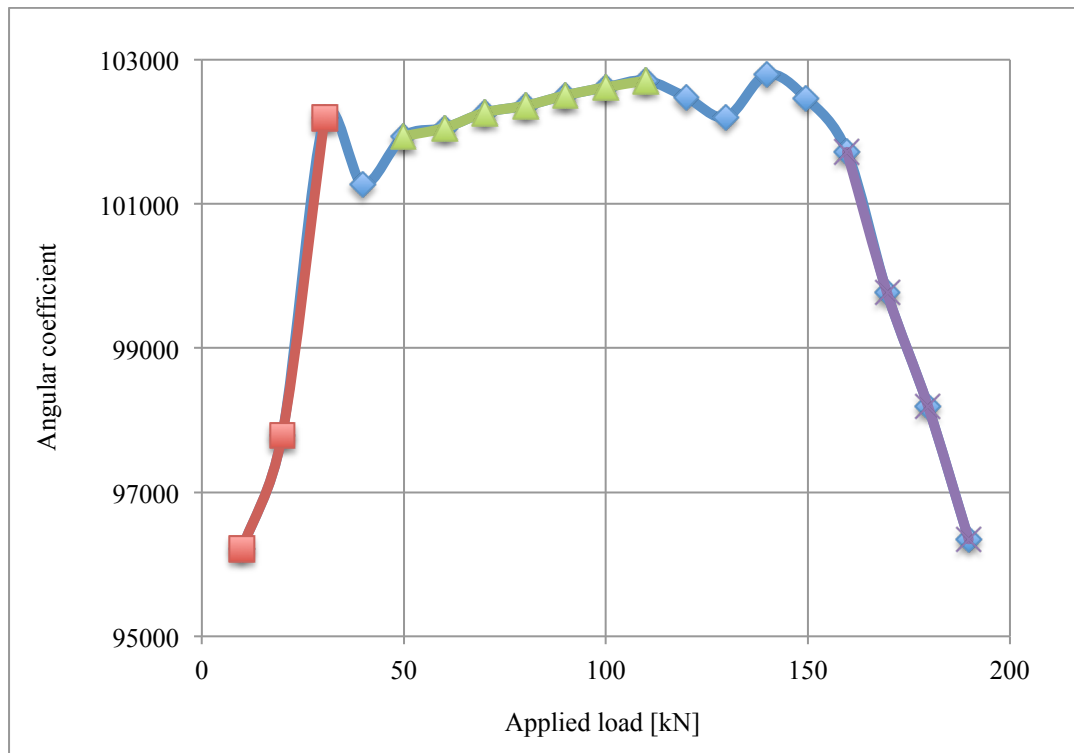
The load-cell in a full-bridge configuration was then plugged into another channel of the NI 9219 module for data acquisition.



**Figure 2.15. Layout of the electrical connection for a load-cell in a full-bridge configuration.**

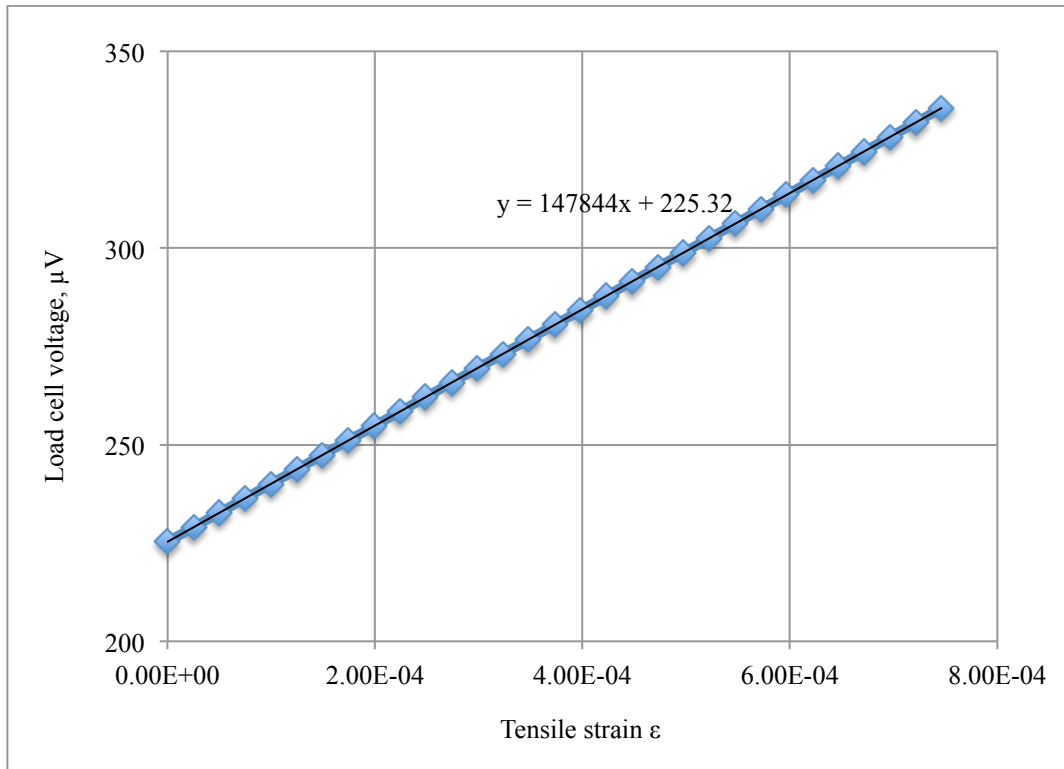
### *Calibration*

The peculiarity of this load cell (which is also valid for the major part of them) is that their precision is high only for the measured values of the order of the nominal force, which for our force washer was 200 kN. The calibration of this load cell had been performed previously by our colleagues at the laboratory of the department of Industrial Engineering in Parma. The result showed that the sensibility of the instrument does not have a constant value and is in a nonlinear dependence from the applied load.



**Figure 2.16. Dependence between load cell sensibility and applied load.**

In Table 2-1 based on the maximum allowable stress and the cross-section area of the beam, we calculated the maximum allowable tensile force of 40 kN, the actual value we managed to reach manually pumping the lift was about 30 kN, which makes only 15% of the nominal force. From the data presented in the previous Figure 2.16, we concluded that on the force range [0; 30] kN the sensibility could not be considered constant. Thus, it has been decided to measure the applied load both via the load cell and compute from the strain gauge measurements. Mutual calibration of the load cell with respect to strain gauge is illustrated in Figure 2.17.



**Figure 2.17. Dependence between load cell reading and actual tensile strain.**

#### **2.2.2.6 Impact hammer**

A PCB instrumented impact hammer features a rugged, force sensor that is integrated into the hammer's striking surface. The force sensor serves to provide a measurement of the amplitude and frequency content of the energy stimulus that is imparted to a test object. By eliminating hammer resonances in the frequency range of interest from corrupting the test data, it is ensured that the structural characteristics of the hammer do not affect measurement results, which provides more accurate and consistent measurements.

Using the multi-channel data acquisition and analysis software, we are able to obtain a variety of mechanical properties to comprehend characteristics of the beam's structural behaviour. Impact hammer testing is applicable for modal analysis, resonance determination and structure health testing.

The PCB instrumented impact hammer demonstrated in Figure 2.18 was used to cause the beam vibrations. The signal of the hammer (input to the system) was recorded via a channel of the NI 9234 module for data acquisition. This signal was controlled for

every excitation to ensure that it was as close as possible to an instant strike, i.e. an impulse. In this way elaboration of data allowed to obtain a clean frequency response function. The details of experimental modal analysis are explained in the following sections.



**Figure 2.18. Instrumented impact hammer.**

### **2.2.2.7 Accelerometer**

To monitor and register the vibration response of a mechanical system three types of sensors are commonly used: displacement sensors, velocity sensors and accelerometers. Data from the sensors is further elaborated via appropriate software and analysed.

Displacement sensors use eddy currents to detect vertical and/or horizontal motion. Velocity sensors use a spring-mounted magnet that moves through a coil, with the outer case of the sensor attached to the part under testing. The coil of wire moves through the magnetic field, generating an electrical signal that is sent back to a receiver and recorded for analysis. Newer models use time-of-flight technology and improved analysis software. Velocity sensors are commonly used in handheld sensors.



Accelerometers use a *piezoelectric crystal* that converts sound waves to electrical impulses and back, attached to a mass that vibrates due to the motion of the part to which the sensor is glued. As the mass and the piezoelectric crystal vibrate, a low voltage current is generated. It is passed through a pre-amplifier and sent to the recording device. Accelerometers are very effective for detecting even the high frequency vibrations. In this study the accelerometers are used as vibration sensors.

A PCB accelerometer was used in conjunction with the hammer to provide a measurement of the beam's structural response due to the hammer impulse.



**Figure 2.19. Accelerometer used for dynamic response acquisition.**

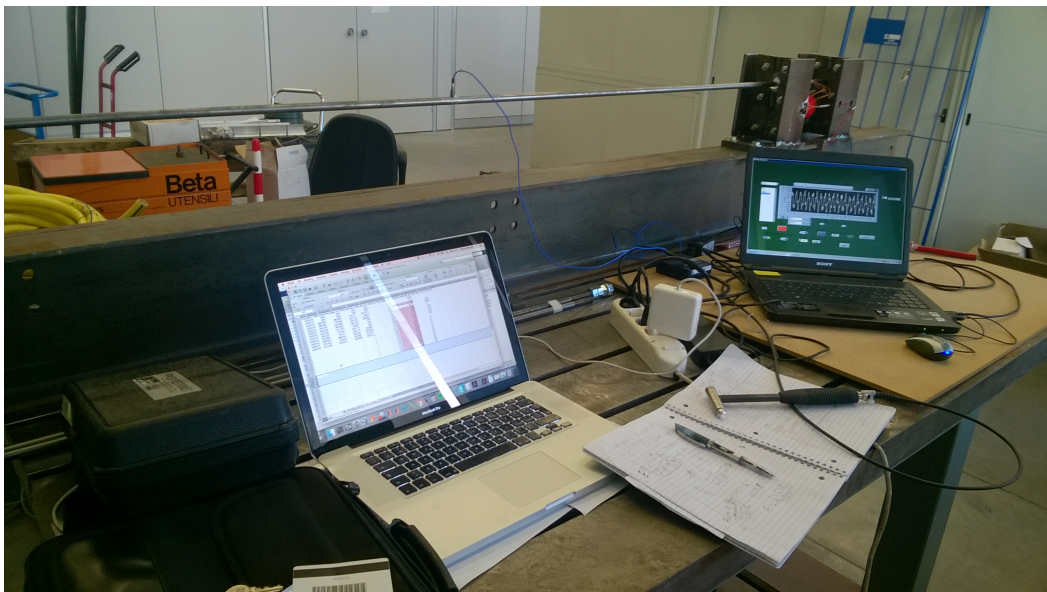
Figure 2.19 shows the PCB accelerometer used for testing: the sensor fixed on the beam, the case with the model specification and the data-sheet that states the sensitivity of  $9.98 \text{ mV}/(\text{m/s}^2)$ . NI 9234 module for data acquisition hosted the sensor.

## 2.3 Experimental modal analysis

Modal analysis is a way to describe a structure in terms of its natural characteristics, which are the frequency, damping and mode shapes. These modal characteristics are unique for each structure and are determined by its material properties, i.e. mass, stiffness, damping, and boundary conditions. Modal analysis is an important tool that nowadays assists in the design of almost any structure, since it helps to spot the possible weaknesses of the structure and identify elements that should be improved.

### 2.3.1 Data acquisition

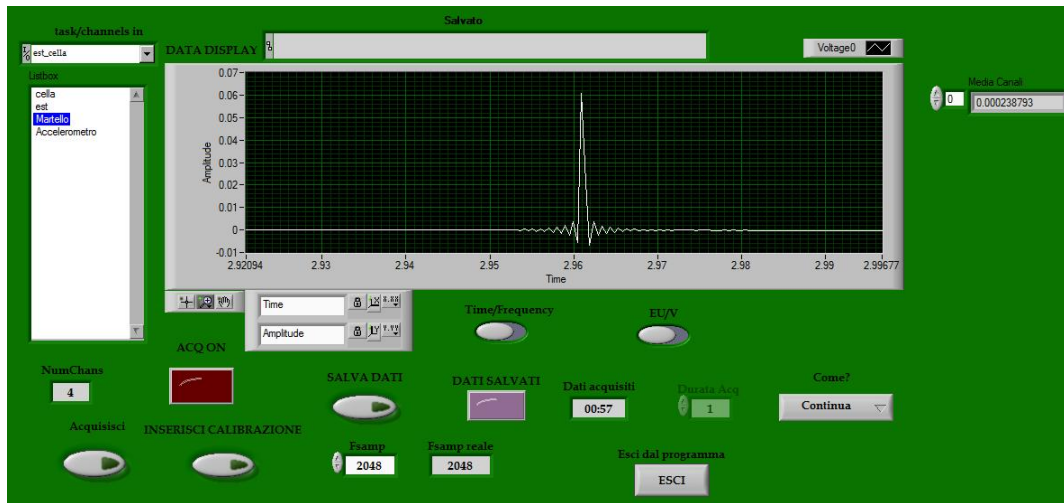
The objective of the experiment was to measure dynamical response of the system to an impulse excitation. Vibrations were excited by an instrumented impact hammer and registered with an accelerometer. The tests were carried out for two beams: “healthy” and “damaged” varying the tensile load from 0 to 30 kN. Figure 2.20 pictures the testing process in progress.



**Figure 2.20. Experimental setup and the laboratory workspace.**

The hardware of the experimental setup described in Section 2.2 was powered by the National Instrument software for data acquisition *LabView*. LabView allows to construct your own program for data acquisition for the specific configuration and

scope of the experiment (see Figure 2.21 for the screenshot of our program during measurements). In our case there were four channels for signal registration: strain gauge, load cell, impact hammer and accelerometer. Before starting the measurements, the functioning of modules and settings of channels were changed controlled inside the appropriate program.



**Figure 2.21. Screenshot of the program for data acquisition developed in LabView.**

The developed LabView program for the experiment enabled the following actions:

- 1) Choose the type of signal registration: continuous or instantaneous;
- 2) Setup the sampling rate for signals (the allowed minimum was 2048 samples per second);
- 3) Insert calibration for channels;
- 4) Start acquisition;
- 5) Choose time or frequency domain visualization in the graphical window;
- 6) Track each of the channel signals in the graphical window;
- 7) Control the time of registration;
- 8) Finish acquisition;
- 9) Calculate the mean value of each channel after the acquisition is finished;
- 10) Save the registered signals in a .mat file (ready to use in Matlab for further elaboration).

First, the value of load was controlled and registered and then the acquisition of vibrations was performed 5 times for measurements at each load. It was important to control the input signal to make sure that it was a single stroke close to the Dirac delta. It was easily done thanks to the instant graphical representation of registered signals directly in the program window (see Figure 2.21). Once the data was recorded it was elaborated in terms of FRF to obtain the natural frequencies and modal parameters of the beams.

### 2.3.2 Data elaboration: FRF and coherence

Fundamentally a *frequency response function (FRF)* is a mathematical representation of the relationship between the input to the system and the output of a system. The response of the system in the time domain  $y(t)$  (output) to an instrumented impact hammer excitation  $x(t)$  (input) is represented by the vibrations registered via accelerometers. The first step of data elaboration is an appropriate trimming of registered signals. Since our input is close to the Dirac delta (impulse), the response of our interest starts with the moment of the impulse impact and lasts until all the motion caused by this impact is damped. After performing some pre-tests, we concluded that the response lasts from 5 to 20 seconds depending on the axial load and the beam. The trimming is done automatically in the software for experimental data processing coded Matlab.

FRFs are most commonly used for single input and single output analysis, normally for the calculation of the  $H_1(f)$  or  $H_2(f)$  functions. The  $H_1(f)$  frequency response function is used in situations where the output to the system is expected to be noisy compared to the input. The  $H_2(f)$ , on the contrary, is used when the input to the system is expected to be noisy compared to the output.  $H_1(f)$  or  $H_2(f)$  can be used for resonance analysis or hammer impact analysis, while  $H_2(f)$  is mostly used for random excitation. In our data elaboration procedures the FRF  $H_1(f)$  is computed according to Equation (29).

$$\begin{aligned}
 H_1(f) &= \frac{S_{xy}(f)}{S_{xx}(f)} \\
 H_2(f) &= \frac{S_{yy}(f)}{S_{yx}(f)}
 \end{aligned}
 \tag{29}$$

Where  $S_{xy}(f)$  is the cross power spectrum of the input and output,  $S_{xx}(f)$  is the auto spectrum of the input,  $S_{yy}(f)$  is the auto spectrum of the output,  $S_{yx}(f)$  is the cross power spectrum of the output and input in the frequency domain. These spectra are averaged for a set of  $N$  input-output signals and are computed as follows.

$$\begin{aligned}
 S_{xx}(f) &= \frac{1}{N} \sum_{n=1}^N X_n(f) \overline{X_n(f)} \\
 S_{xy}(f) &= \frac{1}{N} \sum_{n=1}^N Y_n(f) \overline{X_n(f)} \\
 S_{yy}(f) &= \frac{1}{N} \sum_{n=1}^N Y_n(f) \overline{Y_n(f)} \\
 S_{yx}(f) &= \frac{1}{N} \sum_{n=1}^N X_n(f) \overline{Y_n(f)}
 \end{aligned} \tag{30}$$

Where  $X_n(f)$  and  $Y_n(f)$  are correspondingly the single input and output signals in the frequency domain, computed as Fast Fourier Transforms of the input  $x_n(t)$  and output  $y_n(t)$  signals in the time domain; the bar corresponds to the operation of complex conjugate.

Since a noise is always present in measurements of the input-output behaviour of a system, it is important to evaluate to what extent the measured output is caused by the registered input. This operation is characterized by another spectrum called the *coherence function*. The coherence is also defined in terms of the cross spectra and the auto spectra as of Equation (31).

$$\gamma^2(f) = \frac{S_{xy}(f)S_{yx}(f)}{S_{xx}(f)S_{yy}(f)} = \frac{H_1(f)}{H_2(f)} \tag{31}$$

Coherence is a dimensionless spectrum with magnitude between 0 and 1 at any frequency. It quantifies the fraction of measured output power caused by the measured input power and a linear process. For a single pair of input-output the coherence would result 1, thus, this spectra only makes sense for ensemble averaged cross and auto spectra. Basically coherence characterizes a route of energy through the loop of the

process: in a perfectly linear system not contaminated with noise the energy that is put in comes back fully and the coherence is 1. If the system is non-linear or if external noise was introduced to the input or output, the energy loop will be less efficient and the coherence will be less than one. Subsequently, a coherence of zero means that the output and input are totally unrelated. Values different from 0 and 1 may indicate noise in input-output and/or nonlinearity of the process.

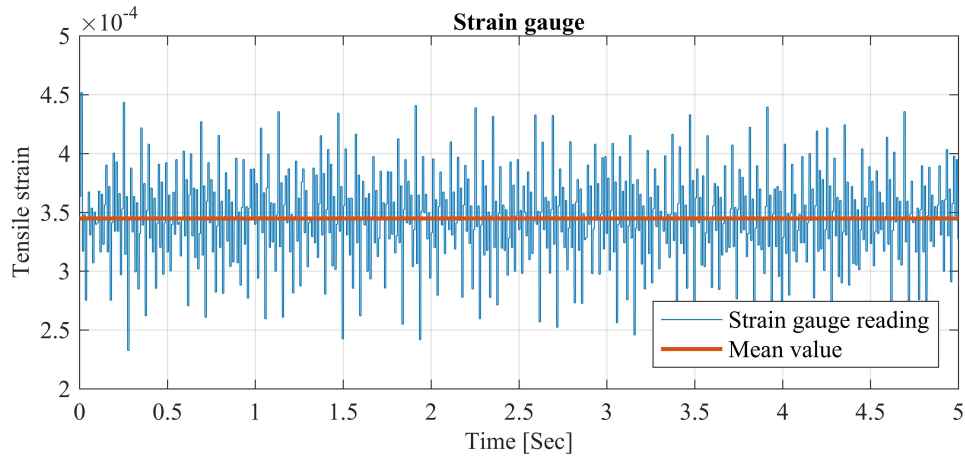
FRF and coherence are used together for correct and complete analysis of the system response. As the number of averaged spectra increases, FRF and coherence become more definitive. In our research we averaged the spectra of five samples of input-output  $N=5$ , which resulted in good quality measures.

The computation of FRFs and coherence function was done via scripts and functions developed in Matlab. Signals saved in the .mat file from the data acquisition program were passed on to the scripts to perform the following operations:

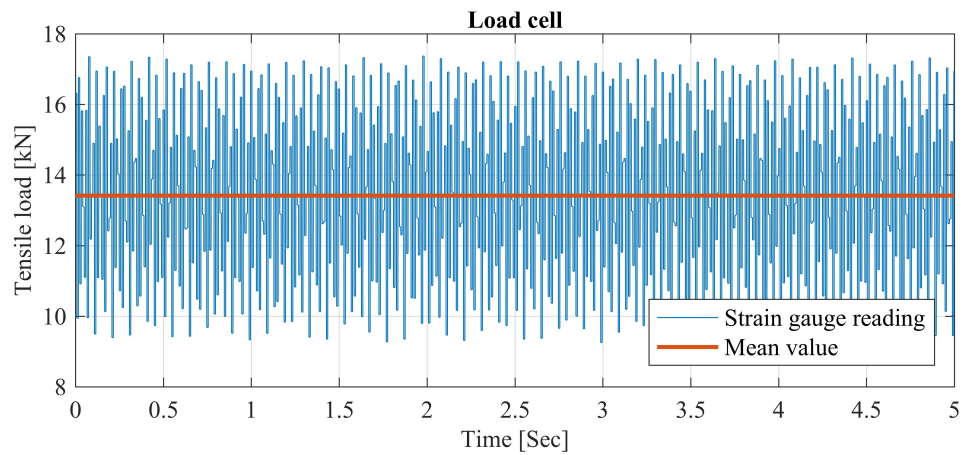
- 1) Trimming of recorded signals: window from the moment when the impulse was given to the system and until the motion was over;
- 2) Applying calibration to the registered signals;
- 3) Computing frequency domain representation of the signals;
- 4) Computing averaged input/output/cross and power spectra;
- 5) Computing frequency response and coherence functions;
- 6) Visualizing FRFs, coherence functions, recorded inputs, outputs and their spectra;
- 7) Saving the results in array forms in .mat files.

### 2.3.3 Experimental results

Both strain gauge and load cell demonstrated quite noisy signals with many oscillations as pictured in Figure 2.22 and 2.23. To obtain the values of tensile load and strain, the mean of each signal was computed and then converted to appropriate unit using the calibration.

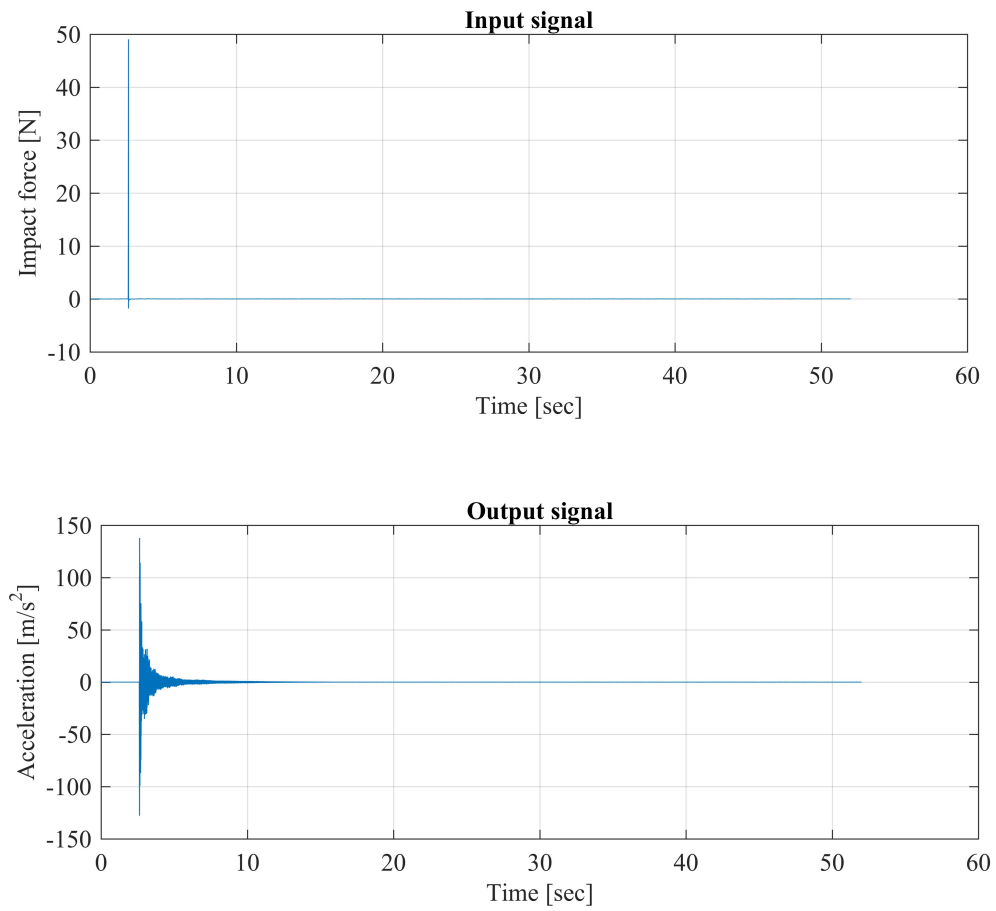


**Figure 2.22.** Example of a signal recorded from the strain gauge.



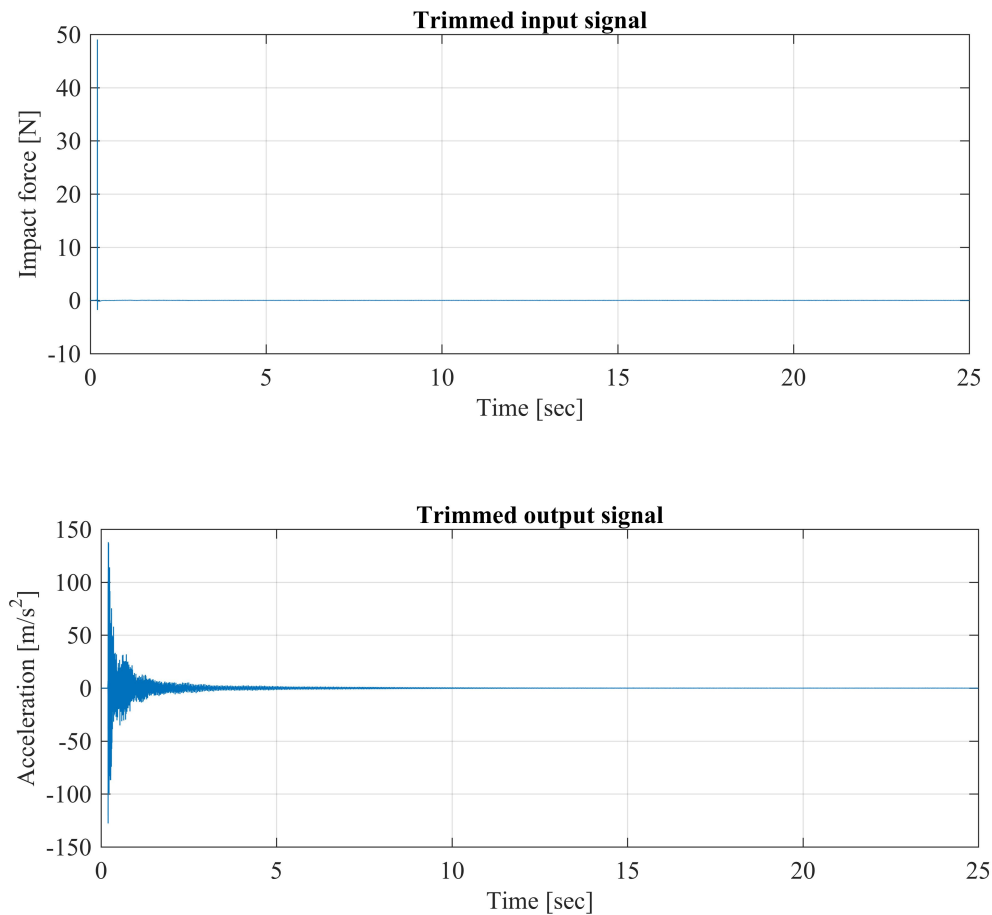
**Figure 2.23.** Example of a signal recorded from the load cell.

Afterwards, the signals recorded from the impact hammer and accelerometer were analysed. In Figure 2.24 one can see the untrimmed raw signals. The moment of impulse excitation is clearly observed and the windowing of the signals is done for time of 0.2 sec before the impulse and until the excited motion dies down. Figure 2.25 pictures the trimmed input and output signals, final duration was about 25 seconds or, correspondingly, 51200 samples.



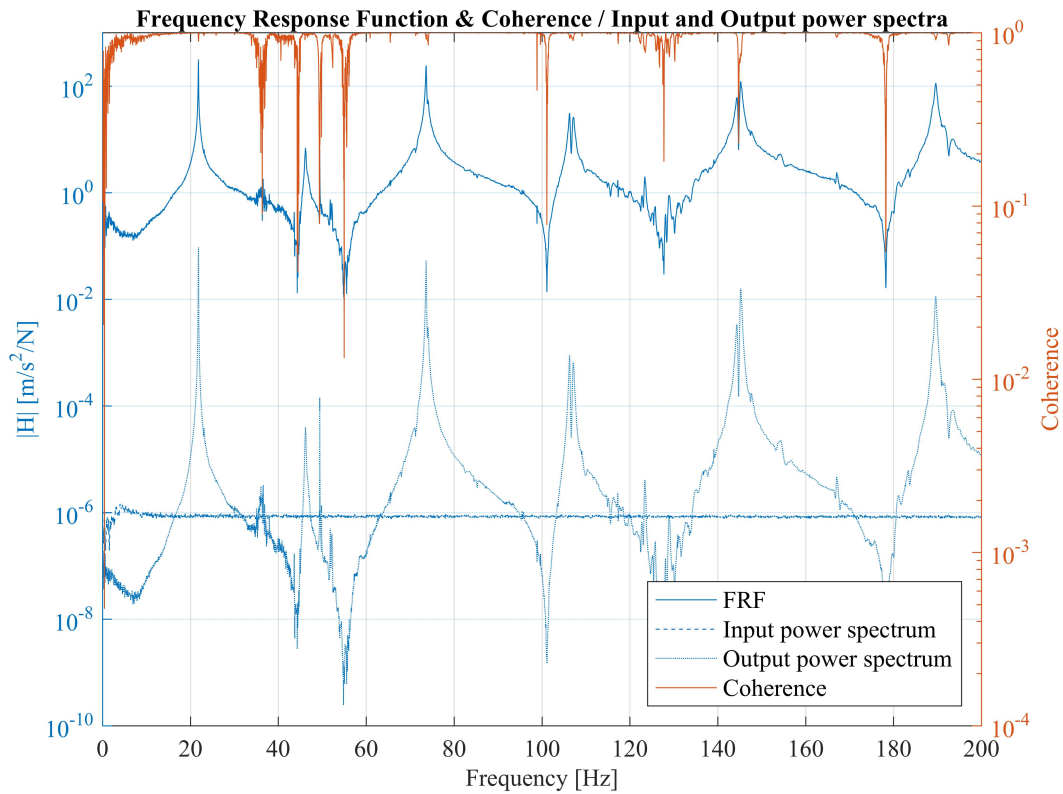
**Figure 2.24. Example of input and output signals: impulse excitation and response.**





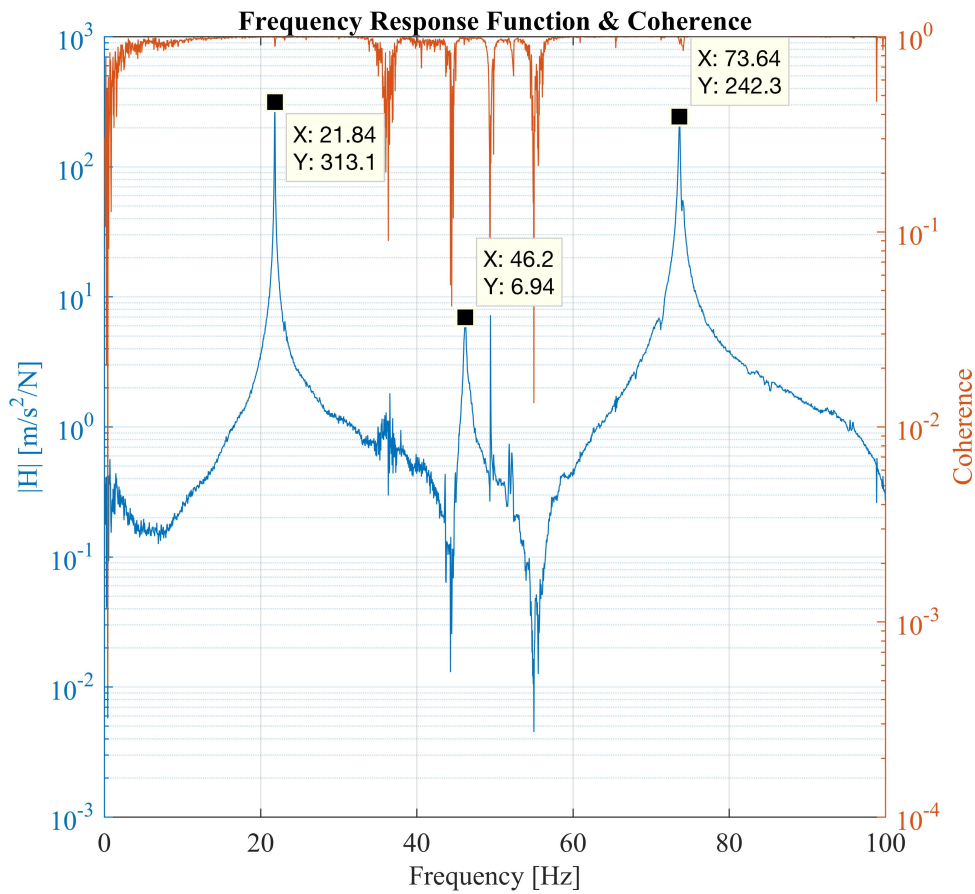
**Figure 2.25. Windowing of input and output signals.**

The trimmed input/output signals (5 pairs for each tensile load) were further elaborated in Matlab, obtaining their representation in the frequency domain, computing auto and cross power spectra and, finally, frequency response and coherence functions. Figure 2.26 gives a peek on the corresponding results for a beam under 13.49 kN tensile load. From this example it is evident that the impact was sufficient to excite all the first modes of beam vibrations (input power spectrum is almost a horizontal line). The quality of all the acquisitions was controlled analysing the FRF and coherence.



**Figure 2.26. FRF, coherence and input/output power spectra.**

A set of natural frequencies was obtained by picking the peaks of the frequency response function diagram. For each value of the tensile load we picked first 6 natural frequencies in the range of 0 – 250 Hz, which is sufficient to characterize a mechanic system of this kind. Figure 2.27 illustrates the picked first three natural frequencies of the healthy beam under axial load of 13.49 kN.



**Figure 2.27. FRF and coherence function with picked peak frequencies.**

Another important parameter of modal analysis is the damping ratio. It indicates how vibrations of each eigenmode are damped in the system. A couple of approaches for computing damping ratios exist, in this study we adopted the following concept:

$$\zeta_r = \frac{\Delta\omega}{2\omega_r} \quad (32)$$

Where  $\omega_r$  is the resonant frequency and  $\Delta\omega$  is the frequency bandwidth around that frequency. The amplitude of FRF at the final points of the bandwidth is equal to the resonant amplitude divided by the square root of two  $A_r/\sqrt{2}$ . Calculated in decibel this results in  $-3$  dB compared to the resonant amplitude. Natural frequencies and damping

ratios of the first three modes of the healthy beam under axial load of  $13.49 \text{ kN}$  (the FRF shown in Figure 2.27) are given in Table 2-2.

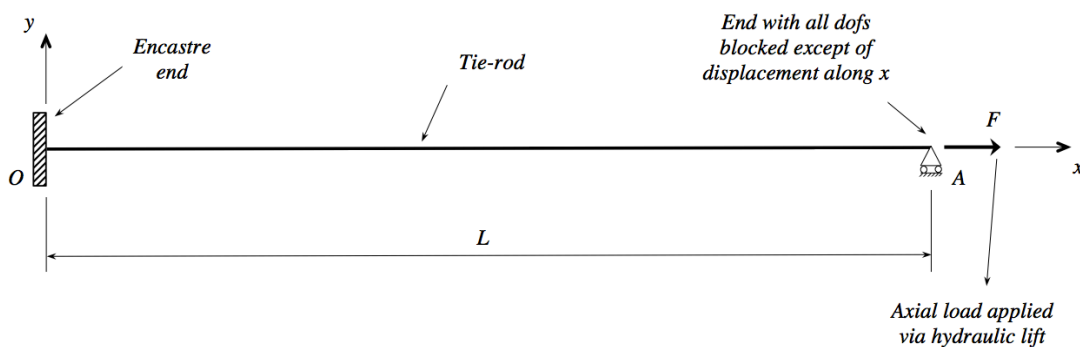
**Table 2-2. Natural frequencies and damping ratios of the first three modes of the healthy beam under axial load of 13.49 kN.**

Mode number	Natural frequency	Damping ratio
I	21.84	0.0017
II	46.20	0.0026
III	73.64	0.0011

The procedure of FRF and coherence quality analysis and natural frequency extraction was carried out for every measurement at each tensile load and for both beams.

### 2.3.4 Influence of the axial load on beam vibrations

In this Section theoretical background for the effect of tension on beam vibrations is presented. The scheme of a beam in our experimental setup (described in Section 2.2) is sketched in Figure 2.28. One end of the beam was fixed and another could move along the horizontal axis, enabling the axial loading. Once the load was applied it was kept constant during the vibration acquisitions, thus, that end in terms of boundary conditions was considered encasté as well.



**Figure 2.28. Scheme of a beam in the experimental setup.**

Section 1.2.1 showed how the equation of free vibrations of a beam (7) is derived from the Lagrange principle. Considering the scheme in Figure 2.28, this equation can be rewritten for a general case of forced vibration (33).

$$EI \frac{\partial^4 w}{\partial x^4} + \rho A \frac{\partial^2 w}{\partial t^2} - F \frac{\partial^2 w}{\partial x^2} = P(x, t) \quad (33)$$

Where  $P(x, t)$  is an external force. If this force is equal to zero, we are dealing with free vibrations or modal vibrations (34).

$$\frac{\partial^4 w}{\partial x^4} - \frac{F}{\rho A c^2} \frac{\partial^2 w}{\partial x^2} + \frac{1}{c^2} \frac{\partial^2 w}{\partial t^2} = 0 \quad (34)$$

Proceeding with solving differential equation (34) according to the approach described in Section 1.2.1, we used the general solution (13) for the form function. Thus, roots of the first equation in (14) were obtained as follows:

$$s^2 = \frac{1}{2} \frac{1}{\rho A c^2} \left( F \pm \sqrt{F^2 + 4\omega^2 c^2 \rho^2 A^2} \right) \quad (35)$$

From equation (35) we deduced two real and two complex roots  $s_{1,2} = \pm k_1$ ,  $s_{3,4} = \pm ik_2$ .

$$\begin{aligned} k_1 &= \sqrt{\frac{1}{2} \frac{1}{\rho A c^2} \left( F + \sqrt{F^2 + 4\omega^2 c^2 \rho^2 A^2} \right)} \\ k_2 &= \sqrt{\frac{1}{2} \frac{1}{\rho A c^2} \left( -F + \sqrt{F^2 + 4\omega^2 c^2 \rho^2 A^2} \right)} \end{aligned} \quad (36)$$

The form function (15) can be expressed in terms of trigonometric functions  $\sin$ ,  $\cos$  and hyperbolic functions  $\sinh$ ,  $\cosh$ , S. Rao [94] to avoid solving equations in complex numbers where possible.

$$W(x) = C_1 \cos k_1 x + C_2 \sin k_1 x + C_3 \cosh k_2 x + C_4 \sinh k_2 x \quad (37)$$

The boundary conditions for the beam clamped at both ends require the deflection and the angle of rotation to be equal to zero (38).

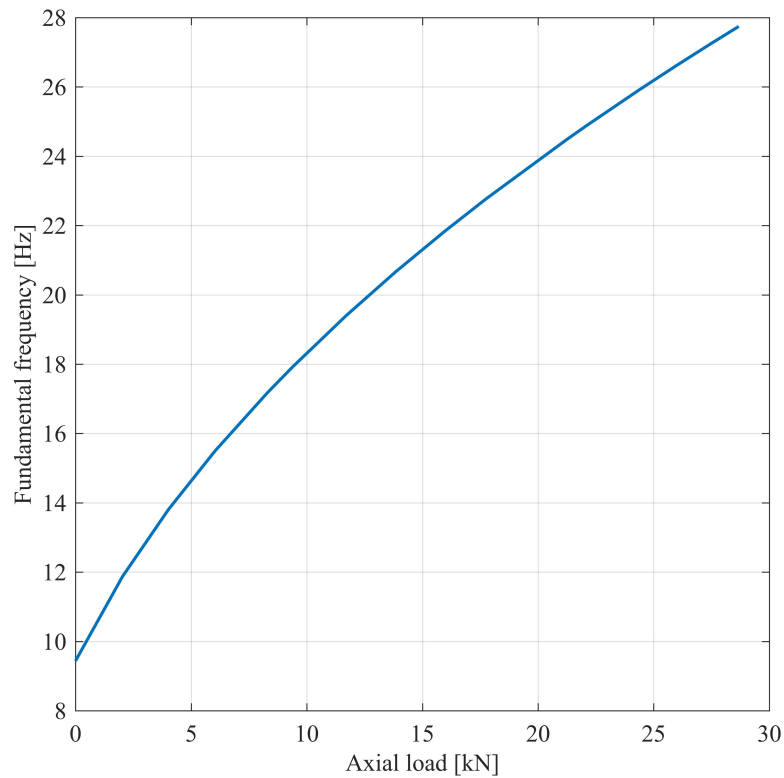
$$x = 0, L : \begin{cases} w = 0 \\ \frac{\partial w}{\partial x} = 0 \end{cases} \quad (38)$$

After substitution of the form function  $W(x)$  (37) into the boundary conditions (38) a homogeneous system of four algebraic equations containing the unknown constants  $C_1 \dots C_4$ , is obtained. In a matrix form it is expressed identically to (16). Furthermore, the characteristic equation was derived since the determinant of the matrix  $M$  in (16) is set to zero (39).

$$\det \begin{bmatrix} 1 & 0 & 1 & 0 \\ 0 & k_1 & 0 & k_2 \\ \cos k_1 L & \sin k_1 L & \cosh k_2 L & \sinh k_2 L \\ -k_1 \sin k_1 L & k_1 \cos k_1 L & k_2 \sinh k_2 L & k_2 \cosh k_2 L \end{bmatrix} = 0 \quad (39)$$

Equations (36) for the coefficients  $k_1$  and  $k_2$  were substituted into (39) and, thus, the frequency equation was derived. The natural frequencies of the system  $\omega$  were computed from the latter equation with assistance of appropriate software, e.g. symbolic mathematical software *Maple*, used in this thesis, which allows to obtain both numerical or symbolic solution, otherwise *Mathematica* or *Matlab*.

As shown hereby,  $\omega$  depends on the mass and stiffness  $(\rho, A, E, I, L)$  characteristics of the system, as well as on the axial pretension applied to the beam. Basically, Equation (39) provides an implicit function of two variables –  $\omega$  and  $F$ . Analytical investigation of this function illustrated in Figure 2.29 has proven that axial load increases the natural frequencies and, thus, stiffens the beam.

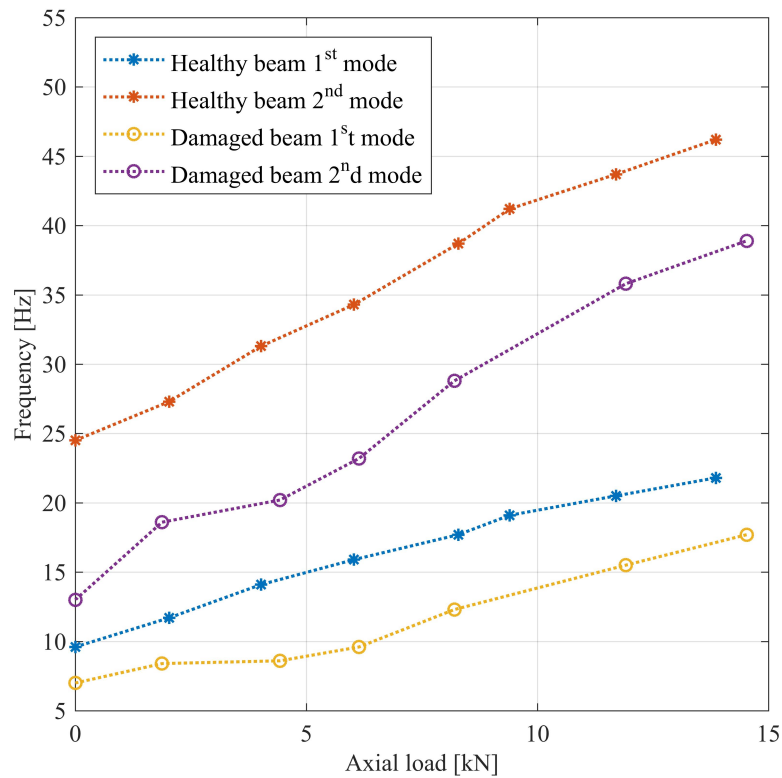


**Figure 2.29. Fundamental frequency of a beam in tension.**

### 2.3.5 Influence of the damage on beam vibrations

After completing the sets of tests for healthy and damaged beams, the results were confronted between each other. It should be noted that since the axial load was regulated manually, it was possible to maintain a loading step of about 1-2 kN, however, the exact same values of loading values for each test were not achievable. That is why in the comparison of the results we see some deviation, e.g. the healthy beam under 11.7 kN and the damaged beam under 11.9 kN.

The main conclusion drawn from the testing of the two types of beams was that *the natural frequencies of the “damaged” beam were consistently lower than for the “healthy” (continuous) one*, under the same loading condition. This fact is illustrated in Figure 2.30.



**Figure 2.30. First and second natural frequencies of the healthy and damaged beams with respect to axial load.**

The beam with the simulated “damage” was tested separately for 4 different torque values applied with a torque wrench at the joint between the two parts of the beam. The torques were following: 10, 15, 20 and 25 Nm. Figure 2.30 illustrated the first two eigenfrequencies of a damaged beam with 25 Nm nominal torque at the joint. More experimental results for the first six natural modes with respect to axial load, damage and torques are presented in Table 2-3.

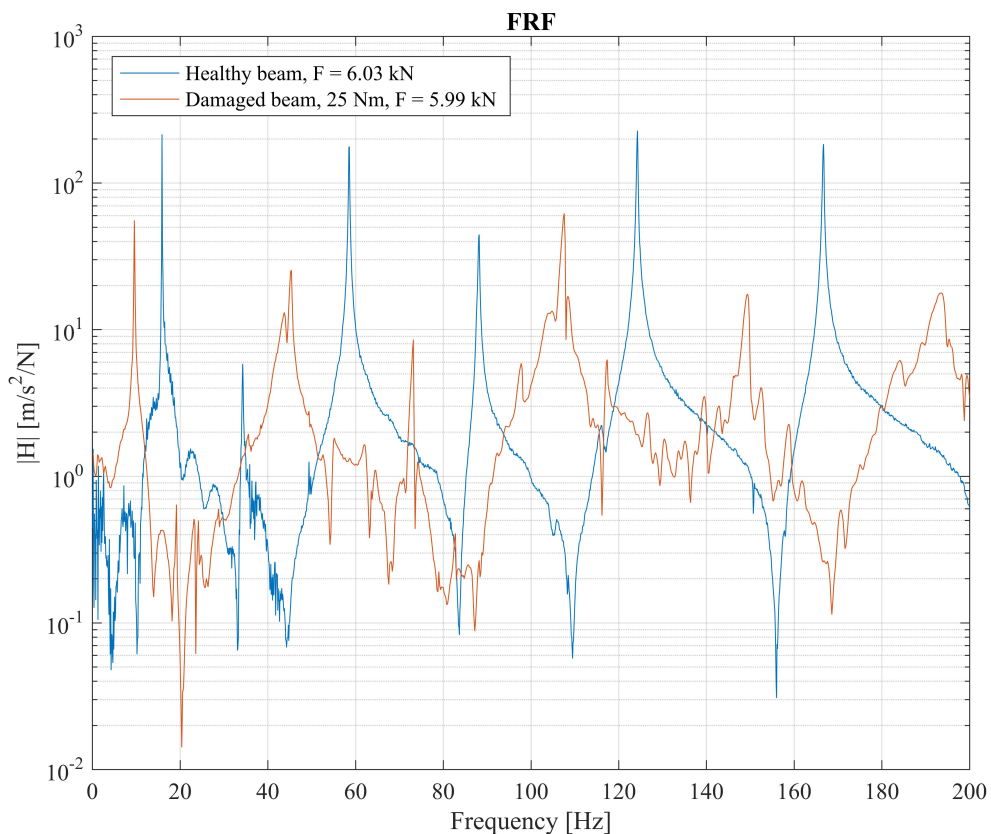


**Table 2-3. Natural frequencies of the tested beams under tensile loading.**

Axial load $F$ , kN	$\omega_1$	$\omega_2$	$\omega_3$	$\omega_4$	$\omega_5$	$\omega_6$
Healthy beam						
0.00	9.60	24.50	45.45	73.75	106.20	152.40
2.03	11.70	27.30	49.00	77.20	112.40	154.10
4.02	14.10	31.30	54.30	83.10	118.50	160.90
6.03	15.90	34.30	58.60	88.20	124.30	166.70
8.29	17.70	38.70	62.80	93.30	130.00	172.70
9.40	19.10	41.20	66.40	97.60	134.70	178.70
11.70	20.50	43.70	70.20	102.20	140.10	184.20
13.49	21.80	46.20	73.60	106.30	145.20	189.60
15.97	22.80	48.00	76.50	110.70	149.90	195.20
17.75	24.20	50.60	80.10	115.20	155.00	200.00
21.23	25.80	53.10	85.00	121.20	162.60	209.60
22.10	25.80	53.10	85.10	121.30	162.70	209.70
24.38	27.00	57.30	88.50	125.80	167.90	214.80
25.92	27.60	58.50	90.80	127.90	170.40	218.80
27.46	28.60	60.87	94.33	132.30	175.80	224.50
28.67	28.60	60.80	94.10	132.00	175.20	223.90
Beam with the "damage" Torque 10 Nm						
3.32	7.60	15.10	36.80	62.30	96.00	137.90
4.29	7.80	16.50	37.70	59.40	97.00	139.10
5.91	8.90	22.40	41.50	68.90	101.80	143.80
8.64	11.30	29.60	47.40	75.40	110.60	151.80
10.68	13.80	31.60	53.70	82.90	119.50	162.20
11.66	14.80	32.80	56.00	86.10	122.70	166.10
14.43	17.40	38.90	63.30	115.60	133.00	177.70
Beam with the "damage" Torque 15 Nm						
1.72	8.50	18.50	38.00	66.00	97.00	141.00
3.94	8.80	23.30	41.10	82.20	101.90	143.80
5.93	10.70	25.70	47.60	76.30	111.80	155.00
8.52	13.40	30.60	53.80	83.90	120.70	164.50
10.72	15.60	34.10	58.80	89.50	126.80	171.00
12.02	16.60	37.30	61.30	92.50	130.00	174.40
14.50	18.60	40.40	66.20	98.20	136.60	181.80
Beam with the "damage" Torque 20 Nm						
1.93	8.33	16.00	38.00	65.67	97.33	136.30
3.87	8.50	16.80	38.70	64.50	98.20	138.60
7.00	9.80	25.00	45.80	74.00	108.80	151.40
8.47	11.00	27.10	48.20	77.90	112.60	156.90
10.68	13.60	30.90	54.40	84.80	122.20	166.40
12.07	14.70	32.80	57.20	87.80	125.40	169.80
14.96	16.90	37.70	62.40	94.00	132.00	177.40

Beam with the “damage” Torque 25 Nm						
1.88	8.40	18.60	37.40	64.80	97.40	136.40
4.43	8.60	20.20	39.60	66.80	99.80	140.50
5.99	9.50	19.20	43.40	73.20	107.60	147.60
6.14	9.60	23.20	43.80	71.40	106.50	149.30
8.20	12.30	28.80	51.80	81.60	118.80	161.80
11.07	14.90	34.70	57.80	88.70	126.50	171.10
11.91	15.50	35.80	59.10	90.10	128.10	172.80
14.53	17.70	38.90	64.20	96.20	134.70	180.60

Generally the FRFs of the “healthy” beam appeared less contaminated, the resonant peaks were more accented (see Figure 2.31 for an example). In particular this was even more evident for the level of axial loading under 10 kN. Overall for lower load (<10 kN) the response of the “damaged” beam to the impact of same intensity lasted much less: about 2 seconds compared to almost 10 seconds for the “healthy” beam. Both of these facts are related to damping.



**Figure 2.31. FRFs of healthy and damaged beams under tensile load of 6.03 kN and 5.99 kN.**

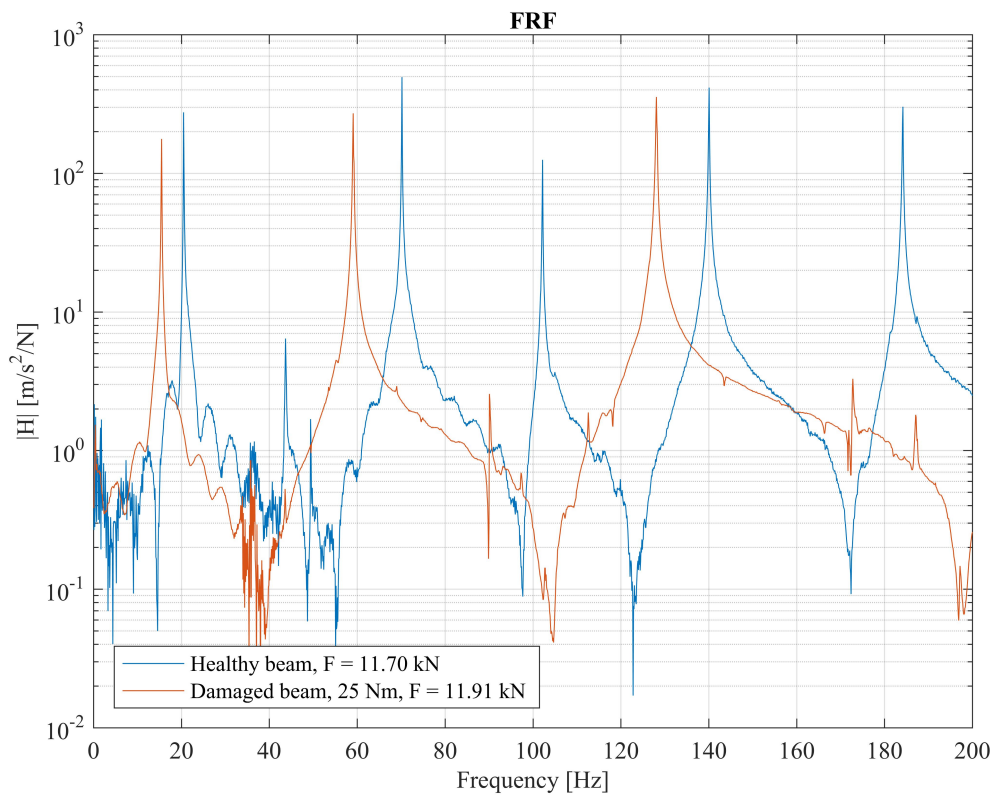
Higher damping ratios of the “damaged” beam mean that it is in general more damped as a system. This makes sense if we take a look at the Rayleigh damping matrix  $C$  (40), which is proportional to the mass and stiffness matrices  $M$  and  $K$  [109].

$$C = \alpha M + \beta K \quad (40)$$

Modal damping ratios and natural frequencies are related to the coefficients  $\alpha$  and  $\beta$  by Equation (41). Thus, increased  $\zeta$  means that  $\alpha$  and  $\beta$ , and, subsequently, the overall damping are higher.

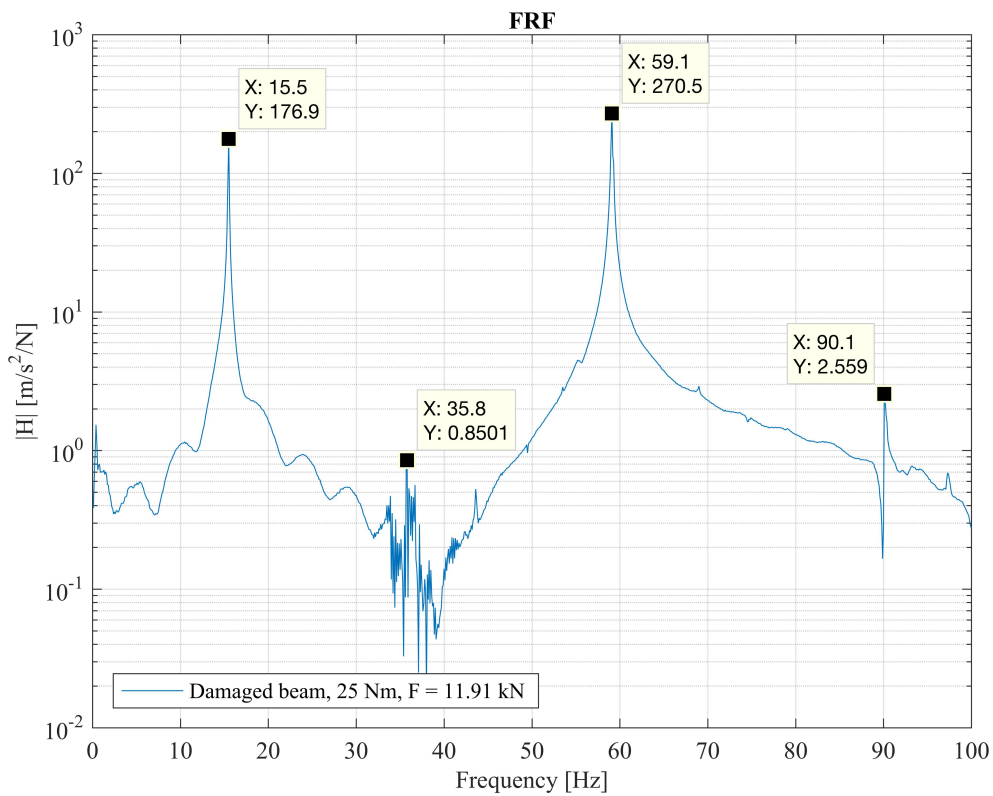
$$\zeta_r = \alpha \frac{1}{2\omega_r} + \beta \frac{\omega_r}{2} \quad (41)$$

Damage introduces a way of energy dissipation in the structure, which is reflected in augmentation of the system damping. Hence, we concluded that one of *the main damage markers is the increased modal damping*. This observation, however, became less evident with increase of the axial load (see Figure 2.32), since the tension stiffens the beam and makes the system less damped. Still, the trend of smaller amplitudes of resonant peaks for the damaged beam compared to the FRF of the healthy one persisted.



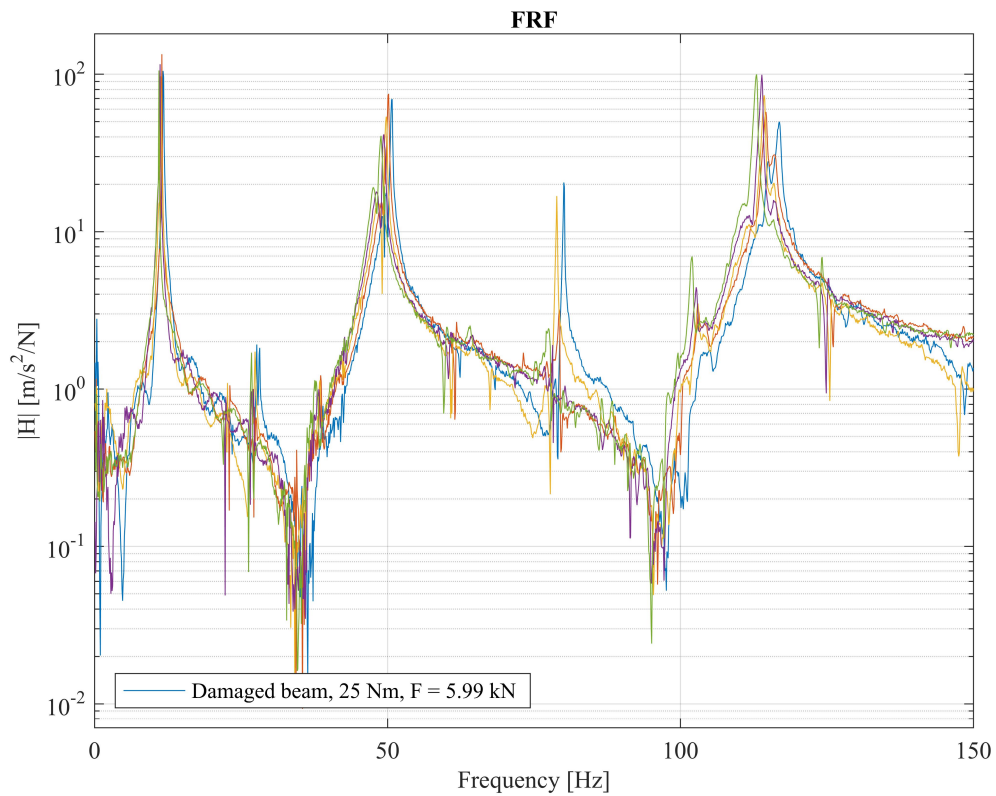
**Figure 2.32. FRFs of healthy and damaged beams under tensile load of 11.70 kN and 11.91 kN.**

Besides the generally lower amplitudes, FRFs of the damaged beam demonstrated some “weak” peaks characterized by low amplitudes, which were more accented in FRFs of the healthy beam. These low peaks were due to the accelerometer positioned close to the node of the corresponding modal shape, but since position of the accelerometer was kept the same for both beams, this means that the modal shapes were slightly different. Thus, the *test detected the asymmetry of the damaged beam*. Figure 2.33 presents a closer look at the FRF of the damaged beam with the low-amplitude peak at the second natural frequency.



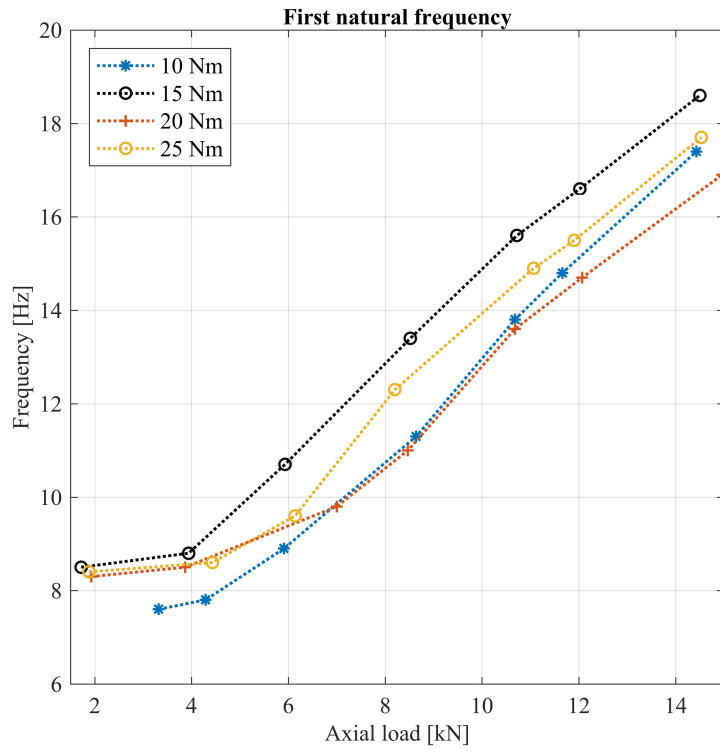
**Figure 2.33. FRF of damaged beam under tensile load of 11.91 kN with a low-amplitude second peak.**

Another typical phenomenon for FRFs of the damaged beam was the “broken” or “doubled” peak (see FRFs of the damaged beam in Figure 2.31 and 2.34). This issue has already been addressed in the beginning of this section and was confirmed by the experiment. Double peaks indicate two resonances that are close together. Behaviour like this is possible for a system with a nonlinearity like a structural crack. We consider the “broken” peak a qualitative damage identifier that is a signal to perform further testing.

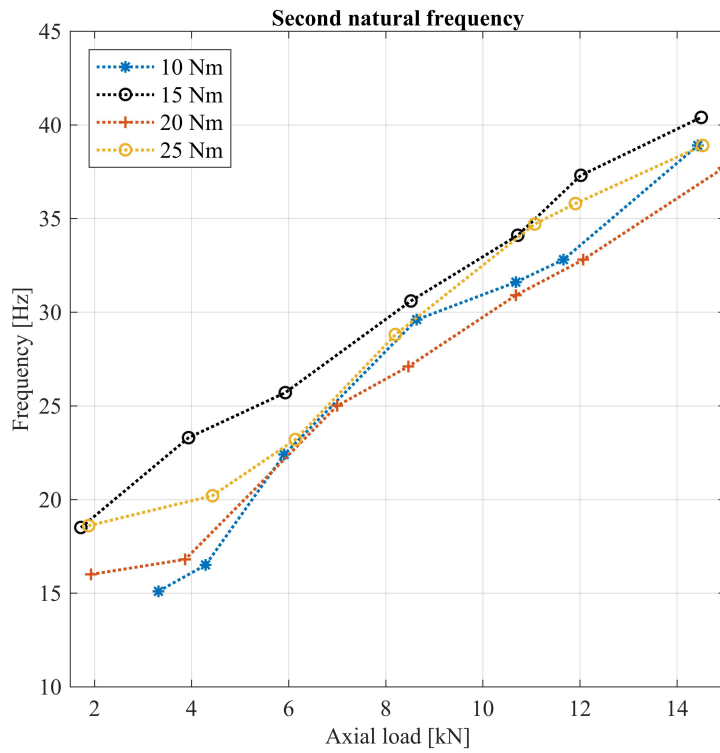


**Figure 2.34. FRFs of damaged beam under tensile load of 5.99 kN.**

The frequencies changed also depending on different torques applied at the joint of the two parts of the beam that represented our “damage”. The nominal value according to specifications for M8 thread is 25 Nm. It was difficult to define a clear tendency in this dependency especially for lower tensile loading, as shown in Figure 2.35 and 2.36.



**Figure 2.35. First natural frequency of damaged beam with respect to axial load and different torques at the joint.**



**Figure 2.36. Second natural frequency of damaged beam with respect to axial load and different torques at the joint.**

## 2.4 Static tests

In the Section 2.3.4 the effect of axial pretension on the natural frequencies of the beam was shown and discussed. Analogically, herein the influence of axial load on the response to static loading is demonstrated.

The experimental setup described in Section 2.2 was initially designed to perform experimental modal analysis of beams. At the same time, some static tests were executed with few additional equipment and they became as well an important part of the experimental studies. The results of the tests were presented through *compliance*, which is the inverse of stiffness, a measure used in fracture mechanics, as it is explained further in Chapter 3.

Two types of static compliance tests were conducted: flexural and axial. Every test was repeated for different tensile loading, mainly from 0 to 15 kN. In this way, we managed to obtain enough information to draw conclusion about:

- Dependency between the axial tension and the beam stiffness;
- Effect of the damage on the beam stiffness.

The tests and their results are treated in the following sections.

### 2.4.1 Flexural test

The flexural stiffness (or compliance) test is schematically represented in Figure 2.37, where the vertical force  $Q$  is equal to  $Mg$  (weight multiplied by  $g = 9.81 \text{ m/s}^2$ ). The weights were positioned in the centre of the beam, in case of the damaged beam it was in vicinity of the defect. The displacement was measured in a point as close as possible to the weight position (point  $B$  in Figure 2.37). Thus, the measured deflection is  $m_y = BB'$ .

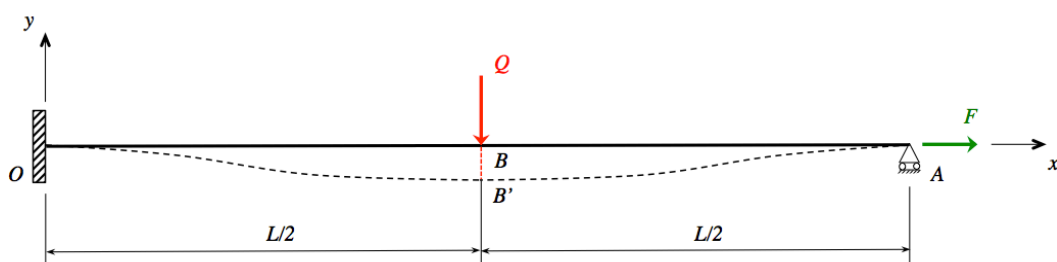


Figure 2.37. Scheme of a beam under flexural compliance testing.



*Compliance*, the inverse of stiffness, is defined by Equation (42) and has the dimension [m/N].

$$C_y = \frac{\delta_y}{Q} \quad (42)$$

Static deflection function  $w(x)$  can be obtained from the differential equation (43) known as the Euler-Bernoulli equation extended for the case of axially loaded beam.

$$\frac{d^2}{dx^2} \left( EI \frac{d^2 w}{dx^2} \right) - F \frac{d^2 w}{dx^2} = q(x) \quad (43)$$

Where  $q(x)$  is distributed vertical load. If the cross-section and material properties are uniform along the beam length, Equation (43) transforms into (44).

$$EI \frac{d^4 w}{dx^4} - F \frac{d^2 w}{dx^2} = q(x) \quad \Rightarrow \quad EI \frac{d^2 w}{dx^2} - Fw = M(x) \quad (44)$$

For the simple case when  $F = 0$ , Equation (44) becomes as follows.

$$EI \frac{d^4 w}{dx^4} = q(x) \quad \Rightarrow \quad \frac{d^2 w}{dx^2} = \frac{M(x)}{EI} \quad (45)$$

Considering the boundary conditions (38), we obtained the deflection function for  $0 < x < L/2$ .

$$w(x) = \frac{Q}{4EI} \left( \frac{x^3}{3} - \frac{x^2}{4} L \right) \quad (46)$$

The maximum deflection is thus equal to (47).

$$\delta_y = \frac{QL^3}{192EI} \quad (47)$$

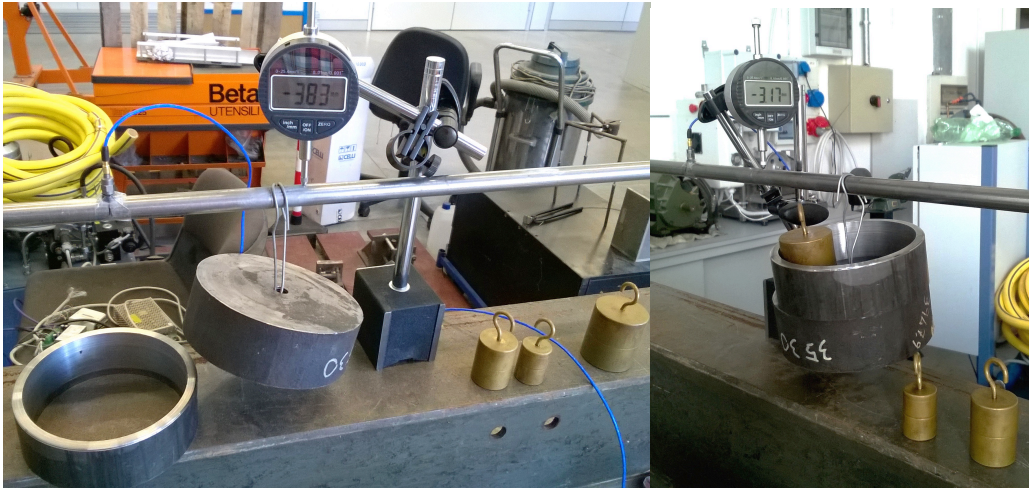
Consequently, the compliance (42) of a healthy unloaded beam is expressed analytically as follows.

$$C_y = \frac{L^3}{192EI} \quad (48)$$

Solution of Equation (44) delivers a more complex expression for deflection that depends on the value of  $F$  and it can be subsequently shown that the compliance reduces when the axial load is applied and increases if a crack is present. Hence, compliance depends on the following factors:

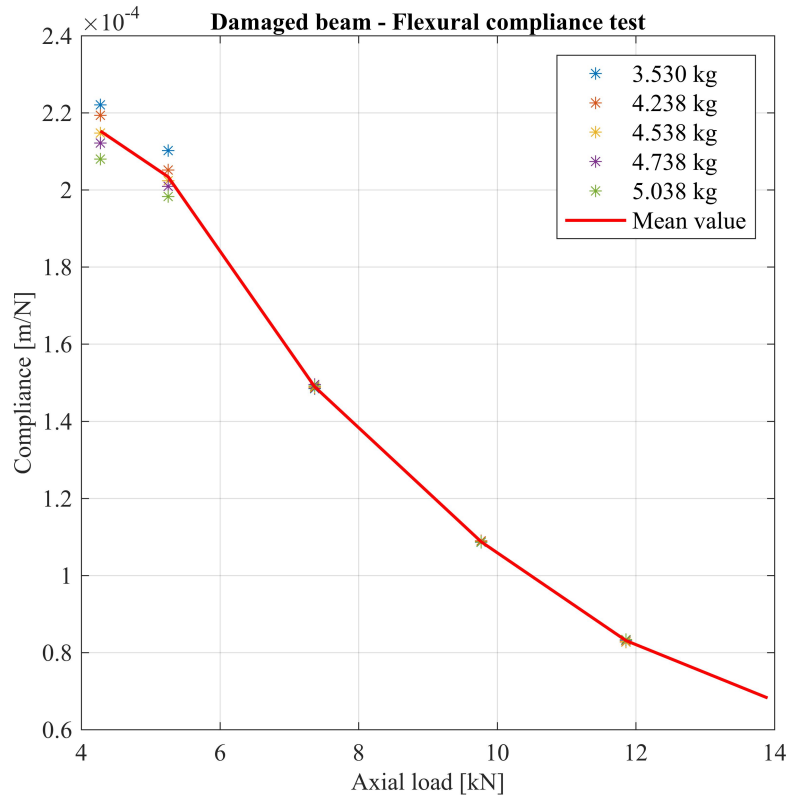
- 1) Boundary conditions at the extremities of a beam or tie-rod
- 2) Material properties
- 3) Cross-section
- 4) Length
- 5) Pretension applied
- 6) Cracks or notches

A vertical force was applied by means of a weight hung close to the centre of the beam. Likewise in the dynamic test, the beams were loaded axially with a hydraulic lift. The loading step was maintained at approximately 1-2 kN and the measurements were started once the beam was straightened with some preload, otherwise, deflection under self weight could interfere with the deflection under the applied vertical load. This vertical displacement was measured by means of a *comparator* on a stand, which enabled high-precision measurements up to hundredth of millimetres. Figure 2.38 pictures one of the experiments in progress.



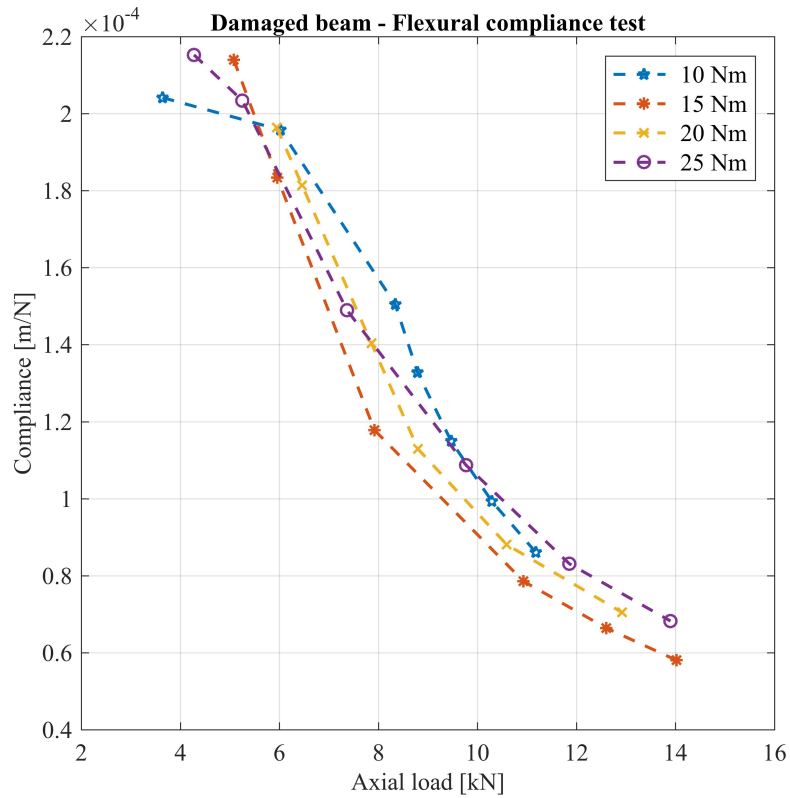
**Figure 2.38. Flexural test setup.**

Equation (44) demonstrates that compliance does not depend on the value of the weight (vertical load). The same conclusion was proved by the first round of tests conducted with five weights ranged from 3.5 to 5 kg. Figure 2.39 shows that a minor difference in the measured compliance is present at a lower level of axial load. Supposedly, this variation is associated with geometrical nonlinearity of a large deflection under self-weight at a low tensile load. Hence, we calculated the mean value of compliance for five measurements with different weights at each axial load.



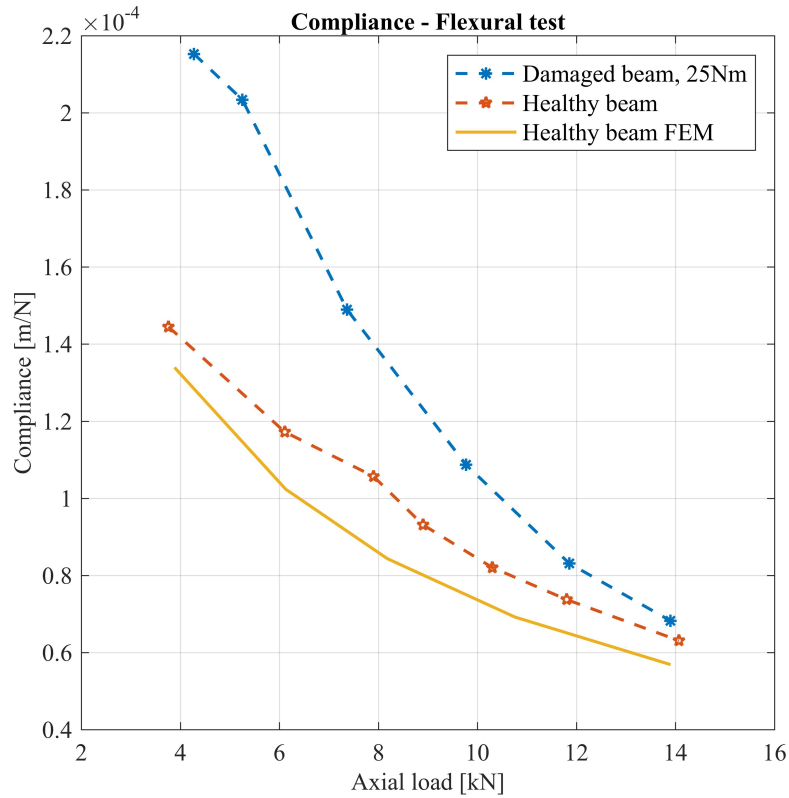
**Figure 2.39. Results of flexural compliance test with five different weights for damaged beam torqued with 25 Nm.**

In Section 2.2.1 we introduced the approach of a crack representation according to which the joint of two parts of the damaged beam is regulated via a torque-wrench with prescribed torques of 10, 15, 20 and 25 Nm. The bending stiffness/compliance tests were performed for each of these various conditions and the results are presented in Figure 2.40. There was no clear dependency observed between the applied torque and the measured compliance. At this point we continued the tests on the beam under the nominal torque of 25 Nm considering it the most representative.



**Figure 2.40. Flexural compliance test of the damaged beam.**

The bending tests confirmed that compliance decay when the axial load increases. In Figure 2.41 we present a comparative graphic of compliance measured via flexural stiffness tests of a “healthy” and “damaged” beam, and of the numerical simulation results.



**Figure 2.41. Flexural compliance of healthy and damaged beams: test vs. FEM simulation.**

It is notable that the FEM model (see Chapter 4 for details) appears to be more rigid than both tested beams. We also observed that the gap between the two curves (healthy and damaged beam with 25 Nm torque applied at the joint) is shrinking as the axial force increases. Thus, the higher the load, the less significant became the influence of the defect on the bending compliance. In other words, the effect of the damage, that locally decreases the beam stiffness, becomes minor compared to the stiffening due to the tensile load. In fact, the compliance increase caused by crack opening is compensated by the reduction of compliance due to tension, and the defect becomes more difficult to detect.

## 2.4.2 Tensile test

Another compliance test concerned the measurement of elongation, i.e. axial displacement of the beam under increasing tensile load. As in the previous test, the comparator was used to measure displacements as pictured in Figure 2.42.

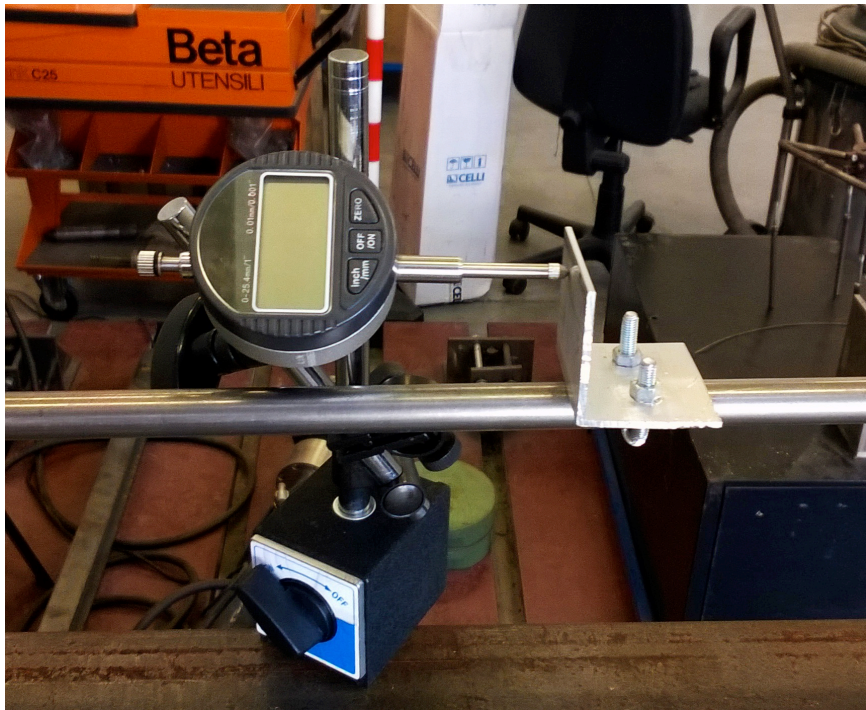


Figure 2.42. Axial stiffness test setup.

The axial stiffness test is schematically represented in Figure 2.43. The axial displacement  $\delta_x = AA'$  was measured for gradually increasing tensile load.

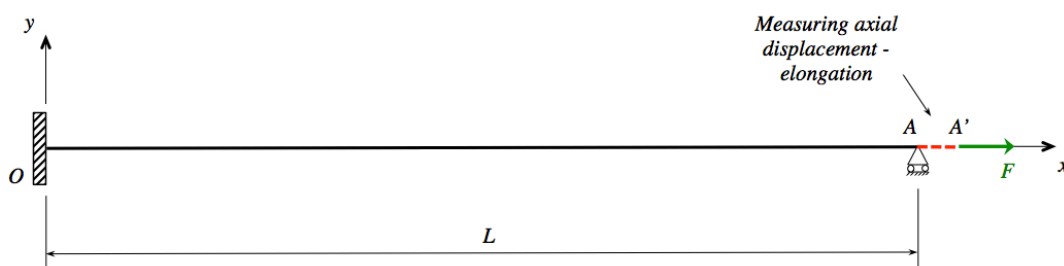


Figure 2.43. Scheme of a beam under axial compliance testing.

Theoretically for a “healthy” beam in the linear field the axial displacement is equal to elongation of the beam due to the linear deformation under axial tension (49).

$$\delta_x = L_1 - L = \varepsilon_x L \quad (49)$$

From the Hooke’s law, the linear deformation is expressed through stress and Young’s modulus (50).

$$\varepsilon_x = \frac{\sigma_x}{E} = \frac{F}{EA} \quad (50)$$

Hence, the axial displacement is in linear dependence from the tensile load as given by Equation (51).

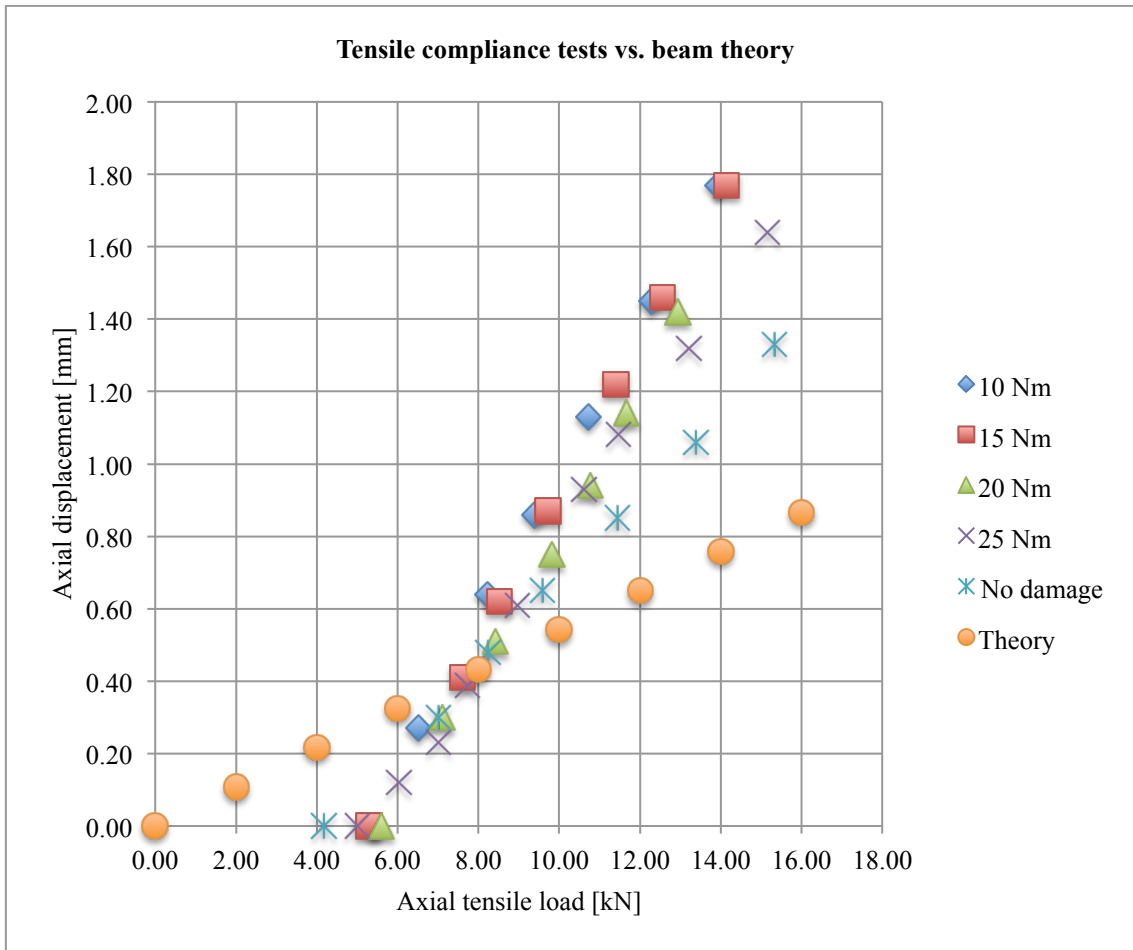
$$\delta_x = \frac{FL}{EA} \quad (51)$$

Consequently, the axial compliance of a healthy beam is expressed via Equation (52). The value is represented as a column titled “Theory” in Figure 2.45.

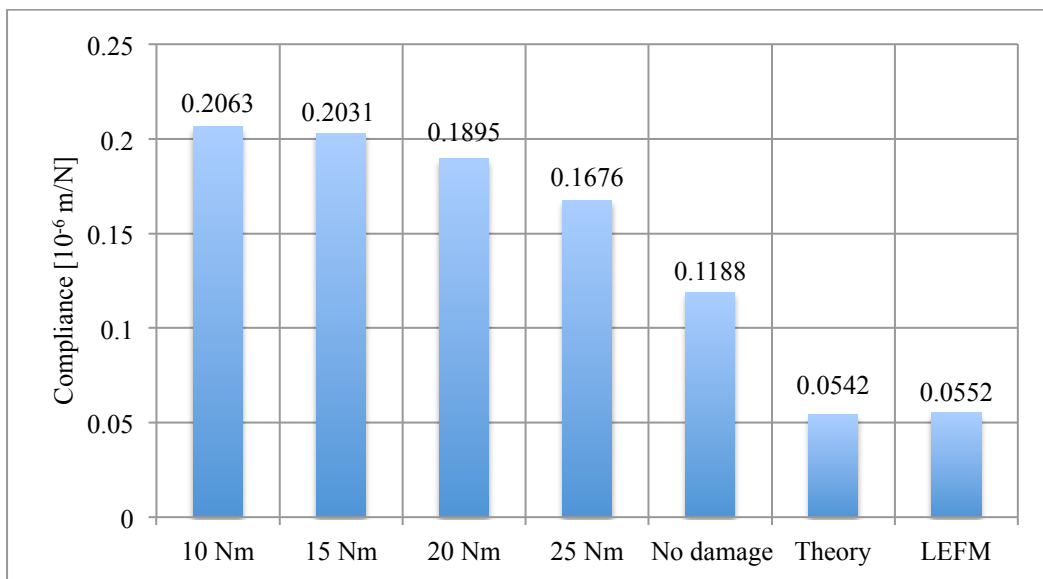
$$C_x = \frac{\delta_x}{F} = \frac{L}{EA} \quad (52)$$

The displacement-load curves obtained from the tensile compliance tests are contained in Figure 2.44. These curves were very close to straight lines and the approximation with linear polynomials provided the resulting values of compliance for each tested sample (see Figure 2.45). It is clear that compliance was inversely proportional to the torque applied at the joint between the two parts of the damaged beam (as expected, the higher the torque, the lower compliance). Still, the healthy beam remained more rigid than the damaged for all the torque values in the range, and the theoretical model, in its turn, was stiffer than the real healthy beam.





**Figure 2.44. Axial displacement vs. tensile load for healthy and damaged beams.**



**Figure 2.45. Axial compliance of healthy and damaged beams.**

When the axial load was applied, the increasing tensile stress  $\sigma$  tended to separate the contact surfaces. This is alike to what would happen if the tie-rod incorporated a real crack. The isolated compliance of the damaged beam due to the presence of a crack is further addressed in Section 3.5 of Chapter 3 “Fracture mechanics approach”. Using the linear elastic fracture mechanics (LEFM) methods we evaluated the augmentation of compliance caused by the damage. The result is given as a column titled “LEFM” in Figure 2.45. The theoretically estimated compliances resulted lower than experimentally measured, but the predicted trend was present.

## 2.5 Conclusions

This Chapter revealed a method of damage detection in metal beams by means of modal analysis. The procedure of vibration measurement previously approbated in situ, as described in Chapter 1, is of a simple execution. The subsequent data analysis leads to conclusions on structural damage presence in tested tie-rods.

The method was developed ex situ utilizing a particular experimental rig. The constructed experimental setup enabled testing of healthy “healthy” beams and “damaged” beams controlled defect. The artificial defect was simulated throughout an M8-type bolt connection of two parts of a beam, i.e. a beam of the same cross-section and material as the “healthy” one was cut in two and then a thread and a corresponding hole were carved to create the bolt connection. The two parts connected together formed the “damaged” beam of the exact same length and other properties as the “healthy” one. The bolt between the two parts could be tightened with an adjustable torque using a torque wrench at one edge of the beam.

The acquisition of vibrations was carried out for the damaged and non-damaged beams under variable axial load and for different torques applied at the joint. The tensile load was varied from 0 to 30 kN for the normal beam and from 0 to 14 kN for the damaged sample. Furthermore, the experimental data has been elaborated in terms of modal analysis: frequency response functions, natural frequencies, and modal damping ratios. The laboratory tests have revealed that the defect noticeably decreased the

natural frequencies of the beam and increased the modal damping ratios of the response. It also detected the asymmetry of the damaged beam.

By means of dynamic analysis we managed to spot the possible damage markers that can be applied to *in situ* testing of tie rods, *id est*:

- i. natural frequencies more than 10% lower than available estimated values (estimated based on the loading, length, cross-section, assumed material parameters and evident boundary conditions);
- ii. elevated damping ratios of the natural modes;
- iii. unusual nonlinearities of the FRF, e.g. broken or doubled peaks;
- iv. overall highly damped response characterized by small amplitudes of the FRF.

The static compliance tests confirmed as well the system stiffness reduction for the damaged beam compared to the healthy one. These results were correlated with the tensile compliance of the equivalent crack configuration determined via the linear elastic fracture mechanics approach (see Chapter 3 for details).

---

# Chapter 3

## Fracture mechanics approach

*This Chapter is dedicated to the classification of cracks in round bars and provides justification regarding the damage representation adopted in Chapter 2. The results of static compliance tests are hereby correlated with calculations according to the linear elastic fracture mechanics approach.*

### 3.1 Introduction

The majority of structure design problems and strength calculations are solved in the field of the theory of elasticity, presuming that the equivalent stress in the loaded structure does not exceed the yield stress. Otherwise, irreversible plastic deformation occurs and the theory of plasticity should be used. Tie-rods, the subject of the present research, are loaded in tension with a quasi-constant load, that may gradually change with time due to displacements in supported building, loose of anchoring system, environmental conditions, etc. This tensile load, however, is not of a cyclic nature. Thus, the fracture processes, crack initiation and propagation, in tie-rods are most likely

to be related to corrosion. Figure 3.1 illustrates an example of a crack in an ancient tie-rod. Consequences of material aging and corrosion are quite evident from the image.



**Figure 3.1. Crack in an ancient iron tie-rod**

(courtesy of the NDT laboratory of Politecnico of Milan, *M. Bellanova et al.* [95]).

Stress corrosion is a phenomenon usually occurring at relatively low stress levels, when the macroscopic material behaviour is characterized by known elastic constants: Young's modulus ( $E$ ) and Poisson's ratio ( $\nu$ ). In the next Sections the passage from the "damage" representation, adopted in the previous Chapter 2, to equivalent cracks is performed, and the stress concentrations are evaluated and compared.

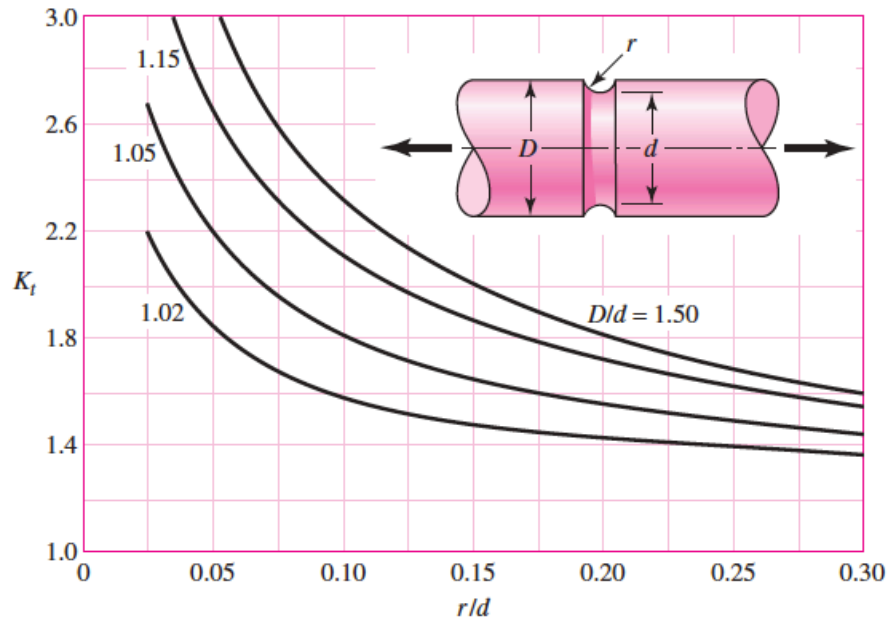
## 3.2 Stress concentrations

In case a structure incorporates a notch, stress distribution becomes inhomogeneous and is characterized by a stress concentration at the root of the notch. The theoretical *stress concentration factor*  $K_t$  is defined as the ratio between the maximum stress at the root of the notch  $\sigma_{\max}$  and the nominal stress  $\sigma_{nom}$ , which would be present if a stress concentration did not occur, *J. Schijve* [96].

$$K_t = \frac{\sigma_{\max}}{\sigma_{nom}} \quad (53)$$

The stress concentration depends on the notch configuration. The values of  $K_t$  can be obtained by analytical or numerical calculations or via experiments, e.g. strain gauge or

photo-elastic measurements. Profound information on stress concentration can be found in the work of *R. Peterson* [97]. The  $K_t$  values are tabulated for all the common geometries of notches and are contained in handbooks, for instance the book by *J.E. Shigley* [98] can be consulted. Figure 3.2 shows a graph of  $K_t$  for a grooved round bar in axial tension.



**Figure 3.2. Stress concentration factor  $K_t$  for a grooved round bar in tension.**

Stress distribution around notches is important for crack initiation and subsequent crack growth. But for a crack tip the  $K_t$ -concept is no longer applicable, because a crack is a notch with a zero radius, thus, the theoretical stress concentration factor becomes infinite for any crack length. The appropriate paradigm to describe the severity of the stress concentration at the crack tip is the *stress intensity factor*  $K$  (SIF). It was first developed in the works of *G. Irwin* [99-100]. The concept of *linear elastic fracture mechanics* is to apply the stress intensity factor to analyse crack data and to predict crack growth. The stress intensity factor  $K$  is defined by Equation (54).

$$K = \beta\sigma\sqrt{\pi a} \quad (54)$$

Where  $\sigma$  is the loading stress,  $\beta$  is a dimensionless coefficient that depends on geometry of the element and  $a$  is the length (depth) of the crack. The stress distribution at the crack tip is, thus, represented via a linear function of  $K$ . This conceptual difference is important to justify the manipulations (see Chapter 2) performed on a beam to represent a defect as close as possible to a real crack in a structure. The “damage” formed by connecting two parts of the beam enabled the contact between the surface of the defect. Otherwise, the defect would be simply a notch.

In real structures cracks are most likely to grow in the direction perpendicular to the maximum principal stress, i.e. the tensile stress in the case considered hereby. This stress tends to open a crack and the corresponding type of opening is called *Mode I*. Along with that there are Mode II (in-plane shear), Mode III (transverse shear) and mixed modes. An exact analytical solution for the stress distribution in the vicinity of a crack has been derived for an infinite sheet with a crack loaded in Mode I. The stresses can be presented in the form of Equation (55).

$$\sigma_{ij} = \frac{K}{\sqrt{2\pi r}} f_{ij}(\theta) \quad (55)$$

Where  $r$  and  $\theta$  are the polar coordinates in the vicinity of the crack tip, and  $f_{ij}$  are trigonometric functions defining the stress distribution around the crack tip. The term  $1/\sqrt{2\pi r}$  indicates how rapidly the stress decreases as the distance from the crack tip increases. In this solution the theoretical stress at the crack tip ( $r = 0$ ) is infinite, which is practically impossible and this singularity means that plasticity must be present at the tip. For the infinite sheet the geometry correction coefficient  $\beta$  is equal to 1. Other cases of common geometries and loading modes have been investigated and most of the solutions for  $K$  ( $\beta$ ) can be found in appropriate handbooks by *Y. Murakami* [101], *H. Tada*, *P. Paris* and *G. Irwin* [102], *D. Rooke* [103]. Unlike the stress concentration factor  $K_t$ , which is a dimensionless coefficient that accounts only for the geometry of the specimen, the stress intensity factor  $K$  indicates the severity of the stress intensity and takes into account the load applied, as well as geometry, since it contains the dimensionless shape factor  $\beta$ .  $K$  has the dimension of  $Pa\sqrt{m}$ .

### 3.3 Cracks in round beams

In the framework of the research reported hereby we tested a beam with a circular defect introduced by means of joining two parts of the beam with adjustable torque (see Chapter 2). This kind of damage is approximating to a *ring-shaped crack*. The cross-section with the defect is schematically represented in Figure 3.3, where the inner diameter  $d$  is the diameter of the M8 thread equal to 8 mm and the diameter of the beam  $D$  is 16 mm.

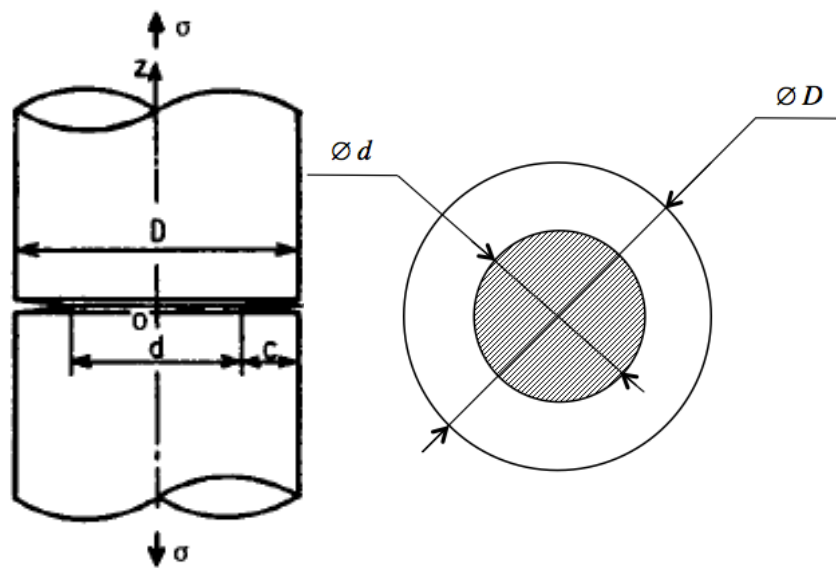


Figure 3.3. Beam with a circular defect loaded in tension.

The crack depth  $a$  in this case is expressed as follows.

$$a = \frac{D-d}{2} \quad (56)$$

SIF solutions for this type of cracked beams loaded in pure tension (mode I) were reported in the Stress intensity factors handbook by *Y. Murakami* [101].

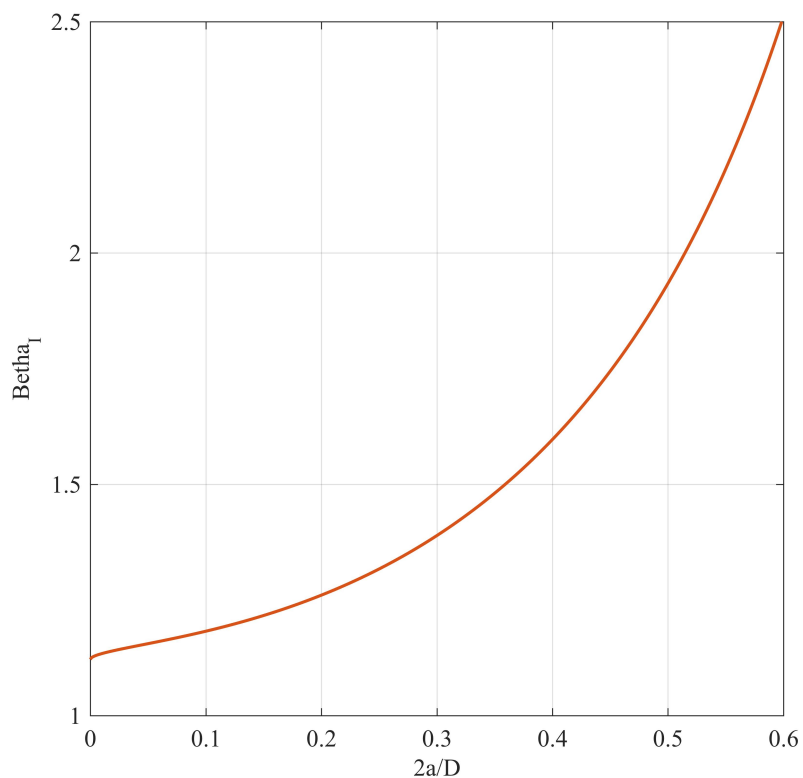
$$K_I = \beta_I \sigma \sqrt{\pi a} \quad (57)$$



The shape factor  $\beta_I$  is given as a polynomial function of the beam cross-section geometry.

$$\beta_I = \frac{1}{2} \left[ \left( \frac{d}{D} \right)^{-\frac{3}{2}} + \frac{1}{2} \left( \frac{d}{D} \right)^{-\frac{1}{2}} + \frac{3}{8} \left( \frac{d}{D} \right)^{\frac{1}{2}} - 0.363 \left( \frac{d}{D} \right)^{\frac{3}{2}} + 0.731 \left( \frac{d}{D} \right)^{\frac{5}{2}} \right] \times \left[ 1 + 0.1 \left( \frac{2a}{D} \right)^{\frac{1}{2}} \left( 1 - \frac{2a}{D} \right)^2 \right] \quad (58)$$

Figure 3.4 shows the dimensionless stress intensity factor  $\beta_I$  as a function of a geometric ratio  $2a/D$ .



**Figure 3.4. Dimensionless stress intensity factor  $\beta_I$  for a ring-shaped crack in a round beam.**

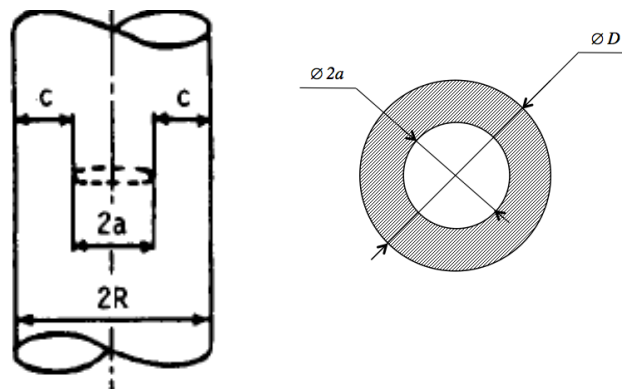
In the tested “damaged” beam the “crack” depth was equal to  $a = 4 \text{ mm}$ , hence,  $d/D = \frac{1}{2}$  and  $2a/D = \frac{1}{2}$ , and for these parameters  $\beta_I$  results 1.940. The error of this solution is

under 0.1% [101]. Thus, the stress intensity factor  $K_I$  for this particular crack can be expressed as a linear function of tensile load  $F$  with an angular coefficient  $\lambda$ .

$$K_I = \lambda F \quad (59)$$

The ring configuration was chosen for the reason that it was possible to emulate joining two parts of the beam. Other crack shapes like a disk (inner crack) or a semi-elliptical surface crack are quite complicated to introduce into a two-meter long slender beam as it can be done for standard samples on an MTS machine. However, we also review other defect types equivalent to the ring-shaped crack based on the relative depth of the crack.

The case of a beam with an *inner circular crack* is shown in Figure 3.5.

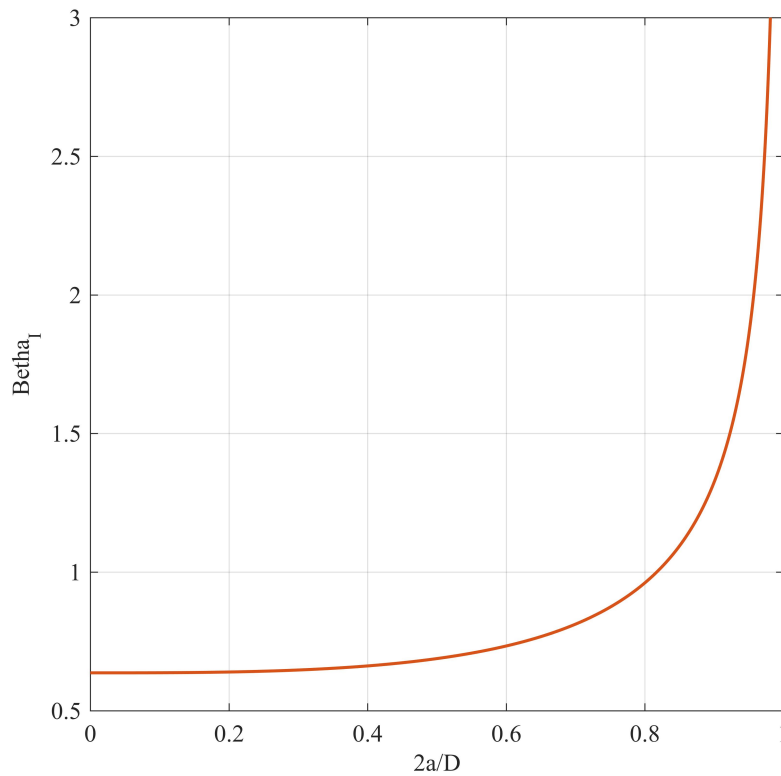


**Figure 3.5. Beam with a disk-shaped defect loaded in tension.**

Hence, SIF is expressed, as previously, by Equation (57). The dimensionless stress intensity factor  $\beta_I$  for a beam with an embedded disk-shaped crack under tensile stress is given as a function of the relative crack depth  $2a/D$  by Equation (60) [101].

$$\beta_I = \frac{2}{\pi} \left( 1 + \frac{1}{2} \frac{2a}{D} - \frac{5}{8} \left( \frac{2a}{D} \right)^2 \right) + 0.268 \left( \frac{2a}{D} \right)^3 \left[ 1 - \left( \frac{2a}{D} \right)^2 \right]^{-1} \sqrt{1 - \frac{2a}{D}} \quad (60)$$

The corresponding graphical representation is plotted in Figure 3.6.



**Figure 3.6. Dimensionless stress intensity factor  $\beta_F$  for a disk-shaped crack in a round beam.**

We assume that the equivalent configuration of this crack type has the crack length of  $2a = 8 \text{ mm}$ , having the ratio  $2a/D = 1/2$ , thus,  $\beta_I$  results in approximately 0.688. The error of this solution is under 1% as reported in [101].

Next, the configuration of a beam with a *semi-elliptical surface crack* is shown in Figure 3.7, where  $2a$  and  $2b$  are the ellipse axes. The stress intensity factor is expressed in form of Equation (61), where  $b$  is the depth of the crack.

$$K_I = \beta_I \sigma \sqrt{\pi b} \quad (61)$$

The shape factor  $\beta_I$  is tabulated for different ratios of crack and beam geometry  $2b/D$  and  $b/a$  [101], i.e.  $\beta_I$  depends on two dimensionless geometric parameters and the  $K$ -solution is two-parameter unlike in the previous cases. The stress intensity in this asymmetrical case varies along the crack front. Figure 3.8 presents some graphics for  $\beta_I$  in the deepest point of the crack front (point  $C$  in the section sketch in Figure 3.7).

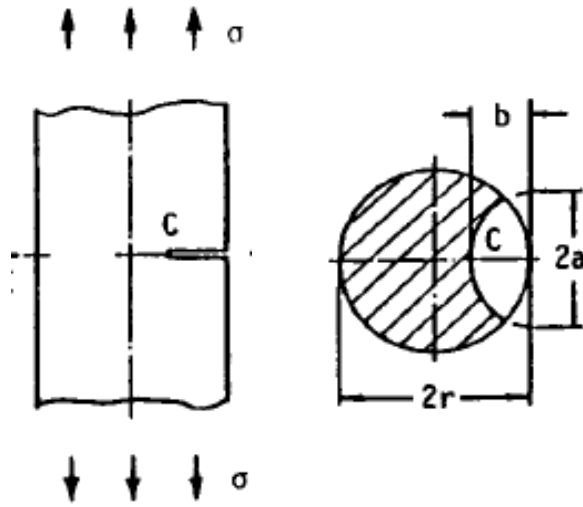


Figure 3.7. Beam with a semi-elliptical defect loaded in tension.

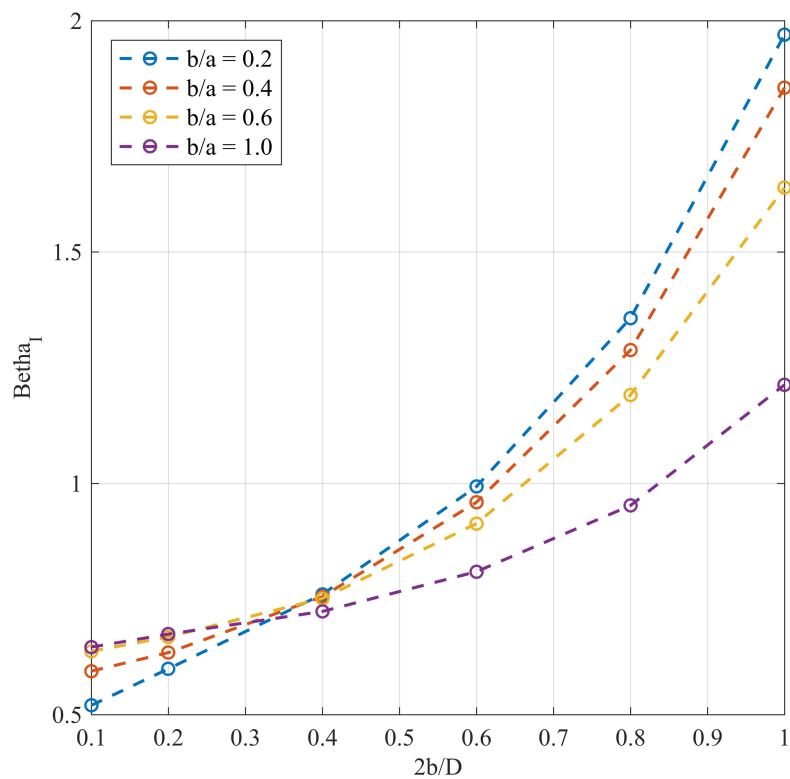
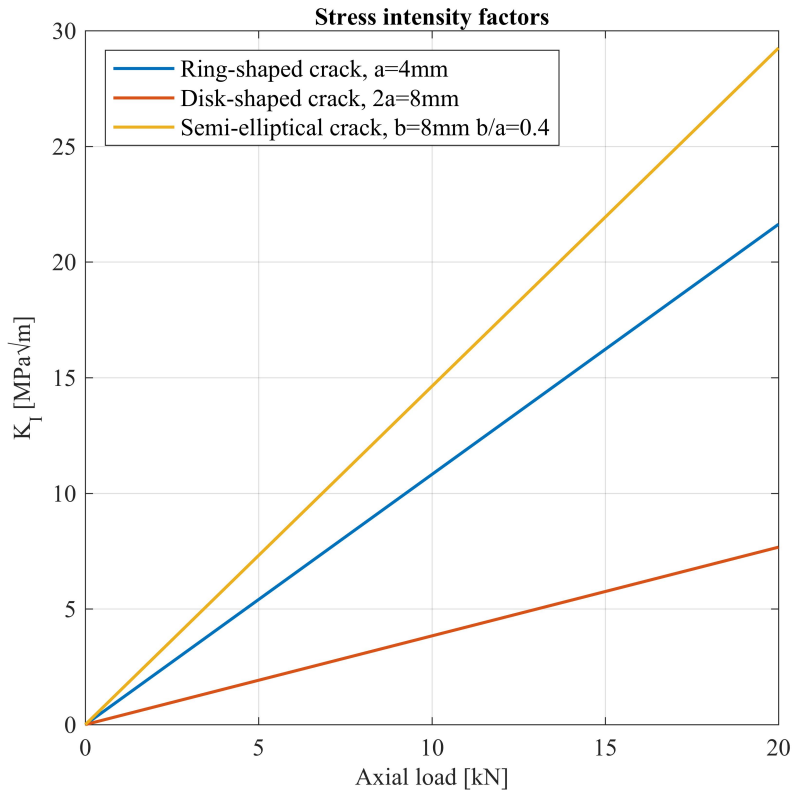


Figure 3.8. Dimensionless stress intensity factor  $\beta_I$  for a semi-elliptical crack in a round beam.

One of the equivalent configurations of the semi-elliptical crack is presumed to have the crack depth of  $b = 8 \text{ mm}$ , hence, the ratio  $2b/D = 1$ . If the ellipse parameter is taken

as  $b/a = 0.4$ , the value of  $\beta_I = 1.855$  is obtained. The error of this solution is about 1% [101].

The stress intensity factor, as previously stated, linearly depends on the tensile load, see Equations (59). SIFs of the three reviewed crack configurations are illustrated in Figure 3.9 for variable axial load.



**Figure 3.9. Stress intensity factors  $K_I$  vs. axial load for three equivalent cracks: ring-shaped, disk-shaped and semi-elliptical.**

It is notable that the equivalent crack with an asymmetrical configuration, i.e. the semi-elliptical crack, demonstrates 35% higher stress intensity compared to the symmetrical ring-shaped crack represented by the “damage” in the tested beam.

### 3.4 Compliance

In engineering static displacement under loading is often referred to as compliance, which is the inverse of stiffness. Compliance methods in fracture mechanics use this characteristic to evaluate dimensions of defects, crack closure and residual stresses. Some of these methods were summarized in works of *A. Fleck* [104], *G. Urriolagoitia-Sosa et al.* [105] and *J. Toribio et al.* [106-108].

It has been mentioned previously that presence of a crack decreases the local stiffness of a beam; hence, speaking in terms of fracture mechanics, a crack increases the compliance of a structure. Changes in compliance results not only in decrease of natural frequencies, as demonstrated in Chapter 2, but also in a load redistribution inside a structure, which can lead to further crack growth and loss of structural integrity.

Compliance methods consist of applying a certain load to a structure and of measuring the displacement of the load application point. Measuring of the additional compliance occurred due to presence of a crack allows to estimate the crack length. However, the measuring techniques are very sensitive with respect to the point of application, since according to the Saint-Venant principle a crack changes the mechanical properties only of a region adjacent to it.

Let us presume that a beam incorporates a crack, then the local axial displacement under a tensile load  $F$  due to crack opening is  $\tilde{\delta}_x$  and the compliance is defined similar to Equation (52).

$$\tilde{C}_x = \frac{\tilde{\delta}_x}{F} \quad (62)$$

The axial displacement measured during static tests in Chapter 2 consisted of *an elongation* due to linear elastic deformation and of *a displacement due to crack opening*. Likewise, the measured compliance of the structure incorporated a part defined by Equation (52) and a part caused by the crack presence. It has been demonstrated that the isolating compliance  $\tilde{C}_x$  is a function of the crack length/depth [99-104]. For this purpose the strain energy density  $U$  is expressed taking into account the equivalence

between the energy release rate  $G$  and the stress intensity factor in plane strain  $K$ , which is valid for the Mode I loading (pure tension).

$$dU = GdA = \frac{K^2(1-\nu^2)}{E}dA \quad (63)$$

Alternatively, the strain energy density for a cracked beam subjected to tensile load is expressed as follows.

$$dU = \frac{1}{2}Fd\tilde{\delta}_x = \frac{1}{2}F^2d\tilde{C}_x \quad (64)$$

In Equation (63)  $dA$  is the differential of the crack area. The ring-shaped crack of a depth  $a$ , reviewed in the previous Section (see Fig. 3.3), is the closest configuration to the damage in the tested beam. Thus,  $dA$  is delivered by Equation (65) and the stress intensity factor in this case is given by Equation (57).

$$dA = \pi(D - 2a)da \quad (65)$$

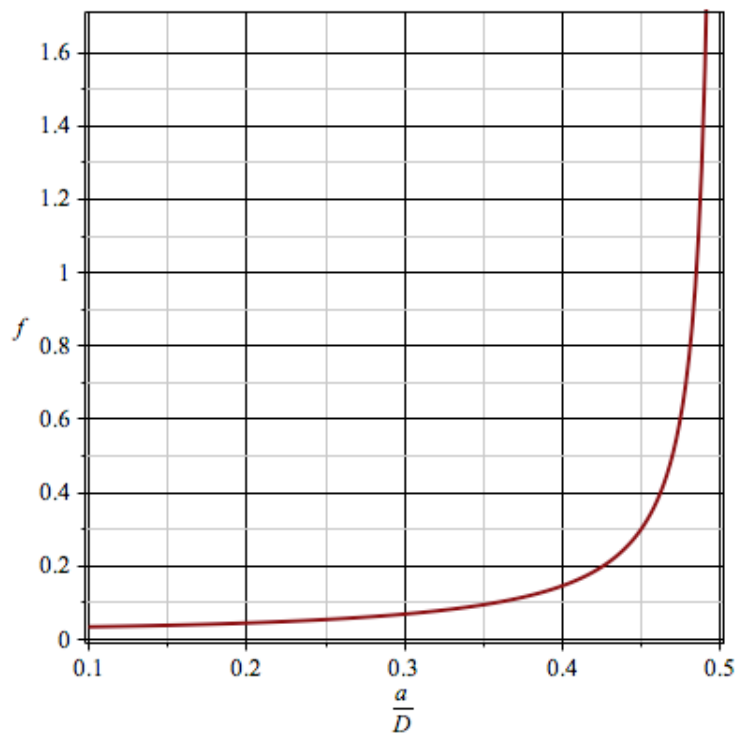
Since Equations (63) and (64) are equivalent, the isolating compliance due to tensile load is obtained.

$$\tilde{C}_x = \frac{32(1-\nu^2)}{D^4E} \int_0^a \beta_l^2 (Da - 2a^2) da \quad (66)$$

The dimensionless stress intensity factor  $\beta_l$  is defined as function of the crack-beam geometry ( $a/D$ ) by Equation (58). The compliance  $\tilde{C}_x$  can be represented through the *dimensionless compliance*  $f$ , which is as well a function of the ratio  $a/D$ , when the integral in Equation (67) is computed.

$$f = \frac{1}{2D^3} \int_0^a \beta_l^2 (Da - 2a^2) da \quad (67)$$

The graphic of the dimensionless compliance with respect to the ratio  $a/D$  is presented in Figure 3.10. The symbolic integration and calculation of coefficients was carried out in *Maple* software. These results correlate with profound studies of different crack configurations in round bars reported previously by *J. Toribio et al.* [107-108].



**Figure 3.10. Dimensionless compliance of a beam with a circular defect loaded in tension.**

For the crack configuration in the tested damaged beam  $f$  results 0.05427 and the compliance  $\tilde{C}_x$ , correspondingly, 9.8765E-10 m/N. This result was reported previously in Chapter 2 (see Figure 2.45) and correlated with experiments conducted for the damaged and healthy beams. Obviously, some particular equipment is required in order to measure more precisely the local displacement due to crack opening. Generally, knowing the sample configuration and having measured the compliance with the precise



gauges, the crack length/depth can be estimated based on the theoretical expression for dimensionless compliance.

## 3.5 Conclusions

In this Chapter we reviewed the elements of linear elastic fracture mechanics (LEFM) that were helpful in justifying the approach of physical crack representation adopted in this research. Understanding of the mechanisms of crack initiation and propagation remains a challenge of mechanics, thus, clearly, introducing a controlled defect into a structure element like a long slender beam is a complicated task. Previously, we described the “damaged” tie-rod, which was composed of two parts joined with a bolt under corresponding torque. This permitted to maintain the contact condition between the “crack” surfaces. Hence, we obtained a beam with a known and characterized defect, a ring-shaped crack. Further, we investigated other crack configurations typical for a round beam. It was concluded that equivalent asymmetrical cracks (a semi-elliptical or a straight-fronted edge cracks) are more dangerous for the structure integrity due to higher stress intensity at the crack tip.

In order to determine the crack type, a dynamical analysis described in Chapter 2 is not enough. Attempts can be made to fulfil this task performing static tests that measure compliance, making use of specific high-precision equipment (e.g. crack mouth gauge). In this way the crack opening load can be measured and a crack depth can be estimated based on approximations considering the specimen configuration.

It is hard to predict the load changes throughout lifetime of tie-rods, since the loading conditions depend on the behaviour of the building foundation and masonry. Even though we consider the loading as quasi-static in reality it may change unexpectedly due to earthquake, or some less dangerous event, leading to failure of cracked tie-rods. That is a reason why it is important to be able to detect structural damages during the regular health-monitoring of tie-rods.

The interference of fracture and dynamical behaviour of a structure remains a very tricky problem with many unknowns. For now there is no doubt that cracks can be detected via a vibrometric measurement and the next step to the full picture would be to enable the estimation of crack configuration, depth and position.

---

# Chapter 4

## FEM simulations

*This Chapter reveals the main features of numerical modelling used to support the experimental approach reported in the first two Chapters. Static and modal analyses have been carried out in the finite element method software, including crack modelling by means of available tools.*

### 4.1 Introduction

A British professor George E. P. Box once said, ‘*All models are wrong, but some models are useful*’. He was referring to mathematical models in statistics, but I suppose this statement nowadays can be as well extrapolated to computer-aided numerical simulations. Computer modelling has become a powerful instrument of engineering design, optimization and analyses of all kinds. Finite element method (FEM) introduces a universal approach to solution of any engineering problem. Together with computer-aided engineering (CAE) it empowers scientists to perform complicated simulations in multiphysical environment using handy tools and clear interface. But the transition of reality into purely mathematical frames comes for a price, namely, convergence problems, lack of input data, unrealistic results, etc.

The basic principle of FEM is discretization: a continuous system, e.g. a beam, with an infinite number of degrees of freedom is divided into elements and nodes, forming an equivalent system with a limited number of *dofs*

FEM modelling raises many issues, some of which are addressed in this Chapter. The broad choice of options provided by CAE software requires the engineers to master the ability to critically prioritise physical phenomena that have influence on the problem, to simplify geometries, to choose correctly interactions, boundary conditions, material models, to create efficient meshes, and to make reasonable assumptions about unknown parameters. Further on the stage of postprocessing, it is, of course, utterly important to perceive and validate the results. Sometimes multiple software packages are used in order to evaluate quality of the analyses outputs. When experimental data on the problem is available, the validation is performed confronting numerical results with real-life tests.

Simulations might be wrong, sometimes too far from experimental reality or analytical solutions, but they are still useful. The main reason is that thanks to the computerized nature they are irreplaceable for sensitivity analyses and optimization of even large-scale problems. In this research we used commercial CAE software Abaqus 6.13 to model tie-rods with or without cracks and execute static, dynamic and modal analyses. Using parametric models helps to define unknown properties by matching numerical and test data, as it has been performed in the frame of axial load identification method treated in Chapter 1. The FEM simulations, as described in the following sections, also supported the experimental damage detection technique proposed in Chapter 2.

## 4.2 Beam and crack modelling

The usual sequence of steps required to perform an effective FEM analysis is as follows:

- Create or import a CAD model of the structure, if it consists of multiple parts, then create an assembly;
- Introduce a crack or a notch into the damaged part of the structure, if necessary;

- 
- Create and then assign to the structure parts the appropriate material and geometric properties (including modulus of elasticity, Poisson's ratio, density, and cross-section shapes and dimensions if applicable);
  - Create a proper structured meshing of the parts, if required create geometrical partitions first;
  - Choose and assign appropriate element type based on the scope of analysis;
  - Create interactions, contact conditions or engineering
  - Create steps of analysis: static (e.g. pretension), frequency (modal), dynamic (time-stepped), steady state (frequency domain stepped), and other;
  - Create field and history outputs of required variable (e.g. displacements, velocities, accelerations, deformations, stresses, etc.);
  - Create loads and boundary conditions inside the corresponding analysis steps;
  - Create the job and run the analysis;
  - Visualize, extract, export and interpret the output in the postprocessing phase.

In FEM a tie-rod can be modelled using specific Beam elements. In this case the beam is represented with a one-dimension body, i.e. a wire (line, curve, polyline), and cross-section shapes and dimensions are assigned to this body as one of the properties. The Beam model shows good results for analyses of long slender beams without defects. For Beam elements there is an option of modelling the axial tensile load as a bolt pretension load.

The Beam model was adopted in the numerical part of the axial load identification method described in Chapter 1. Tie-rods were modelled in FEM software using 50-60 B31 2-node linear beam elements in 3D space (see Figure 4.1), implying Timoshenko's beam theory, which allowed taking into account irregular cross-sections, added masses, elastic supports, etc.



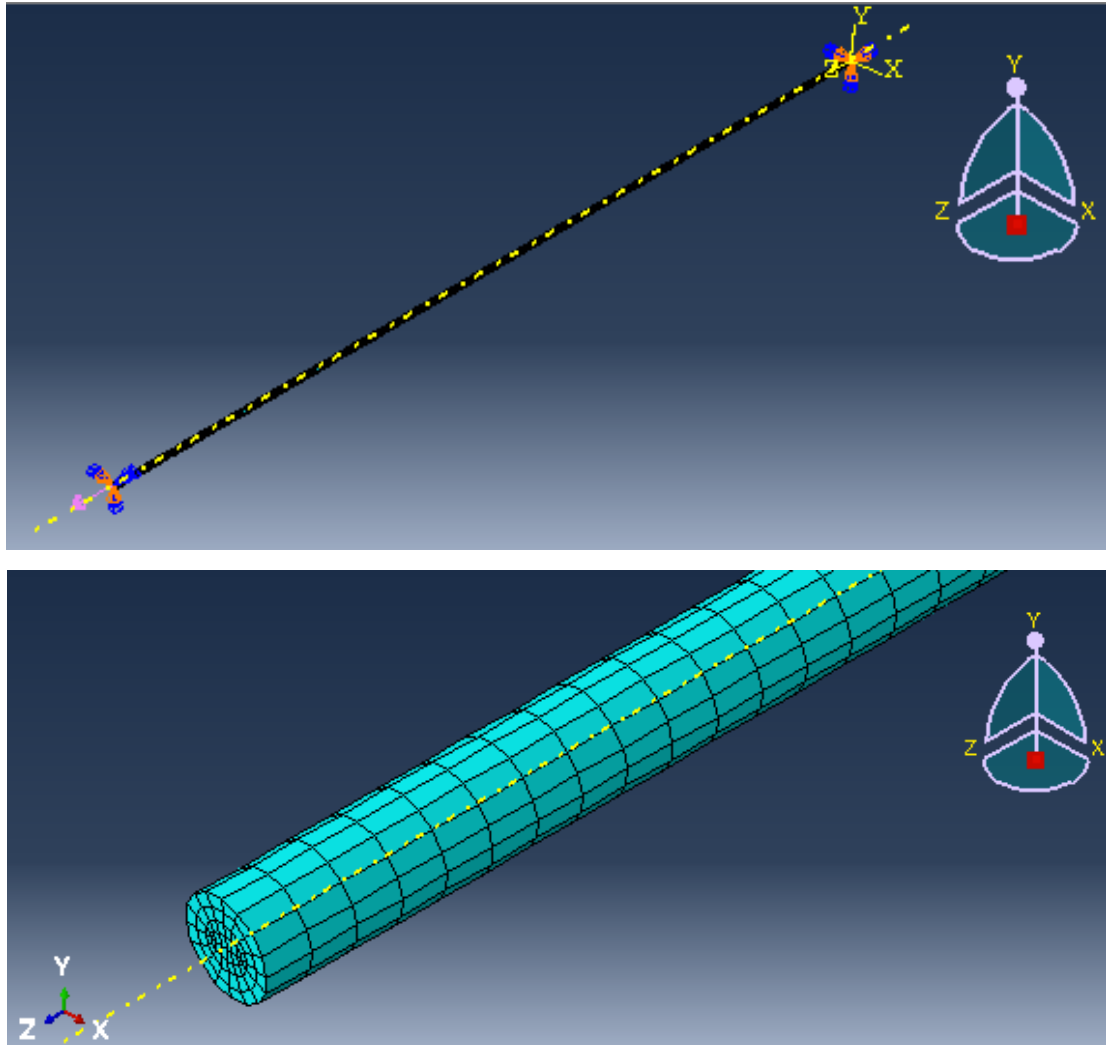
**Figure 4.1. Tie-rod represented with Beam elements in Abaqus CAE.**

The FEM simulation was divided into two steps: as a first step a pretension load  $F$  was applied to the beam and as a second step the modal analysis was performed. The FEM model was parametric, since the tensile load and elastic foundation parameters were unknown. Idea here was tuning these parameters in order to match results of physical tests and FEM simulations. Optimization criterion was represented by a residual error between natural frequencies defined via experimental and numerical modal analyses, calculated according to Equation (18). Hence, the minimum of the multi-parameter function  $R$  delivered the optimal solution. By using a parametric FEM model the representation of a tie-rod became flexible and first 6 natural frequencies were matched with overall accuracy up to 1%.

Parameterisation of the FEM model was achieved by direct coding of the analysis input file \*.inp, since parametric analysis is not enabled inside the graphical interface of Abaqus. Afterwards the script was executed automatically inside the optimization program coded in C. The latter program automatically extracted the required results from the text files with analysis outputs created by Abaqus. Results and discussion of the procedure is contained in Chapter 1.

The beams tested in Chapter 2 were first modelled in Abaqus also using the Beam elements. Varying the tensile load and performing a regular modal analysis, we managed to obtain sufficient correlation with experimental results (see Section 4.3 for details on the results). The accuracy of identification with respect to experiment was 1-5%. The Beam element option provided fast calculation, no convergence problems and optimal results, the only disadvantage was that there was no possibility to model a crack

damage. For this purpose we referred to modelling with Solid elements: 24k of C3D8R 8-node linear brick elements (see Figure 4.2).



**Figure 4.2. Tie-rod represented with Solid elements in Abaqus CAE.**

Modelling a tie-rod or any beam-like structure with a reasonable amount of Solid elements means enlarging the model dimension, i.e. increasing the number of *dofs*, and thus, it is likely to make the system less stiff with respect to the Beam model. This causes lower eigenfrequencies, if the rest of parameters are kept the same, which has been observed from the results reported in Table 4-1 of the following Section.

Abaqus allows to model fractures in two-dimensional (Shell elements) and three-dimensional (Solid elements) models as *stationary* or *propagating* cracks. Cracks are

---

defined in the Interaction module. To perform a *contour integral* analysis in case of a stationary crack, one must define the crack front, the crack tip or crack line, and the crack extension direction. Alternatively, a crack can be modelled as a line embedded in a face in a two-dimensional model or as a face embedded in a cell in a three-dimensional model. The embedded line or face is called a *seam*. When the model is meshed, Abaqus creates duplicate overlapping nodes on the seam; these coincident nodes are free to move apart as the seam separates. However, a contour integral estimate does not predict how a crack will propagate and is applicable only for static or quasi-static problems.

A more advanced way to model a propagating defect, that has been introduced recently, involves the *extended finite element method* (XFEM). XFEM is an extension of the conventional finite element method based on the concept of partition of unity. It allows the presence of discontinuities in an element by enriching degrees of freedom with special displacement functions. XFEM enables prediction of the *crack initiation*, *propagation* and *failure* by means of two distinct types of damage modelling: cohesive segments approach or linear elastic fracture mechanics (LEFM) approach. The cohesive segments approach uses traction-separation laws and follows the general framework for surface-based cohesive behaviour; the damage properties are specified as part of the bulk material definition. The LEFM-based approach employs the virtual crack closure technique (VCCT), and the damage properties in this case are specified via an interaction property assigned to the XFEM crack. The crack can be modelled independently from the mesh.

Both of the mentioned techniques are not supported for eigenfrequency extraction, although they are available for static or quasi-static, implicit dynamic, and low-cycle fatigue procedures.

A chosen workaround towards the modal analysis was modelling an open crack as a circular V-notch of a small 0.2 mm opening and with zero curvature radius at the tip. This does not identically represent the defect in the beam that was subjected to testing reported in Chapter 2, but allows to assess the sensitivity of natural modes to a damage.

Figure 4.3 shows the ring-shaped defect embedded in the transverse section of the beam. Results of FEM analyses of the healthy and the damaged beams are reported in the following Section.

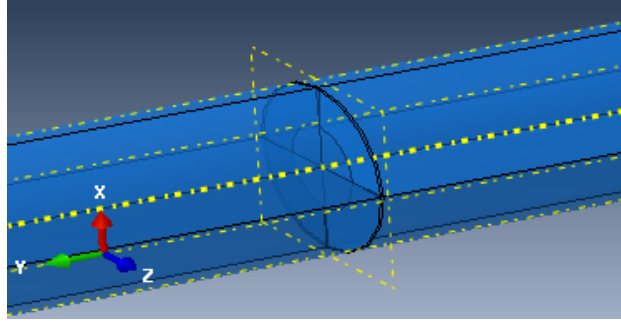


Figure 4.3. Damaged tie-rod in Abaqus CAE.

## 4.3 Modal Analysis

First, validation of a tie-rod model has been performed throughout confronting the results of the FEM modal analysis with the experimental modal analysis and theoretical eigenfrequencies of an unloaded beam. Figure 4.4 shows that analytical solution and FEM gave almost identical results with maximum deviation of 0.02 Hz in the fourth natural frequency,

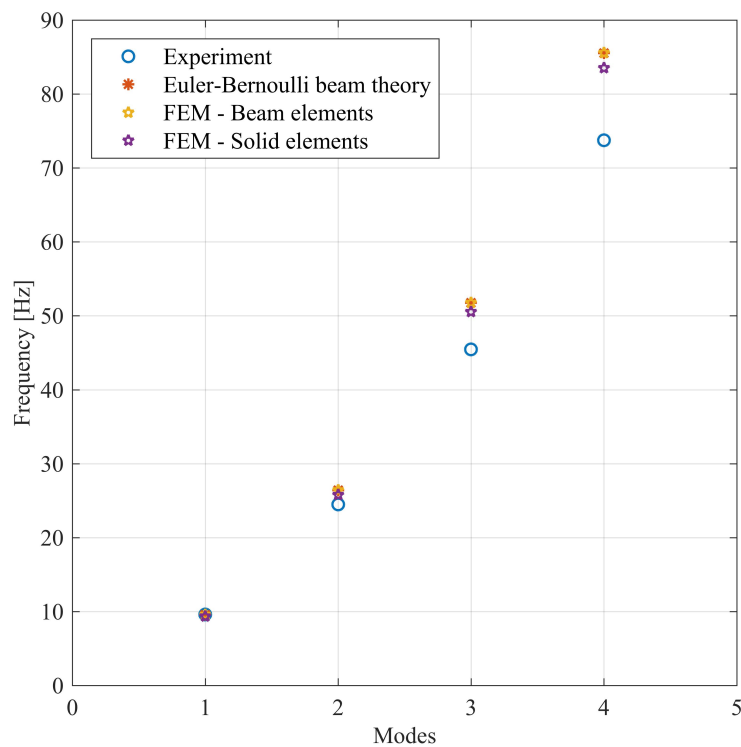


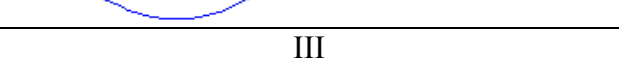

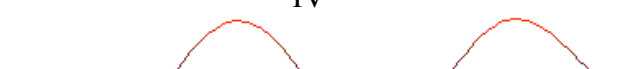


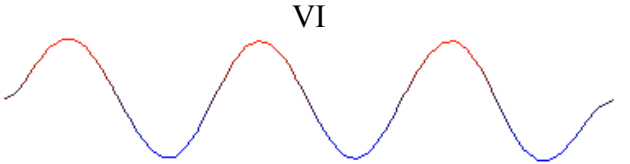
Figure 4.4. Model validation: natural frequencies of an unloaded beam.



Acquisition of vibrations with a single accelerometer does not provide enough data to reconstruct the modal shapes. To be able to do that, acquisitions from different point of the structure is needed, which gives information about phase of the motion of one point with respect to another, subsequently, the vibration mode shapes can be recognized. In this study this was not required, since beam modal shapes are well known and the FEM software was used to visualize them. Natural frequencies of a beam loaded in tension are higher compared to an unloaded one, but the natural modes do not change, and the beam can be seen simply as more rigid. Table 4-1 illustrates the first six modal shapes computed from FEM and comparison of the corresponding natural frequencies: experimental and numerical from analyses of the Beam and Solid models.

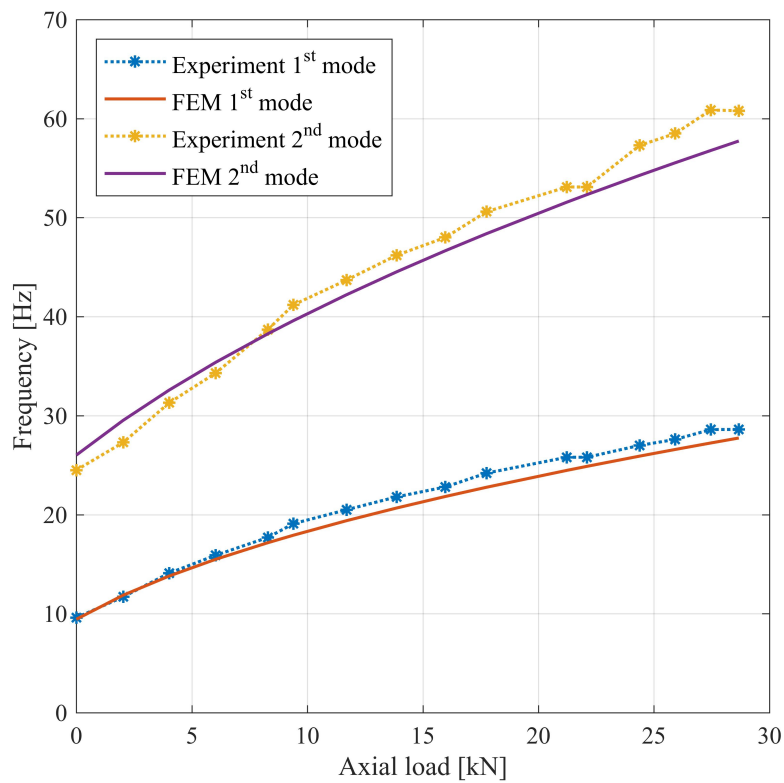
**Table 4-1. Modal shapes of the healthy beam under tensile load of 11.7 kN.**

Modal shapes	Frequency [Hz]		
	Experiment	Beam model	Solid model
I 	20.50	19.40	19.30
II 	43.70	42.22	41.98
III 	70.20	70.77	69.98
IV 	102.20	106.24	104.79
V 	140.10	149.26	146.89

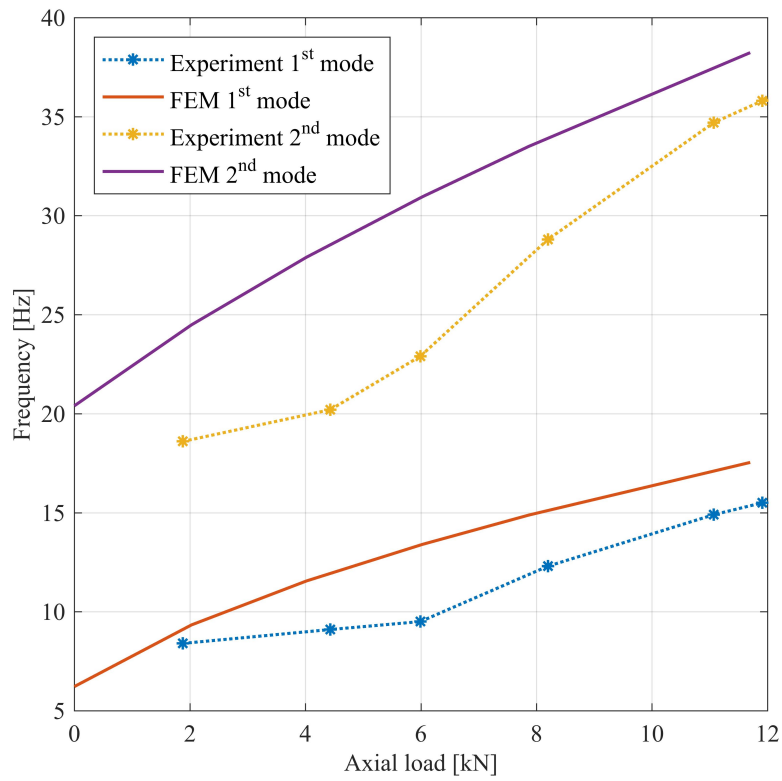
	184.20	200.13	196.61
Residual error $W_1 = \{1,1,1,1,1,1\}$	-	18.91	4.56
Residual error $W_3 = \{4,1,0.5,0.25,0.1,0.05\}$	-	5.69	3.79
Residual error $W_2 = \{10,1,1,1,1,1\}$	-	19.20	4.57

The Solid-element model matched the experimental results better than the Beam-element model. The match was controlled computing the residual error with different sets of weight coefficients according to Equation (18) as it has been done in Chapter 1.

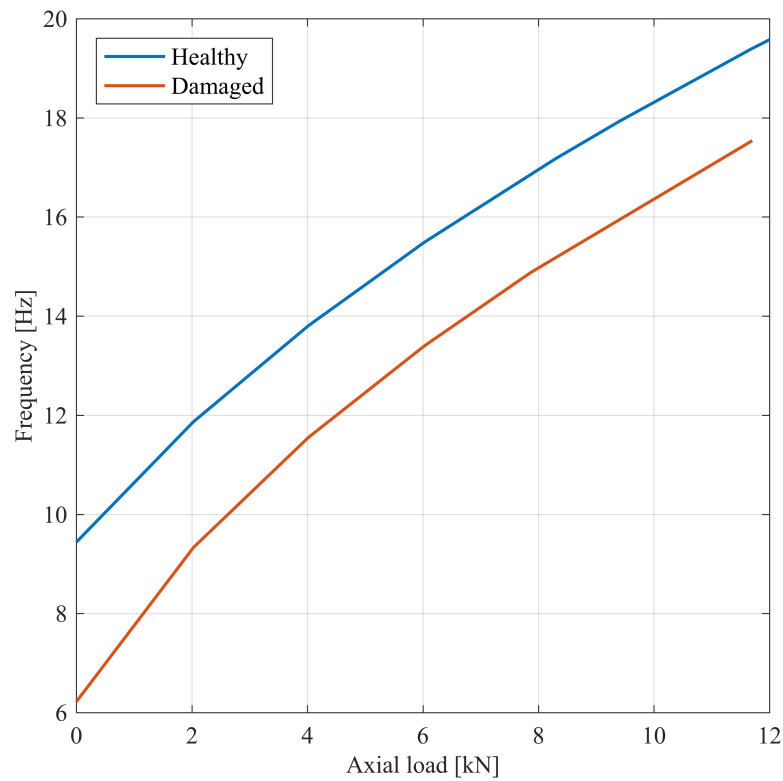
The following Figures 4.5 - 4.7 show two first natural frequencies of the beams with and without damage determined experimentally and via FEM analysis plotted with respect to tensile load.



**Figure 4.5. Natural frequencies of the healthy beam: experiment vs. FEM.**



**Figure 4.6. Natural frequencies of the damaged beam: experiment vs. FEM.**



**Figure 4.7. Fundamental frequency of the healthy and damaged beams in FEM.**

## 4.4 Conclusions

In the conducted research computer simulations with finite element method served some important purposes. Based on a parametric Beam model in Chapter 1 we managed to determine the loading conditions of the ancient tie-rods of Casa Romei in Ferrara. The given input data was composed of sets of natural frequencies, weight coefficients and parameter ranges.

Further, the tested healthy and damaged tie-rods treated in Chapter 2 were modelled with Beam and Solid elements in Abaqus CAE. Only a two- and three- dimensional models can incorporate cracks or notches in Abaqus software. The numerical simulation provided optimal correspondence to the experimental modal analysis of the healthy beam (see Figure 4.5). The FEM model with a crack demonstrated decrease of the natural frequencies compared to the non-damaged model (see Figure 4.7). However, the difference captured by the experiment was more significant, as deduced from Figure 4.6. Still, the qualitative trend of the damaged beam behaviour predicted by FEM has been confirmed by the experiment.

Besides that, FEM analysis was used to visualize forms of vibrations. Validation of FEM models has been carried out on simple examples with available analytical solutions and comparing with experimental results.

FEM modelling and simulations remain subject to constant improvement.

---

# Conclusion

The present thesis focused on development of *in situ* experimental method for health-monitoring of tie-rods. The content was organized in four Chapters. Chapter 1 “Axial load identification in tie-rods” introduced a nondestructive technique for tensile load identification in structural tie-rods and reported results of the method application to a case study of Casa Romei in Ferrara, Italy. The method consisted of two stages: experimental and numerical. In the first part vibrations of the tie-rods caused by an instrumented hammer impact were recorded via accelerometers, and the geometries of tie-rods were measured. The experimental data was elaborated in terms of modal analysis and the first six natural frequencies for each tested tie-rod were extracted. The second part of the method employed a program coded in C, which determined the axial load based on the input data: natural frequencies and configuration of a tie-rod. Tie-rods were represented with Beam elements in a parametric FEM model and the extremities inserted in the masonry walls were modelled as supported by an elastic Winkler-type foundation. The deviation of numerically determined frequencies from the experimental ones was evaluated by a residual error function, where weight coefficients were assigned to the natural modes according to their importance. This error function was the optimization criteria. Thus, the optimization parameters were the tensile load and the distributed stiffness of the elastic boundaries. The program required imposing the ranges of these parameters and after execution the code was automatically running the FEM analysis in Abaqus for each combination of the parameters, extracting the results, and finally finding the minimum of the error function. The optimal value of parameters were then reported as the solution to the stated problem, the main objective of which was to identify the axial load in tie-rods and to draw assumptions about their reliability and functionality based on the obtained results.

---

The novelty of this method with respect to other available techniques is the computer-aided multi-parameter optimization algorithm and consideration of uncertain boundary conditions in the tie-rod model. Parameterisation of the boundary conditions allowed to reach a very precise match with experiment and showed a significantly higher tensile load than for a model with ordinary boundaries. Approbation of the technique on an *in situ* case study proved that it is of a simple execution and still very efficient for the axial load estimation in ancient tie-rods.

Chapter 2 “Damage identification in tie-rods” focused on the development of method of damage detection in metal beams based on vibration analysis. The procedure of vibration acquisition and modal analysis were similar to the experiment employed in the case-study of Chapter 1. With the objective to spot differences between vibrational response of a new beam with no damage and an identical beam with a defect, a particular experimental setup was invented. It allowed dynamic and static testing of the beams under manually adjustable axial tensile load of up to 30 kN in order to model the real tie-rod working conditions. The structural defect inside a beam was represented throughout joining of two parts with a bolt connection, which could be tightened with a prescribed torque.

The acquisition of vibrations was performed for the damaged and healthy beams under variable axial load and for different torques applied at the joint. The test results were elaborated in terms of modal analysis: frequency response functions, natural frequencies, and modal damping ratios. The laboratory tests showed that the artificial defect noticeably decreased the natural frequencies of the beam and increased the modal damping ratios of the response. Based on analysis of the FRFs and modal parameters we managed to spot the damage identifiers that can be applied to health-monitoring of tie rods *in situ*. The main signs were lower natural frequencies and higher damping ratios of the damaged beam with respect to the healthy one; presence of broken or doubled peaks or other nonlinearities in the FRF, and overall smaller amplitudes of the FRF. Results of the experimental modal analysis were compared to frequencies obtained from FEM computation. Details on the modelling were addressed in Chapter 4 “FEM simulations”.

The static compliance tests, both tensile and flexural, confirmed the system stiffness reduction for the damaged beam compared to the healthy one. In Chapter 3 “Fracture

mechanics approach” the compliance caused by the presence of a defect was estimated using the LEFM methods. The damage configuration adopted in this experimental study is most closely represented by a ring-shaped crack. Other standard crack shapes typical for round bars were reviewed as well in terms of stress intensity factors. In order to determine the equivalent crack configurations and crack opening loads for the artificial damage it is necessary to measure compliance using specific high-precision crack mouth or similar gauges.

Material aging, corrosion due to environmental conditions, displacements in the masonry and foundation due to seismic loads or crawling with time – these are the factors to blame for cracks occurring in tie-rods. The regular health-monitoring of tie-rods helps to preserve the precious architectural heritage of the humanity and to keep the beautiful buildings in a good condition as long as possible. We hope that the easily executed testing methods reported herein will assist in advancing the existing NDT techniques. Having at hand a tool of crack detection via vibrometric acquisitions, the next step to the full picture is to provide a way to estimate the crack depth and configuration, and thus, enable the assessment of the severity of the defect.

Throughout this research we tried to make a step towards understanding the correlation between a fracture and the vibrational behaviour of a structure, which still remains a scientific challenge for engineers. We observed that even a localized defect was able to change on the macroscale the main characteristics of the system, like stiffness and damping, that were captured via the modal analysis. The “music” of the dynamic response is definitely capable to tell us more than we by now comprehended.

The future path for this research is to test some cracked ancient tie-rods in our laboratory in order to improve the methodology. Furthermore, it is necessary appropriate the developed concept *in situ* on functioning tie-rods, and to confront the results with other available NDT technique. Collecting modal data from many tie-rods, we can create a database of “healthy” and “damaged” FRFs. This would provide a possibility to develop a software based on Neural Networks. The program that first would learn from numerous examples, then would become capable of recognizing the patterns of good/broken elements behaviour and of classifying the data. A numerical tool like this would make a valuable impact on performing non-destructive vibration analysis.

---

# Bibliography

- [1] M. Amabili, S. Carra, L. Collini, R. Garziera, A. Panno, Estimation of tensile force in tie-rods using a frequency-based identification method, *Journal of Sound and Vibration* 329 (11) (2010) 2057–2067.
- [2] R. Garziera, M. Amabili, L. Collini. A hybrid method for the nondestructive evaluation of the axial load in structural tie-rods. *Nondestructive Testing and Evaluation* 26 (2) (2011) 197–208.
- [3] L. Collini, R. Fagiani, R. Garziera, K. Riabova, M. Vanali. Load and effectiveness of the tie-rods of an ancient Dome: Technical and historical aspects. *Journal of Cultural Heritage* 16 (2015) 597–601.
- [4] L. Collini, R. Garziera. Measurement of the tensile force in the hoop tie-rods of an historical dome. *Proceedings of PROHITECH'14 - 2nd Int. Conf. on Protection of Historical Constructions*. 7-9 May 2014, Antalya, Turkey.
- [5] L. Collini, R. Garziera. K. Riabova. Numerical Method for the Estimation of Tensile Load in Tie-rods. *Proceedings of 14th Youth Symposium on Experimental Solid Mechanics*, May 20-23, 2015 Traunkirchen Monastery, Austria.
- [6] L. Collini, R. Garziera. K. Riabova Experimental and numerical determination of the axial load in structural tie-rods with complex boundary conditions. *Proceedings of CILAMCE - XXXVI Ibero-Latin American Congress on Computational Methods in Engineering*, 22-25 November 2015, Rio de Janeiro, Brasil.
- [7] M. Amabili, R. Garziera, A technique for the systematic choice of admissible functions in the Rayleigh–Ritz method, *Journal of Sound and Vibration* 224 (1999) 519–539



- 
- [8] P. Pozzati, *Teoria e Tecnica delle Strutture (Theory and Technique of Structures)*, UTET, Torino, 1977.
- [9] M.L. Beconcini, Un metodo pratico per la determinazione del tiro nelle catene (a practical method for the determination of tensile load in tie-rods), *Costruire in Laterizio* 54/96 (1996) 299–301.
- [10] S. Briccoli Bati, U. Tonietti, Experimental method for estimating in situ tensile force in tie-rods, *Journal of Engineering Mechanics* 127 (2001) 1275–1283.
- [11] C. Blasi, S. Sorace, Sulla determinazione del “tiro” nelle catene mediante prove statiche e dinamiche. Atti III Congresso Nazionale ASS.I.R.CO, Catania, Italy, November 1988.
- [12] C. Blasi, S. Sorace, Determining the axial force in metallic rods, *Structural Engineering International (IABSE)* 4 (1994) 241–246.
- [13] S. Sorace, Parameter models for estimating in-situ tensile force in tie-rods, *Journal of Engineering Mechanics* 122 (1996) 818–825.
- [14] S. Lagomarsino, C. Calderini, The dynamical identification of the tensile force in ancient tie-rods, *Engineering Structures* 27 (2005) 846–856.
- [15] K. Maes, J. Peeters, E. Reynders, G. Lombaert, G. De Roeck. Identification of axial forces in beam members by local vibration measurements. *Journal of Sound and Vibration*, Volume 332 (2013) 5417–5432.
- [16] S. Li, E. Reynders, K. Maes, G. De Roeck. Vibration-based estimation of axial force for a beam member with uncertain boundary conditions. *Journal of Sound and Vibration*, 332 (2013) 795–806.
- [17] G. Rebecchi, N. Tullini, F. Laudiero. Estimate of the axial force in slender beams with unknown boundary conditions using one flexural mode shape. *Journal of Sound and Vibration* 332 (2013) 4122–4135.
- [18] N. Tullini. Bending tests to estimate the axial force in slender beams with unknown boundary conditions. *Mechanics Research Communications* 53 (2013) 15–23.
- [19] N. Tullini, G. Rebecchi, F. Laudiero. Bending tests to estimate the axial force in tie-rods. *Mechanics Research Communications* 44 (2012) 57–64.

- 
- [20] N. Tullini, F. Laudiero. Dynamic identification of beam axial loads using one flexural mode shape. *Journal of Sound and Vibration* 318 (2008) 131–147.
- [21] C. Gentilini, A. Marzani, M. Mazzotti. Nondestructive characterization of tie-rods by means of dynamic testing, added masses and genetic algorithms. *Journal of Sound and Vibration* 332 (2013) 76–101.
- [22] T. Livingston, J.G. Beliveau, D.R. Huston. Estimation of axial load in prismatic members using flexural vibrations. *Journal of Sound and Vibration* 179 (1995) 899–908.
- [23] B.H. Kim, T. Park, Estimation of cable tension force using the frequency-based system identification method, *Journal of Sound and Vibration* 304 (2007) 660–676.
- [24] C. Urbano, Sulla determinazione del tiro nelle catene degli archi: considerazioni teoriche ed applicazioni sperimentali (on the determination of tensile load in tie-rods of arcs: theoretical considerations and experimental applications), *Costruzioni Metalliche* 5 (1967) 315–323
- [25] M. Arduini, R. Carli, P. Cesari, Tecniche di identificazione dello sforzo e del grado di vincolo nei tiranti strutturali con metodi dinamici (identification techniques of stress and the degree of constraint in the structural tie-rods with dynamic methods), *Ingegneri Architetti Costruttori (INARCOS)* 563 (1995) 493–496
- [26] E. Viola, M. Dilena, E. Artioli, Identification of metallic rods by frequency estimation on the historical church tower in S. Vito al Tagliamento (PN) - Italy, *Proceedings of the International Conference on Restoration, Recycling and Rejuvenation Technology for Engineering and Architecture Application*, Cesena, Italy, 2004
- [27] W.-X. Ren, G. Chen, W.-H. Hu, Empirical formulas to estimate cable tension by cable fundamental frequency, *Structural Engineering and Mechanics* 20 (2005) 363–380.
- [28] S. Park, S. Choi, S.-T. Oh, N. Stubbs, H.-C. Song, Identification of the tensile force in high-tension bars using modal sensitivities, *International Journal of Solids and Structures* 43 (10) (2006) 3185–3196

- 
- [29] S.H. Farghaly, K.M. Zeid. An exact frequency equation for an axially loaded beam-mass-spring system resting on a Winkler elastic foundation. *Journal of Sound and Vibration* (1995) 185(2), 357–363.
- [30] P. Ruge, C. Birk. A comparison of infinite Timoshenko and Euler–Bernoulli beam models on Winkler foundation in the frequency- and time-domain. *Journal of Sound and Vibration* 304 (3–5) (2007) 932–947.
- [31] S.G. Koroma, M.F.M. Hussein, J.S. Owen. Vibration of a beam on continuous elastic foundation with nonhomogeneous stiffness and damping under a harmonically excited mass. *Journal of Sound and Vibration* 333 (9) (2014) 2571–2587.
- [32] Silva, J. M. M., & Gomes, A. J. M. A. (1990). Experimental dynamic analysis of cracked free-free beams. *Experimental Mechanics*, 30, 20-25.
- [33] Doebling, S. W., Farrar, C. R., Prime, M. B., & Shevitz, D. W. (1998). A summary review of vibration based damage identification methods. *The Shock and Vibration Digest*, 30, 91-105.
- [34] A. S. Bouboulas, S. K. Georgantzinou and N. K. Anifantis. *Advances in Vibration Engineering and Structural Dynamics*. Chapter 8: Vibration Analysis of Cracked Beams Using the Finite Element Method. Edited by Francisco Beltran-Carbajal. InTech, 2012.
- [35] T.G. Chondros, A.D. Dimarogonas, Identification of cracks in welded joints of complex structures, *Journal of Sound and Vibration* 69 (1980) 531–538.
- [36] T.G. Chondros, A.D. Dimarogonas, Dynamic sensitivity of structures to cracks, *Journal of Vibration, Acoustics, Stress, and Reliability in Design* 111 (1989) 251–256.
- [37] T.G. Chondros, Fatigue fracture of the Bjork–Shiley heart valve strut and failure diagnosis from acoustic signatures, *Theory of Applied Fracture Mechanics* 54 (2010) 71–81.
- [38] A.D. Dimarogonas, S.A. Paipetis, *Analytical Methods in Rotor Dynamics*, Elsevier Applied Science Publishers, London, 1983.
- [39] A.D. Dimarogonas, *Vibration for Engineers*, 2nd ed., Prentice-Hall, Upper Saddle River, 1996.

- 
- [40] T.G. Chondros, The continuous crack flexibility method for crack identification, *Fatigue & Fracture of Engineering Materials & Structures* 24 (2001) 643–650.
- [41] A.D. Dimarogonas. Vibration of cracked structures: a state of the art review. *Engineering Fracture Mechanics* 55 (1996). 831–857.
- [42] Christides, S., & Barr, A. D. S. (1984). One-dimensional theory of cracked Bernoulli- Euler beams. *International Journal of Mechanical Sciences*, 26, 639-648.
- [43] Dimarogonas, A. D. *Vibration Engineering*. West Publishers (1976), St Paul, Minnesota, USA.
- [44] Chondros, T. G., & Dimarogonas, A. D. (1980). Identification of cracks in welded joints of complex structures. *Journal of Sound and Vibration*, 69, 531-538.
- [45] Krawczuk, M., Żak, A., & Ostachowicz, W. (2000). Elastic beam finite element with a transverse elasto-plastic crack. *Finite Elements in Analysis and Design*, 34, 61-73.
- [46] Bouboulas, A. S., & Anifantis, N. K. Formulation of cracked beam element for analysis of fractured skeletal structures. *Engineering Structures* 30 (2008) 894-901.
- [47] P.F. Rizos, N. Aspragathos, A.D. Dimarogonas, Identification of crack location and magnitude in a cantilever beam from the vibration modes, *Journal of Sound and Vibration* 138 (1990) 381–388.
- [48] Y. Narkis, E. Elmalah, Crack identification in a cantilever beam under uncertain end conditions, *Int.J.Mech.Sci.* 38 (1996) 499–507.
- [49] T.G. Chondros, A.D. Dimarogonas Vibration of a cracked cantilever beam, *Trans. ASME* 120 (1998) 742–746.
- [50] M.A. Mahmoud, M.A. Zaid, S. Al Harashani, Numerical frequency analysis of uniform beams with a transverse crack, *Commun.Numer.Methods Eng.* 15 (1999) 709–715.
- [51] F.G. Tomasel, H.A. Larrondo, P.A.A. Laura, Detection of cracks in cantilever beams: experimental set-up using optical techniques and theoretical modelling, *Journal of Sound and Vibration* 228 (1999) 1195–1204.

- 
- [52] J.K. Sinha, M.I. Friswell, S. Edwards, Simplified models for the location of cracks in beam structures using measured vibration data, *Journal of Sound and Vibration* 251 (2002) 13–38.
- [53] J.K. Sinha, M.I. Friswell. Simulation of the dynamic response of a cracked beam. *Computers and Structures* 80 (2002) 1473–1476
- [54] F.B. Sayyad, B. Kumar, B.P. Ronge, Theoretical and experimental study for identification of crack in vibrating simply supported beam, *Proceedings of the Tenth International Congress on Sound and Vibration, Stockholm, Sweden, 2003*, pp. 3027–3035.
- [55] E. Douka, G. Bamnios, A. Trochidis, A method for determining the location and depth of cracks in double-cracked beams, *Applied Acoustics* 65 (2004) 997–1008.
- [56] M.B. Kim, M. Zhao, Study on crack detection of beam using harmonic responses, *Proceedings of the 2004 IEEE International Conference on Intelligent Mechatronics and Automation, Chengdu, China (2004)* 72–76.
- [57] X.F. Chen, Z.J. He, J.W. Xiang, Experiments on crack identification in cantilever beams, *Exp.Mech.* 45 (2005) 295–300.
- [58] A.M. Yan, G. Kerschen, P. De Boe, J.C. Golinval, Structural damage diagnosis under changing environmental conditions, Part I: a linear analysis, *Mech. Syst. Signal Process.* 19 (2005) 865–880.
- [59] Gudmundson, P. (1983). The dynamic behavior of slender structures with cross-sectional cracks. *Journal of the Mechanics and Physics of Solids*, 31, 329-345.
- [60] Cacciola, P., & Muscolino, G. (2002). Dynamic response of a rectangular beam with a known non-propagating crack of certain or uncertain depth. *Computers and Structures*, 80, 2387-2396.
- [61] Benfratello, S., Cacciola, P., Impollonia, N., Masnata, A., & Muscolino, G. (2007). Numerical and experimental verification of a technique for locating a fatigue crack on beams vibrating under Gaussian excitation. *Engineering Fracture Mechanics*, 74, 2992-3001.
- [62] Sholeh, K., Vafai, A., & Kaveh, A. (2007). Online detection of the breathing crack using an adaptive tracking technique. *Acta Mechanica*, 188, 139-154.

- 
- [63] Clark, R., Dover, W. D., & Bond, L. J. (1987). The effect of crack closure on the reliability of NDT predictions of crack size. *NDT International*, 20, 269-275.
- [64] Abraham, O. N. L., & Brandon, J. A. (1995). The modelling of the opening and closure of a crack. *Journal of Vibration and Acoustics*, 117, 370-377.
- [65] Douka, E., & Hadjileontiadis, L. J. (2005). Time-frequency analysis of the free vibration response of a beam with a breathing crack. *NDT&E International*, 38, 3-10.
- [66] Loutridis, S., Douka, E., & Hadjileontiadis, L. J. (2005). Forced vibration behavior and crack detection of cracked beams using instantaneous frequency. *NDT&E International*, 38, 411-419.
- [67] P.N. Saavedra, L.A. Cuitiño. Crack detection and vibration behaviour of cracked beams. *Computers and Structures* 79 (2001). 1451-1459.
- [68] Andrieux, S., & Varé, C. (2002). A 3D cracked beam model with unilateral contact. Application to rotors. *European Journal of Mechanics A/Solids*, 21, 793-810.
- [69] Nandi, A., & Neogy, S. (2002). Modelling of a beam with a breathing edge crack and some observations for crack detection. *Journal of Vibration and Control*, 8, 673-693.
- [70] Andreaus, U., Casini, P., & Vestroni, F. Nonlinear dynamics of a cracked cantilever beam under harmonic excitation. *International Journal of Nonlinear Mechanics* 42 (2007) 566-575.
- [71] O. Giannini, P. Casini, F. Vestroni. Nonlinear harmonic identification of breathing cracks in beams. *Computers and Structures* 129 (2013) 166–177.
- [72] Bovsunovsky A.P., Bovsunovsky O. Crack detection in beams by means of the driving force parameters variation at nonlinear resonance vibrations. *Key Eng Mater* 2007;347:413–20.
- [73] Chatterjee A. Structural damage assessment in a cantilever beam with a breathing crack using higher order frequency response functions. *J Sound Vibr* 2009; 329: 3325–34.

- 
- [74] Andraus U, Baragatti P. Cracked beam identification by numerically analysing the nonlinear behaviour of the harmonically forced response. *Journal of Sound and Vibration* 2011;330:721–42.
- [75] U. Andraus, P. Baragatti. Experimental damage detection of cracked beams by using nonlinear characteristics of forced response. *Mechanical Systems and Signal Processing* 31 (2012) 382–404.
- [76] U. Andraus, P. Baragatti, Fatigue crack growth, free vibrations and breathing crack detection of aluminium alloy and steel beams, *J.Strain Anal. Eng. Des.* 44 (2009) 595–608.
- [77] D. Chelidze, M. Liu, Dynamical systems approach to fatigue damage identification, *J.SoundVibr.* 281 (2005) 887–904.
- [78] J.N. Sundermeyer, R.L. Weaver, On crack identification and characterization in a beam by nonlinear vibration analysis, *Journal of Sound and Vibration* 183 (1995) 857–871.
- [79] M. Kisa, J.Brandon, M. Topcu, Free vibration analysis of cracked beams by a combination of finite elements and component mode synthesis methods, *Comput. Struct.* 67 (1998) 215–223.
- [80] A. Rivola, P.R. White, Bispectral analysis of the bilinear oscillator with application to the detection of fatigue cracks, *Journal of Sound and Vibration* 216 (1998) 889–910.
- [81] S.L. Tsyfansky, V.I. Beresnevich, Non-linear vibration method for detection of fatigue cracks in aircraftwings, *Journal of Sound and Vibration* 236 (2000) 49–60.
- [82] F. Leonard, J. Lanteigne, S. Lalonde, Y. Turcotte, Free-vibration behaviour of a cracked cantilever beam and crack detection, *Mech.Syst.Signal Process.* 15 (2001) 529–548.
- [83] A.P. Bovsunovsky, C. Surace, R. Ruotolo, The effect of damping on the non-linear dynamic behaviour of a cracked beam at resonance and super-resonance vibrations, *KeyEng.Mater.* 245 (2003) 97–106.
- [84] A.P. Bovsunovsky, C.Surace, Considerations regarding superharmonic vibrations of a cracked beam and the variation in damping caused by the presence of the crack, *Journal of Sound and Vibration* 288 (2005) 865–886.

- 
- [85] V.K. Nguyen, O.A. Olatunbosun, A proposed method for fatigue crack detection and monitoring using the breathing crack phenomenon and wavelet analysis, *J.Mech.Mater.Struct.* 2 (2007) 399–420.
- [86] Z.K. Peng, Z.Q. Lang, S.A. Billings, Crack detection using nonlinear output frequency response functions, *Journal of Sound and Vibration* 301 (2007) 777–788.
- [87] Z.K. Peng, Z.Q. Lang, F.L. Chu. Numerical analysis of cracked beams using nonlinear output frequency response functions. *Computers and Structures* 86 (2008) 1809–1818.
- [88] V.V. Matveev, A.P. Bovsunovsky, Vibration-based diagnostics of fatigue damage of beam-like structures, *J.SoundVibr.* 249 (2002) 23–40.
- [89] A.M. Yan, G. Kerschen, P. De Boe, J.C. Golinval, Structural damage diagnosis under changing environmental conditions, Part II: local PCA for nonlinear cases, *Mech. Syst. Signal Process.* 19 (2005) 847–864.
- [90] Shuncong Zhong, S. Olutunde Oyadiji. Crack detection in simply supported beams without baseline modal parameters by stationary wavelet transform. *Mechanical Systems and Signal Processing* 21 (2007) 1853–1884.
- [91] Shuncong Zhong, S. Olutunde Oyadiji. Detection of cracks in simply-supported beams by continuous wavelet transform of reconstructed modal data. *Computers and Structures* 89 (2011) 127–148.
- [92] Bachschmid, N., Tanzi, E., & Audebert, S. (2008). The effect of helicoidal cracks on the behavior of rotating shafts. *Engineering Fracture Mechanics*, 75, 475-488.
- [93] T.G. Chondros, A.D. Dimarogonas, J. Yao. Vibration of a beam with a breathing crack. *Journal of Sound and Vibration* 239 (2001). 57–67.
- [94] Singiresu S. Rao. *Mechanical Vibrations*. 5th edition (2011) Pearson Education, Inc., Upper Saddle River, NJ, USA. 1104 pages. ISBN-13: 978-0132128193 ISBN-10: 0132128195.
- [95] M. Bellanova, M. Carboni, R. Felicetti, A. Gianneo. Individuazione di difetti sulle catene sottriche metalliche. *Giornale delle Prove non distruttive, monitoraggio, diagnostica. AIPnD* 4 (2015) 4 49–54.



- 
- [96] Jaap Schijve. *Fatigue of Structures and Materials*. Springer Science+Business Media, B.V., 2009. ISBN-13: 978-1-4020-6807-2 e-ISBN-13: 978-1-4020-6808-9.
- [97] Peterson, R.E., *Stress Concentration Factors*. John Wiley & Sons, New York (1974). New edition by Pilkey, W.D. and Pilkey, D.F., *Peterson's Stress Concentration Factors*, 3<sup>rd</sup> rev. edn., John Wiley & Sons (2008).
- [98] Shigley, Joseph Edward, *Budynas–Nisbett Shigley's Mechanical Engineering Design*. McGraw–Hill, 8<sup>th</sup> edition (2006).
- [99] Irwin, G.R., Analysis of stresses and strains near the end of a crack traversing a plate. *Trans. ASME, J. Appl. Mech.*, Vol. 24 (1957), pp. 361–364.
- [100] Irwin, G.R., The crack extension force for a part-through crack in a plate. *Trans. ASME, J. Appl. Mech.*, Vol. 29 (1962), pp. 651–654.
- [101] Murakami, Y. (Ed.) *Stress Intensity Factors Handbook*. Pergamon Press, Oxford (1987).
- [102] Tada, H., Paris, P.C. and Irwin, G.R., *The Stress Analysis Handbook*, 2nd edition. Paris Productions Inc., St. Louis (1985).
- [103] Rooke, D.P. and Cartwright, D.J., *Stress Intensity Factors*. Her Majesty's Stationary Office, London (1976).
- [104] Fleck N.A. Chapter 4 "Compliance Methods for Measurement of Crack Length" in *Fatigue Crack Measurement: Techniques and Applications*, eds. K. J. Marsh, R. A. Smith and R. Ritchie, EMAS Publications Ltd., Warley, England, 1991.
- [105] G. Urriolagoitia-Sosa, B. Romero-Ángeles, L.H. Hernández-Gómez, C. Torres-Torres, G. Urriolagoitia-Calderón. Crack-compliance method for assessing residual stress due to loading/unloading history: Numerical and experimental analysis. *Theoretical and Applied Fracture Mechanics* 56 (2011) 188–199.
- [106] J. Toribio, N. Álvarez, B. González, J.C. Matos. A critical review of stress intensity factor solutions for surface cracks in round bars subjected to tension loading. *Engineering Failure Analysis* 16 (2009) 794–809.
- [107] J. Toribio, J.C. Matos, B. González, J. Escudra. Compliance evolution in round cracked bars under tensile fatigue. *Engineering Fracture Mechanics* 78 (2011) 3243–3252.

- [108] J. Toribio, J.C. Matos, B. González, J. Escuadra. Evolution of crack paths and compliance in round bars under cyclic tension and bending. *Frattura ed Integrità Strutturale* 30 (2014) 182-190.
- [109] Lord Rayleigh, *Theory of Sound*, Dover, 1945.

---

## Vita

Kseniia Riabova was born in Kharkiv, Ukraine, on 31 July 1988, the daughter of Irina Byalaja and Sergey Riabov. In 2009 she accomplished a Bachelor's degree and in 2011 obtained a Master of Science degree in Mechanical Engineering, with distinction, at the Polytechnic University of her hometown. In 2011 she spent a few months as a research trainee at the RWTH Aachen University, Germany. In the next two years she started her career in Kharkiv out of the academia, and in 2013 she decided to resume her studies and enter a postgraduate program in Europe. From 2014 to the end of 2016 Kseniia was a PhD student at the University of Parma, Italy. In 2015 she did a graduate research internship at the McGill University, Montreal, Canada. She currently resides in Italy and can be reached on [ksenia.riabova@gmail.com](mailto:ksenia.riabova@gmail.com).